$Z + \gamma$ Cross-Section Measurement, $\sigma * BR(Z + \gamma)$, in the Electron Channel for $p\overline{p}$ Collisions at $\sqrt{s} = 1.8$ TeV, and Limits for the $ZZ\gamma$ and $Z\gamma\gamma$ Anomalous Couplings.

A dissertation

submitted by

Mary Roach-Bellino

In partial fulfillment of the requirements

for the degree of

Doctor of Philosophy

in

Physics

TUFTS UNIVERSITY

February, 1994

ABSTRACT OF THE DISSERTATION

$Z + \gamma$ Cross-Section Measurement, $\sigma * BR(Z + \gamma)$, in the Electron Channel for $p\bar{p}$ Collisions at $\sqrt{s} = 1.8$ TeV, and Limits for the $ZZ\gamma$ and $Z\gamma\gamma$ Anomalous Couplings.

by Mary Roach-Bellino, Ph.D.

Dissertation Director: Prof. K. Sliwa

The $Z + \gamma$ cross-section $\times$ branching ratio in the electron channel has been measured using the inclusive Z data sample from the CDF '88-'89 collider run, for which the total integrated luminosity was 4.05 ± 0.28 pb^{-1}.

Two Zγ candidates are observed from central photon events with $\Delta R_{l\gamma} > 0.7$ and $E_t^\gamma > 5.0$ GeV. From these events the $\sigma * BR(Z + \gamma)$ is measured and compared with SM predictions:

$$\sigma * BR(Z + \gamma)_e = 6.8^{+5.7}_{-5.7}(stat + syst)pb$$

$$\sigma * BR(Z + \gamma)_{SM} = 4.7^{+0.7}_{-0.2}(stat + syst)pb$$

From this Zγ cross section measurement limits on the $ZZ\gamma$ and $Z\gamma\gamma$ anomalous couplings for three different choices of compositeness scale Λ_Z are obtained. Our experimental sensitivity to the $h_{30}^{Z,\gamma}/h_{10}^{Z,\gamma}$ couplings is in the range of $\Lambda_Z \sim 450 - 500$ GeV and for the $h_{40}^{Z,\gamma}/h_{20}^{Z,\gamma}$ couplings $\Lambda_Z \sim 300$ GeV.

Acknowledgements

I'd like to begin by expressing my great appreciation of the Tufts University High Energy Physics Program, and in particular my advisor Prof. Krzysztof Sliwa for his unwavering encouragement and support.

Special thanks to Prof. W. Anthony Mann for initalizing my beginnings as a graduate student and for providing me my first work opportunity in Experimental High Energy Physics. This proved to be rewarding in many ways, not the least of which was learning a bit of electronics and humor from Prof. William Oliver. I'd like to thank Prof. Richard Milburn for his genuine concern, not only for me but for all students. To Prof. Austin Napier, thank you for endless discussions about computers. I know that my devotion to the "Amiga" may have caused you a few headaches. Further I thank you for your great smile, which never goes away. I also wish to thank Prof. Kathyrn McCarthy for all her guidance and her friendship. In addition, thanks to Dorothy DeStefano, Rita Fleischer and Waltye Greene for their companionship and seemingly endless secretarial support.

I'm grateful to all my fellow graduate students for their constant encouragement and understanding, but especially for their humor and friendship. To my "Solid-State" friend, Christine Considine-McCormack, I thank you for those long walks at lunchtime and for the great discussions that transpired. To my ex-officemate and good friend Dr. Stéphane Willocq, many many thanks for your patience in answering my neverending questions. You are a truly great teacher of physics and an excellent high energy physicist. I thank you further for introducing me to Alma Karas, without whom I would never have made it through those Fermilab years. Alma, thank you for being such a good friend and for trying to teach me the game of bridge(my

inabilities in this area have nothing to do with your teaching attempts). Further thanks to Carol Hawk, a Rutgers' graduate student and fellow CDF'er. Without Carol life in a large collaboration would have been devoid of any fun.

I'm indebted to Doug Benjamin for all his hard work which has been a major contribution to the results of this dissertation. In addition, I thank Prof. Steve Errede of the University of Illinois at Urbana-Champaign for his leadership and dedication to the analysis group.

I'd like to take this opportunity to thank a very dear friend and colleague, Dr. Marie A. Kenyon. Marie, thank you for your friendship and encouragement throughout our entire college years, but especially for those many evenings we "walked-the-Charles" and talked about everything. I shall cherish those times forever.

To my sisters Regina Madsen and Helen King, my brothers John and Charles Roach, and my "adopted" sister Carole Depin, thank you for enduring these years with me and for your unending love and support.

I am indebted to my parents, John and Elizabeth Roach for their encouragement, steadfastness and love. Without you this thesis would not have been possible-alas we can celebrate!

To my husband Michael, thank you for your love and encouragement. I'm very greatful for your undying devotion to my goal and for your humor, which has seen us through many tough times. Last but not least, I'd like to thank my son, Christopher Michael for being a wonderful light of hope and love in my life. He is truly my greatest achievement.

Dedication

to my loving parents,

John and Elizabeth Roach

and

in memory of my grandmother

Mary Moore

Table of Contents

List of Tables

List of Figures

Chapter 1
Introduction

The unification of the electromagnetic and weak interactions, as described by the gauge group $SU(2)_L \otimes U(1)_Y$, is referred to as the Electroweak Theory or more generally as The Standard Model. The vector bosons $W^{\pm}$ are carriers of the charged weak currents while the γ and Z° are mediators of the neutral currents. The couplings between these bosons and the quarks and leptons can be tested by measuring the production cross-sections or rates of W and Z particles. By determining the production cross-sections for the similar processes, $W\gamma$ and $Z\gamma$, not only can their anomalous couplings be tested, but information on higher order static and transition moments respectively can be gained. Furthermore by pushing beyond the realm of the Standard Model, higher production cross-sections for these processes could be indicators of internal structure or compositeness of W and Z bosons.

The 1988-1989 data collected by the CDF collaboration as listed in Appendix A is used for this analysis. The purpose of this work is to measure the production cross-section of $Z\gamma$ events. In addition, the limits for the anomalous $ZZ\gamma$ and $Z\gamma\gamma$ couplings are investigated as well as the possibilities for Z boson compositeness.

The organization of the dissertation is as follows:

- In Chapter 2, an overview of the Electroweak Theory is presented with the introduction of the basic concepts which describe the weak vector bosons. Briefly the anomolous couplings of the Z boson for both tree-level and beyond as well as a possible composite model are discussed.

- In Chapter 3, the apparatus used to obtain the physics results is described.

This chapter begins with an overview of the fundamental properties of the Tevatron accelerator, and then highlights those components of the CDF detector which are pertinent, e.g. the CEM,PEM,FEM calorimeters as well as the tracking chambers and trigger specifics.

- In Chapter 4, the analysis methods are discussed. The process of event reconstruction and selection begins the chapter, which includes the electron identification process, followed by the Monte Carlo simulations used in this analysis.

- In Chapter 5, the acceptances, efficiencies and backgrounds for $Z\gamma$ are outlined. The expermental cross-section is given in terms of the # observed, # of background expected as well as the acceptance and efficiency factors for determining $Z\gamma$ events.

- In Chapter 6, the kinematical properties and the determination of the cross-section $\times$ branching ratio for $Z\gamma$ are discussed and the results are tabulated and shown graphically. Furthermore, systematic uncertainties due to $Z + \gamma$ P_t distributions, Q^2 scale dependence, and Structure Function(SF) choices are described and tabulated.

- In Chapter 7, the limits on the anomalous $ZZ\gamma$ and $Z\gamma\gamma$ couplings and transition moments are obtained. The chapter concludes with a summary of results.

Chapter 2

Theory

Enrico Fermi was one of the first physicists to attempt to understand the weak interaction using the available quantum theory of his time. Unfortunately, the four-fermion β decay analogy cannot be made directly due to the fact that the propagators for the electromagnetic and weak forces are distinctly different. The photon, which mediates the electromagnetic force, is a massless pointlike particle, while the effective mass of the $e\nu$ pairs of β decay varies from process to process. However, because of the great success of Quantum Electrodynamics(QED), a theory by Richard Feynman and others in the 1940's and 1950's, it was natural to believe there was a weak analog to the photon, the intermediate vector boson(IVB), and to assume it was the mediator of the weak force. Fermi's work was important because it led the way for an eventual unification of both the electromagnetic and weak forces[1].

2.1 The Electroweak Theory

During the early 1960's, the concept of unifying the weak and electromagnetic interactions came to fruition. The resulting electroweak theory developed by Glashow, Weinberg and Salam[2] provided the framework for experimental testing which proved to be highly successful. The unification describes a gauge theory invariant under gauge transformation $\mathrm{SU(2)_L} \otimes U(1)$;for the $\mathrm{SU(2)_L}$ group this corresponds to arbitrary rotations of isospin doublets, while for the U(1) group this corresponds to phase transformations. In this model, the weakly interacting particles as members of iso-doublets, interact with coupling constant g and couple to

weak isospin doublets which are representatives of $SU(2)_L$. The electromagnetic interactions are included by introducing the U(1) group with coupling constant g' which is related to hypercharge. The existence of gauge bosons, the mediators of the weak force, is a requirement of local gauge transformation invariance. Due to the short range of these interactions the bosons must be very massive; however, invariance under $SU(2)_L \otimes U(1)$ gauge transformation only provides for massless bosons(Goldstone Bosons)[2]. To address this problem, a scalar field to spontaneously break the $SU(2)_L \otimes U(1)$ symmetry is inserted giving the Goldstone Bosons mass and leaving the photon massless. Each gauge group contains a particular weak force mediator such that

$$\begin{aligned} U(1) &\rightarrow B^{\circ}_{\mu} \\ SU(2) &\rightarrow W^{+}_{\mu}, W^{-}_{\mu}, W^{\circ}_{\mu}, \end{aligned}$$

where B° and W° mix to give both the Z boson and the photon. This theory was deemed a success with the discovery of the W and Z bosons, whose mass values were in agreement with the theory, at the CERN proton-antiproton collider.

The right-handed fermions in this model are singlets(isospin = 0), for example, e_R, μ_R, τ_R, u_R, etc.. Under $SU(2)_L$ the left-handed fermions transform as isospin doublets(isospin = 1/2), where the leptons and quarks of the i^{th} family are arranged as follows:

$$\psi_i = \begin{pmatrix} \nu_i \\ l_i \end{pmatrix} \text{ and } \begin{pmatrix} u_i \\ d'_i, \end{pmatrix}$$

where $d_i' \equiv \sum_j V_{ij} d_j$ and V is the Cabibbo-Kobayashi-Maskawa mixing matrix.

The complete Lagrangian for the electroweak theory consists of four parts

$$\mathcal{L} = \mathcal{L}_{fermions} + \mathcal{L}_{gauge} + \mathcal{L}_{scalars} + \mathcal{L}_{int}.$$

The first term describes massless fermions and is the invariant part of $SU(2)_L \otimes U(1)$. Here the gauge fields B_μ and W_μ^i are associated with the U(1) and $SU(2)_L$ groups respectively. The charged vector bosons are defined by these gauge fields to be

$$W_\mu^\pm = \frac{1}{\sqrt{2}}(W_\mu^1 \mp iW_\mu^2)$$

and the photons by a linear combination of the W_μ° and B_μ° fields. In addition, there is a second linear combination orthogonal to the photon field which describes the weak neutral current interaction. By requiring that the photon and weak neutral current vector boson be mass eigenstates, these linear combinations are given by

$$A_\mu = W_\mu^\circ \sin\theta_W + B_\mu^\circ \cos\theta_W$$

$$Z_\mu = W_\mu^\circ \cos\theta_W - B_\mu^\circ \sin\theta_W.$$

The mixing angle, θ_W, which is a free parameter of the model and must be measured experimentally, describes the mixing of the $SU(2)_L$ and U(1) sectors in the physical processes.

The second term in the Lagrangian, $\mathcal{L}_{gauge}$, describes the self-interactions of these gauge fields. The iso-doublet of the Higgs scalar field, which is introduced to break the symmetry and to provide the vector bosons with mass, is described by the third term $\mathcal{L}_{scalars}$.

Since the electric charge is related to the third component of isospin, I^3, and to the weak hypercharge, Y, the electromagnetic current is of the form

$$j_\mu^{em} = J_\mu^3 + \frac{1}{2}j_\mu^Y, \tag{2.1}$$

and the interaction Lagrangian for the physical fields can be given as

$$\mathcal{L}_{int}^{em} = -i(g\sin\theta_W J_\mu^3 + g'\cos\theta_W \frac{j_\mu^Y}{2})A^\mu \tag{2.2}$$

$$\mathcal{L}_{int}^{NC} = -i(g\cos\theta_W J_\mu^3 - g'\sin\theta_W \frac{j_\mu^Y}{2})Z^\mu. \tag{2.3}$$

By equating the electromagnetic interaction of Equation 2.2 with that of QED, $\mathcal{L}_{int}^{QED} = -ie(j^{em})^{\mu}A_{\mu}$ the electromagnetic coupling constant, e, and those of the weak force, g and g', are related by

$$e = g\sin\theta_W = g'\cos\theta_W. \tag{2.4}$$

The neutral current interaction of Equation 2.3 can be further simplified by using Equation 2.1 and the relation of Equation 2.4 to be

$$\mathcal{L}_{int}^{NC} = -i\frac{g}{\cos\theta_W}J_{\mu}^{NC}Z^{\mu}, \tag{2.5}$$

where the neutral current is given by

$$J_{\mu}^{NC} = J_{\mu}^{3} - \sin^2\theta_W j_{\mu}^{em}. \tag{2.6}$$

The form of Equation 2.5 determines that the neutral current interaction couples with strength $g/\cos\theta_W$ while the charged current couples with strength g. Furthermore, the relative strengths of the two couplings can be given in terms of the weak vector boson masses and the weak mixing angle by

$$\rho = \frac{M_W^2}{M_Z^2\cos^2\theta_W}. \tag{2.7}$$

By measuring the production rates of these gauge bosons, as well as their kinematic properties, the predicted strengths of their couplings can be experimentally tested, thus providing a direct test of the Electroweak Theory. A complete description of the Standard Model would require the larger symmetry group SU(3) $\otimes$ $SU(2)_L \otimes U(1)$ where the SU(3) group includes the gauge theory of strong interactions Quantum Chromodynamics(QCD).

2.2 $Z\gamma$ Production

In the Standard Model, the lowest order diagram leading to Z° boson production is a Drell-Yan process, as shown in Figure 2.1 for the electron-positron decay mode.

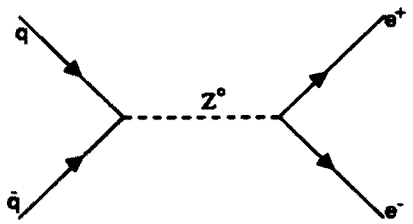

Figure 2.1: $q\bar{q} \rightarrow Z^{\circ} \rightarrow e^{+}e^{-}$

To produce photons in the final state, higher order diagrams referred to as QED radiative corrections, are needed. These internal bremsstrahlung processes, in the next to leading order in α, can be further distinguished as either radiative production or radiative decay. In the former case, we have $q\bar{q}$ annihilation producing a real Z° boson(on mass-shell), where the photon in the final state has been emitted off a quark line. For the latter case, the Z° boson is also on mass-shell but decays into $e^{+}e^{-}\gamma$ where one of the charged leptons has radiated the photon[3]. Both processes are shown in Figure 2.2.

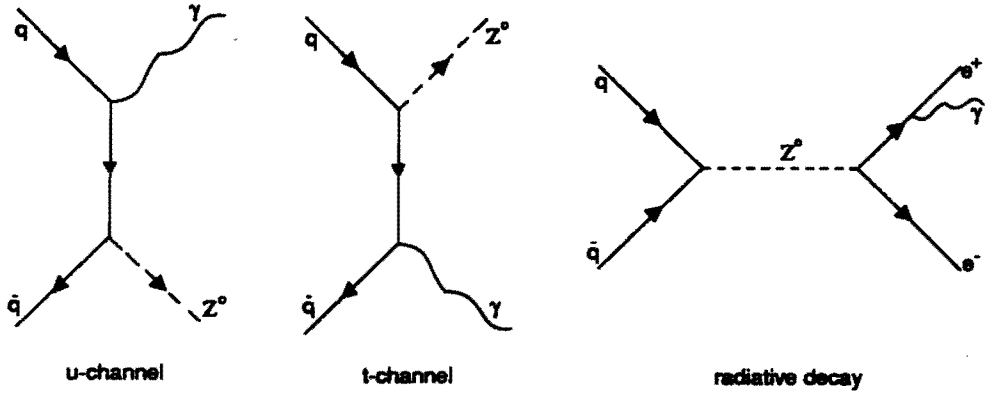

Figure 2.2: Tree level Feynman diagrams of Inner Bremsstrahlung for $Z\gamma$.

The overall cross section for the Z° will include all of these Feynman diagrams. CDF finds the cross-section times branching ratio, in the electron channel[4], to be:

$$\sigma \cdot B(Z \rightarrow e^{+}e^{-}X) = 0.209 \pm 0.013(stat) \pm 0.017(sys) \text{ nb.}$$

A comparison of these two separate radiative processes is provided in Chapter 4,

where the BAUR, WZRAD and PYTHIA Monte Carlo programs are discussed.

Berends and Kleiss[3] give a detailed description of the QED radiative corrections for these processes, with emphasis placed on radiative decay formulae. The correct theoretical form for hard bremsstrahlung events is given, which requires a specific photon energy of $k_o\sqrt{s}/2$ (k_o can take a value of 0.1% of the maximum allowed photon energy). Below this energy the photons are called soft and above which they are referred to as hard. The emisson of soft photons does not affect the kinematical process of the $Z^\circ \rightarrow l^+l^-$ but rather the size of the cross-section. It is the hard bremsstrahlung processes that give rise to radiative decays, where the cross-section for $Z^\circ \rightarrow e^+e^-\gamma$ is given by

$$\frac{d\sigma}{dp_+^o dE_\gamma d\Omega d\phi_\gamma} = \frac{1}{16S}\frac{1}{(2\pi)^5}\frac{1}{4}\sum_{spins}|M_1^Z|^2$$

and where the sum is of the form

$$\begin{aligned}\frac{1}{4}\sum_{spins}|M_1^Z|^2 &= \frac{4Se^2}{|Z(S)|^2}\{[(V_l^2+A_l^2)(V_q^2+A_q^2)-4V_lA_lV_qA_q] \\ &\times[\frac{(p_1\cdot p_+)^2+(p_2\cdot p_-)^2}{(p_+\cdot k)(p_-\cdot k)}-\frac{2m^2(p_1\cdot p_+)^2}{S(p_-\cdot k)^2}-\frac{2m^2(p_2\cdot p_-)^2}{S(p_+\cdot k)^2}] \\ &+[(V_l^2+A_l^2)(V_q^2+A_q^2)+4V_lA_lV_qA_q] \\ &\times[\frac{(p_1\cdot p_-)^2+(p_2\cdot p_+)^2}{(p_+\cdot k)(p_-\cdot k)}-\frac{2m^2(p_1\cdot p_-)^2}{S(p_+\cdot k)^2}-\frac{2m^2(p_2\cdot p_+)^2}{S(p_-\cdot k)^2}]\}\end{aligned}$$

with

$$Z(S) = S - M_Z^2 + iM_Z\Gamma_Z^{tot},$$

the couplings in the Standard Model are:

$$\begin{aligned}&V_l = -g(1-4\sin^2\theta_W), \quad A_l = -g \text{ for leptons} \\ &V_q = g(1-\tfrac{8}{3}\sin^2\theta_W), \quad A_q = g \text{ for } u \text{ and } c \text{ quarks} \\ &V_q = -g(1-\tfrac{4}{3}\sin^2\theta_W), \quad A_q = -g \text{ for } d \text{ and } s \text{ quarks} \\ &g = e/2\sin 2\theta_W,\end{aligned}$$

m is the charged lepton mass and $p_+^o(p_-^0)$ is the energy of the positive(negative) lepton.

For Standard Model Zγ production the angles at which the initial and final-state photons are produced, with respect to the beam and decay lepton directions respectively, tend to be sharply peaked. The increase in integrated luminosity proposed for the next collider run will make possible a more detailed probe of Zγ production. Furthermore, previously untested areas of electroweak interactions such as the self-interactions of the weak vector bosons themselves as shown in Figure 2.3, will be attainable.

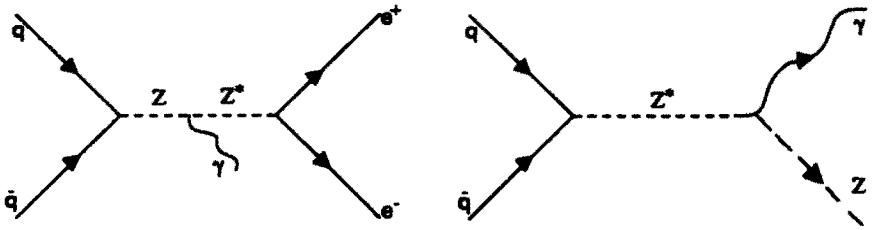

Figure 2.3: Tree level Feynman diagrams of Z-boson self-interactions.

2.3 Zγ and Non-SM Theory

In the scope of the SM at tree level, the self-interactions of the vector bosons are completely fixed by the $SU(2)_L \otimes U(1)$ gauge group structure. The $p\bar{p} \rightarrow Z\gamma$ reaction is usually studied using a restricted set of anomalous couplings[5, 6]. Also, since the Z° is its own anti-particle, any *static* electromagnetic multipole moments such as charge, magnetic dipole and/or electric quadrupole moments are not allowed at tree level[7]. Thus the SM predicts no ZZγ or Z$\gamma\gamma$ anomalous couplings at tree level.

Assuming SM couplings for the Z boson to quarks and leptons, and by using the most general form of the self-interaction vertex, ZγV, (V = γ Z) accessible in the $q\bar{q} \rightarrow Z\gamma$ process(where the quarks are effectively massless), four different anomalous couplings are allowed by electromagnetic gauge invariance and Lorentz invariance[8].

The most general anomalous $ZZ\gamma$ vertex function is given by

$$\Gamma^{\alpha\beta\mu}_{Z\gamma Z}(q_1,\ q_2,\ P)\ =\ \left(\frac{P^2-q_1^2}{M_Z^2}\right)\ \times$$

$$\left[h_1^Z\left(q_2^\mu g^{\alpha\beta}-q_2^\alpha g^{\mu\beta}\right)+\frac{h_2^Z}{M_Z^2}P^\alpha\left(P\cdot q_2 g^{\mu\beta}-q_2^\mu P^\beta\right)+h_3^Z\epsilon^{\mu\alpha\beta\rho}\ q_{2\rho}+\frac{h_4^Z}{M_Z^2}P^\alpha\epsilon^{\mu\beta\rho\sigma}P_\rho q_{2\sigma}\right]$$

where M_Z is the Z boson mass, P and q_1 are the incoming and outgoing Z boson four-momenta (Lorentz indices μ and α respectively), and q_2 is the four-momentum of the outgoing (on-shell) photon (Lorentz index β). By replacing $\left(\frac{P^2-q_1^2}{M_Z^2}\right)$ by $\left(\frac{P^2}{M_Z^2}\right)$ and the parameters h_i^Z by $h_i^\gamma, (i=1...4)$ in the $ZZ\gamma$ vertex function above, the most general $Z\gamma\gamma$ vertex function can be obtained:

$$\Gamma^{\alpha\beta\mu}_{Z\gamma\gamma}(q_1,\ q_2,\ P)\ =\ \left(\frac{P^2}{M_Z^2}\right)\ \times$$

$$\left[h_1^\gamma\left(q_2^\mu g^{\alpha\beta}-q_2^\alpha g^{\mu\beta}\right)+\frac{h_2^\gamma}{M_Z^2}P^\alpha\left(P\cdot q_2 g^{\mu\beta}-q_2^\mu P^\beta\right)+h_3^\gamma\epsilon^{\mu\alpha\beta\rho}\ q_{2\rho}+\frac{h_4^\gamma}{M_Z^2}P^\alpha\epsilon^{\mu\beta\rho\sigma}P_\rho q_{2\sigma}\right].$$

The overall $ZZ\gamma$ and $Z\gamma\gamma$ coupling strengths $g_{ZZ\gamma}$ and $g_{Z\gamma\gamma}$ are chosen to be e, where e is the proton charge. The overall factor of $P^2-q_1^2$ in the $ZZ\gamma$ vertex function is a consequence of Bose symmetry, whereas the factor of P^2 in the $Z\gamma\gamma$ vertex function is a consequence of electromagnetic gauge invariance(note that the $Z\gamma\gamma$ vertex function vanishes identically if both photons are on-shell[9]).

The form factors h_i^Z and h_i^γ are dimensionless functions of q_1^2, q_2^2 and P^2, whose values at low energies are constrained by S-matrix unitarity, and which are of the generalized dipole form[7]:

$$h_i^V(P^2=\hat{s},\ q_1^2=M_Z^2,\ q_2^2=0)\ =\ \frac{h_{i0}^V}{(1+\hat{s}/\Lambda_Z^2)^n}$$

If only one of the anomalous couplings is non-zero at a time, assuming $\Lambda_Z \gg m_Z$, then the form factors are limited by

$$|h_{10}^Z|, |h_{30}^Z|\ <\ \frac{(\frac{2}{3}n)^n}{(\frac{2}{3}n-1)^{n-3/2}}\frac{0.126\ \text{TeV}^3}{\Lambda_Z^3},$$

$$|h_{20}^{Z}|, |h_{40}^{Z}| < \frac{(\frac{2}{5}n)^n}{(\frac{2}{5}n-1)^{n-5/2}} \frac{2.1 \cdot 10^{-3}\ \text{TeV}^5}{\Lambda_Z^5}, \tag{2.8}$$

$$|h_{10}^{\gamma}|, |h_{30}^{\gamma}| < \frac{(\frac{2}{3}n)^n}{(\frac{2}{3}n-1)^{n-3/2}} \frac{0.151\ \text{TeV}^3}{\Lambda_Z^3},$$

$$|h_{20}^{\gamma}|, |h_{40}^{\gamma}| < \frac{(\frac{2}{5}n)^n}{(\frac{2}{5}n-1)^{n-5/2}} \frac{2.5 \cdot 10^{-3}\ \text{TeV}^5}{\Lambda_Z^5}. \tag{2.9}$$

A more practical case however would involve contributions from several of the anomalous couplings simultaneously, where cancellations may occur and the bounds prove weaker than those outlined in Equations 2.8 and 2.9. Let's assume that $n = 3$ for $h_{1,3}^V$ and $n = 4$ for $h_{2,4}^V$. Not only will this demand that the terms proportional to $h_{20,40}^V$ have the same high energy behavior as those proportional to $h_{10,30}^V$, but it will also guarantee that unitarity is not violated. At energies $\sqrt{\hat{s}} >> \Lambda_Z >> M_Z$, where multiple weak boson or resonance phenomena are expected to dominate, $Z\gamma$ production can be suppressed if the exponents for $h_{1,3}^V$ and $h_{2,4}^V$ are sufficiently higher than their minimum values of $n = 3/2$ and $n = 5/2$ respectively. The high energy anomalous contributions for the $Z\gamma$ helicity amplitudes grow like $(\sqrt{\hat{s}}/M_Z)^3$ for $h_{1,3}^V$ and $(\sqrt{\hat{s}}/M_Z)^5$ for $h_{2,4}^V$, and are a direct consequence of unitarity being satisfied.

The momentum dependent form factors for non-standard $ZZ\gamma$ and $Z\gamma\gamma$ couplings must vanish at large momentum transfer to ensure that S-matrix unitarity is not violated[10]. Λ_Z, which characterizes the energy above which the form factors begin to decrease, is responsible for the sensitivity limits of the anomalous couplings which are extracted from the experimental data.

Λ_Z is expected to be $\sim 100 - 300$ GeV in composite models of Z and is generally assumed to be connected to some novel interactions operative at energies $\approx \Lambda_Z$. For $p\bar{p}$ interactions at 1.8 TeV, the dependence of the sensitivity limits on the scale Λ_Z is rather strong for the $ZZ\gamma$ and $Z\gamma\gamma$ couplings h_i^Z and h_i^γ respectively, as shown in Chapter 7.

While all couplings are C−odd, only the h_{10}^V and h_{20}^V ($V = Z,\ \gamma$) parameters violate CP (i.e. violate T). As mentioned before, all the h_i^V couplings vanish in

the Standard Model for tree-level diagrams; however, at the one-loop level, only the $\mathcal{CP}-$conserving couplings h_3^V and h_4^V are non-zero. Furthermore, the higher-order SM contributions to $Z\gamma$ are also expected to be quite small, $h_{30}^Z \sim 2 \times 10^{-4}$[11].

In addition, if the Z boson was a composite particle large anomalous contributions to the h_{30}^Z and h_{40}^Z parameters would be possible, in analogy with the anomalous contributions to the magnetic dipole moments of the proton and neutron, where $\kappa_p = +1.79$ and $\kappa_n = -1.91$ due to the quark substructure of the nucleon.

The electric dipole and magnetic quadrupole transition moments for the $ZZ\gamma$ or $Z\gamma\gamma$ processes correspond to combinations of h_{30}^V and h_{40}^V, whereas the magnetic dipole and electric quadrupole transition moments correspond to the h_{10}^V and h_{20}^V combinations. The $\mathcal{CP}-$conserving electric dipole (E1) and magnetic quadrupole (M2) and the $\mathcal{CP}-$violating magnetic dipole (M1) and electric quadrupole (E2) $Z^*Z\gamma$ transition moments are given by

$$E1 = \frac{2e}{M_Z^2}\frac{k}{M_Z}\frac{k^2}{\sqrt{2}}\left(h_{30}^Z - h_{40}^Z\right) + \mathcal{O}(k^4) \text{ terms} \quad (2.10)$$

$$M2 = \frac{2e}{M_Z^2}k^2\sqrt{\frac{5}{6}}\left(2h_{30}^Z\right) + \mathcal{O}(k^3) \text{ terms} \quad (2.11)$$

$$M1 = \frac{2e}{M_Z^2}\frac{k}{M_Z}\frac{k^2}{\sqrt{2}}\left(h_{10}^Z - h_{20}^Z\right) + \mathcal{O}(k^4) \text{ terms} \quad (2.12)$$

$$E2 = \frac{2e}{M_Z^2}k^2\sqrt{\frac{5}{6}}\left(2h_{10}^Z\right) + \mathcal{O}(k^3) \text{ terms} \quad (2.13)$$

for the case of an off-shell Z^* with mass $\sqrt{\hat{s}}$ radiating to an on-shell Z and a γ with energy $k(k << M_Z)$[12, 13].

Since the Z is a neutral spin-1 Majorana particle the non-relativistic $Z^*Z\gamma$ transition multipoles will have high powers of k. Their expessions in the static limit$(k \to 0)$ are defined conventionally as[14]

$$E1 \equiv -2k\, d_{Z_T} \qquad E2 \equiv \frac{1}{\sqrt{3}}\, k^2\, Q^e_{Z_T} \quad (2.14)$$

$$M1 \equiv -2k\, \mu_{Z_T} \qquad M2 \equiv \frac{1}{\sqrt{3}}\, k^2\, Q^m_{Z_T}. \quad (2.15)$$

Therefore, on equating the above equations, the $\mathcal{CP}-$conserving electric dipole and magnetic quadrupole moments d_{Z_T} and $Q^m_{Z_T}$, and the $\mathcal{CP}-$violating magnetic

dipole and electric quadrupole moments μ_{Z_T} and $Q^e_{Z_T}$, to leading order in k, are given by[13]

$$d_{Z_T} = -\frac{e}{M_Z}\frac{1}{\sqrt{2}}\frac{k^2}{M_Z^2}\left(h_{30}^Z - h_{40}^Z\right) \quad (2.16)$$

$$Q^m_{Z_T} = \frac{e}{M_Z^2}\sqrt{10}\,(2h_{30}^Z) \quad (2.17)$$

$$\mu_{Z_T} = -\frac{e}{M_Z}\frac{1}{\sqrt{2}}\frac{k^2}{M_Z^2}\left(h_{10}^Z - h_{20}^Z\right) \quad (2.18)$$

$$Q^e_{Z_T} = \frac{e}{M_Z^2}\sqrt{10}\,(2h_{10}^Z). \quad (2.19)$$

Note: For $Z\gamma\gamma$ anomalous couplings, the $\gamma^* Z\gamma$ transition moments are not physically well defined in the static limit ($k \to 0$) since the γ^* is very far off-shell[13].

While the inclusive Z cross-section $\times$ branching ratio was measured to be $\sim$ 0.2 nb[4], the SM $Z\gamma$ cross section $\times$ branching ratio is predicted to be roughly $\sim$ 5 pb for events passing the $P_T^\gamma > 5.0$ GeV and $\Delta R_{\ell-\gamma} > 0.7$ cuts. For non-SM values of the h_i^V parameters, the $Z\gamma$ cross section varies quadratically. Furthermore, the minimum of the $Z\gamma$ cross section does not occur at the SM values of the h_i^V parameters due to the interference effects and the different $\hat{s}-$dependencies of the various terms in the overall invariant amplitude $\mathcal{M}$.

Chapter 3
Experimental Apparatus

The Fermi National Accelerator Laboratory(FNAL) contains a proton-antiproton collider which produces center of mass energies of 1.8 TeV. Using this powerful tool, the exploration of many aspects of the Standard Model can therefore be achieved as well as probing for new phenomena. There are two main ingredients involved in this exploration: the accelerator itself and the CDF detector, the former producing the proton-antiproton collisions and the latter analyzing the final state particles produced in the collision. This chapter contains a brief description of both components with emphasis on the detector elements used in this analysis.

3.1 The Accelerator

The colliding of protons and antiprotons at the Fermi National Accelerator Laboratory is a multi-step process. First a beam of 750 KeV H^- ions is created by a Cockroft-Walton generator and injected into a linear accelerator, where the energy of the ions is increased to approximately 500 MeV. The H^- ions are stripped of their two electrons just before injection into a circular booster ring where the bare protons are boosted to 8 GeV. The protons are then injected into the Main Ring. This synchrotron(2 km in diameter) also houses the ring of superconducting magnets used to accelerate the particles to 900 GeV and is called the Tevatron. Once the protons reach 120 GeV, some are extracted to create antiprotons while the rest are accelerated to even higher energies of 150 GeV and injected into the 900 GeV Tevatron. Figure 3.1 is an overhead view of the entire accelerator system.

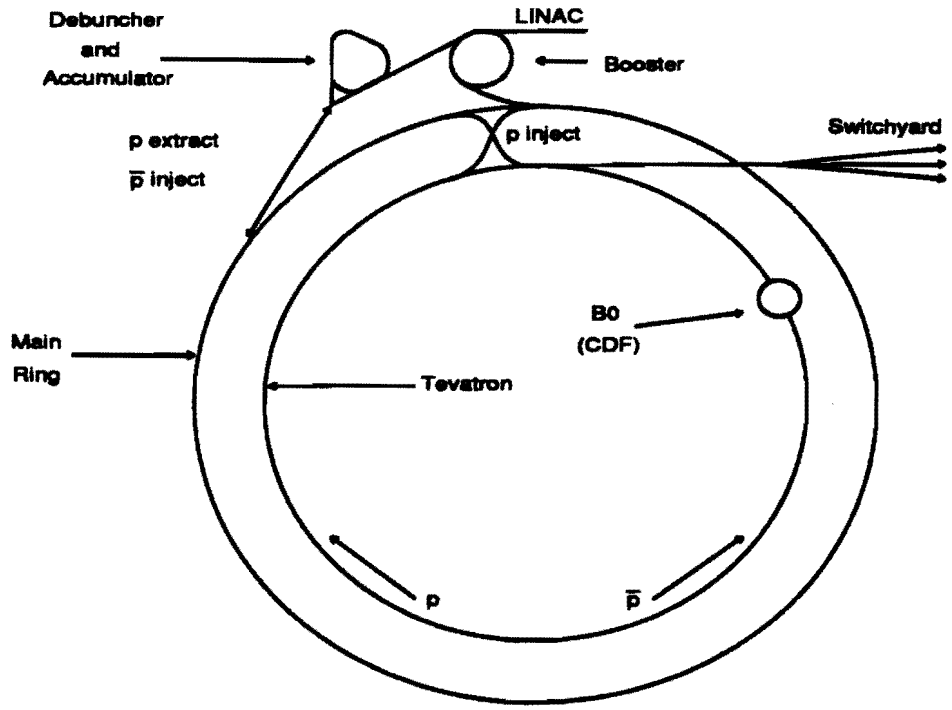

Figure 3.1: Overhead view of the Fermilab accelerator. The fixed target beam lines are shown as well as the position of the B0 intersection where the CDF detector is located.

In pre-Tevatron days, the Main Ring was used to produce beams of 400 GeV protons for the fixed-target experiments.

As alluded to above, the production of antiprotons is accomplished by smashing the 120 GeV extracted protons into a tungsten target. These antiprotons initially have large momentum spreads(on the order of 8 - 13 GeV/c). Those $\overline{p}$'s of about 9 GeV/c, or a momentum spread of about 3%, are injected into the Debuncher by using a "strong focusing magnet" called a lithium lens. To obtain an almost monoenergetic beam of antiprotons, both bunch rotation and stochastic cooling are used to reduce the energy spread and the transverse motion of the beam respectively [15]. Bunch rotation is a technique which uses radio frequencies to increase the time spread of the $\overline{p}$ pulse which in turn reduces the energy spread. Stochastic cooling senses the beam position by using a probe which translates a signal to kicker electrodes and results in beam corrections. Every two seconds the antiprotons are

directed into the Accumulator which continues stochastic cooling and doubles as a storage container for the particles. The antiprotons stored in the Accumulator become compact and have energy distributions which are very narrow. Once a large number of antiprotons are generated, six bunches are then extracted and injected into the Main Ring. As was the case for the protons, the antiprotons are then accelerated to 150 GeV and directed into the Tevatron.

Once in the Tevatron, the $p\overline{p}$ beams are manipulated by requiring their respective radio-frequencies to be out of phase. This method is called cogging and is implemented to ensure the intersection of the beams at different points around the ring. Since the p and $\overline{p}$ travel in opposite directions, the method requires two independent accelerating systems.

The Luminosity, or rate at which the protons and antiprotons collide, is defined to be:

$$\mathcal{L} \equiv \frac{N_p N_{\overline{p}} C}{4\pi\sigma^2}$$

where N_p and $N_{\overline{p}}$ are the total number of protons and antiprotons per bunch respectively. C is the bunch crossing rate, and σ is the rms width of the beam profile. Both beams are assumed to have the same rms width and to overlap completely. A luminosity of 2×10^{30} cm^{-2}s^{-1} would require a crossing rate of approximately 88 KHz.

The rms width is defined to be:

$$\sigma^2 \equiv \frac{\epsilon\beta(s)}{6\pi}$$

where $\beta(s)$, the Beta function of the accelerator, describes the transverse envelope of the beam. It is a function of the beam position in the ring and is determined by focusing magnets. The emittance, ϵ, is a measure of the transverse phase space occupied by the beam. This quantity is independent of the beam position and increases with time.

The Luminosity is increased by decreasing the rms width. This is accomplished

by using the superconducting quadrupole magnets, which focus the beam and reduce the $\beta(s)$ at the collision point. Since the emittance, ϵ, grows with time and some of the protons and antiprotons are lost in the collisions, the Luminosity falls exponentially; approximate beam lifetimes are on the order of 12 hours. For the 1988 - 1989 run, the peak luminosity ranged from 3×10^{29} cm^{-2}s^{-1} to 2×10^{30} cm^{-2}s^{-1}.

At 1.8 TeV the total inelastic cross-section for $p\bar{p}$ collisions is approximately 77 mb. (1 mb = 10^{-24} cm^2). However, a large fraction of final state particles go undetected because they scatter at small angles and traverse down the beampipe. Scintillation counters which surround the beam pipe can only detect final state particles at angles of 1.25° or greater. So the inelastic cross-section for $p\bar{p}$ interactions, where at least the final state particles are $\geq 1.25°$, is 44 mb.

The total number of collisions produced is defined as the integrated luminosity. Figure 3.2 shows the integrated luminosity delivered by the accelerator for the 1988 - 1989 run and the integrated luminosity collected by the CDF detector. The overall efficiency for data collection was approximately 50% for this run.

3.2 The Collider Detector at Fermilab (CDF)

The CDF multi-purpose detector was constructed to analyze the physics processes of $p\bar{p}$ interactions at center-of-mass energies of 1.8 TeV. Charged particle tracking and fine-grained calorimetry are examples of detector designs used in event analysis.

A right handed coordinate system is used in which the positive z-axis is parallel to the direction of the proton beam with a vertical y-axis and an x-axis pointing radially outward. ϕ is defined as the azimuthal angle, while the polar angle θ is measured from the proton beam and the pseudorapidity, $\eta \equiv -\ln\tan(\theta/2)$, is an approximately Lorentz invariant distribution variable of the polar angle appropriate for longitudinal phase space.

A cut-away view of the CDF detector is shown in Figure 3.3. A detailed description of all components is provided in Ref.[16]. A summary of the components used in this analysis follows.

3.2.1 Tracking Detectors

The Vertex Time Projection Chamber(VTPC) located closest to the beampipe determines charged particle trajectories in the r-z plane. It contains 8 chambers which measure 3.5 meters along the beam direction, centered at z= 0 and extending radially from 7 cm to 21 cm. Each chamber is comprised of two drift volumes separated by a high voltage electrode and extending 15.25 cm in the z direction. Located at the end of each drift volume are octagonal proportional chambers which are divided into octants of 24 sense wires and 24 cathode pads. To eliminate problems at octant boundaries and to obtain good azimuthal information, adjacent octants are rotated relative to each other by 11.3°. By extrapolating from r-z back to the beam axis the position of the track can be determined with a resolution of 1 mm[17].

The Central Tracking Chamber(CTC)[18] is an axial wire chamber encased in a superconducting solenoid magnet of central field 1.4116 Tesla. The CTC consists of 84 layers of wires grouped into 9 superlayers. Five of these superlayers contain twelve sense wire planes, positioned parallel to the beam and magnetic field, for determination of track curvature and particle momentum. The other 4 are comprised of small stereo wires where each layer has 6 sense wires. These sense wires are all positioned at stereo angles of $\pm 3°$ and measure the angle of tracks with respect to the beam axis.

The electric field of the CTC, which is oriented 45° to the radial direction is designed to insure that the drift velocity remains fixed. Electrons drift at an angle relative to the direction of the E field so the cells in each chamber are tilted with respect to the magnetic field to maintain an azimuthal drift direction (see Figure 3.4).

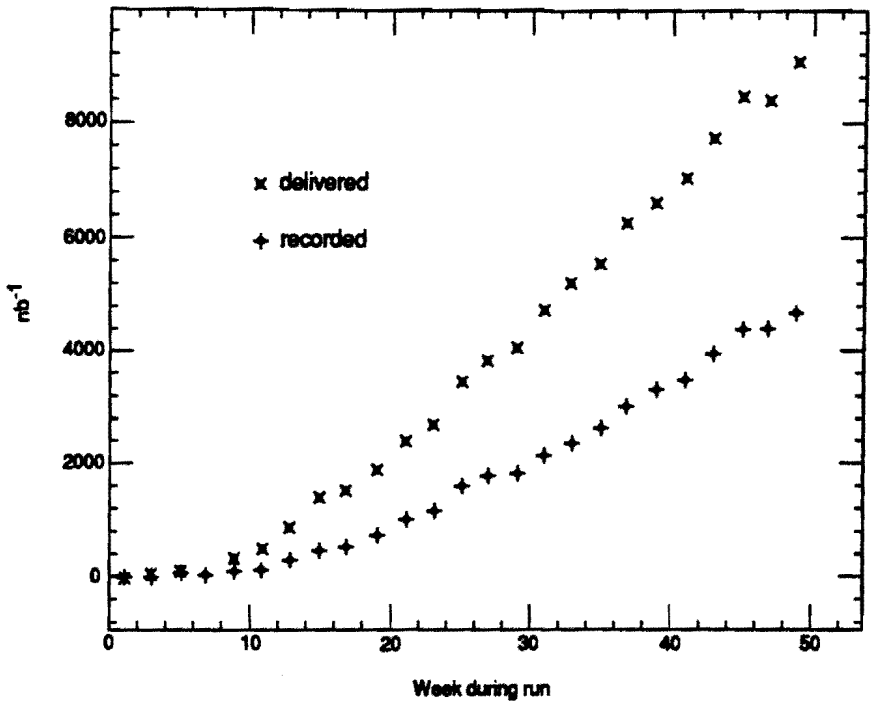

Figure 3.2: The Integrated Luminosity delivered by the Accelerator and recorded by the CDF detector.

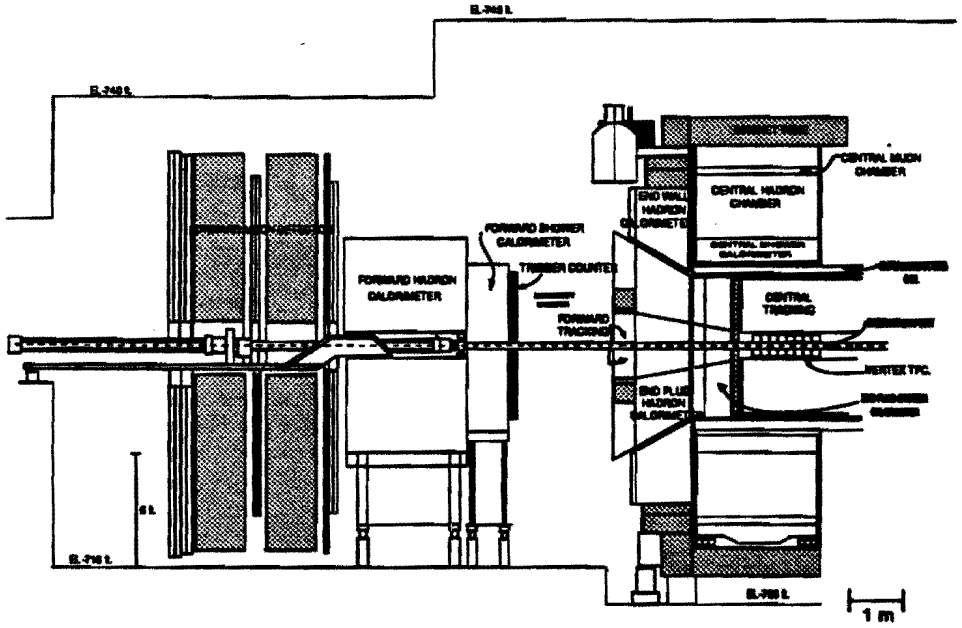

Figure 3.3: Cross section through a vertical plane of one half of the CDF detector. The detector is symmetric about the midplane and roughly symmetric around the beam axis.

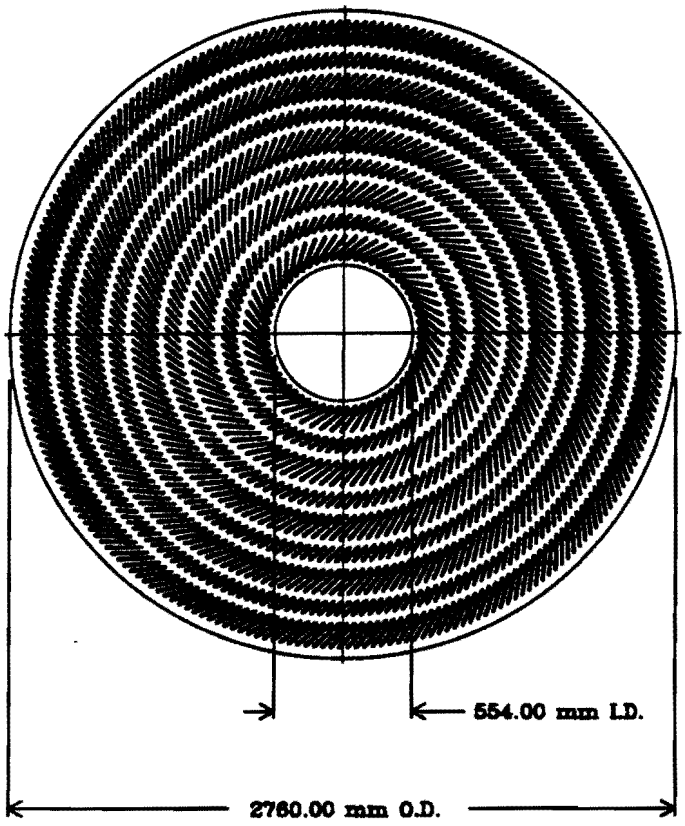

Figure 3.4: $R-\phi$ view of the CTC. There are 9 superlayers and each of the $R-\phi$ cells are tilted by 45°.

The momentum resolution of the CTC alone for isolated tracks is approximately $\sigma_{p_t} = 0.002$ x ${p_t}^2$. However, by including the VTPC which gives a well defined vertex position, the effective tracking radius is extended from 100 to 130 cm. This reduces the overall momentum resolution to about $\sigma_{p_t} = 0.0011$ x ${p_t}^2$.

3.2.2 Calorimeter Detectors

CDF calorimetry coverage is complete in azimuth and extends to about 2° of the proton-antiproton beams in polar angle. Projective towers of polar angle segmentation in pseudorapidity, η are used and point towards the interaction point. The calorimeters are grouped into regions; the Central ($|\eta| < 1.1$) with towers 15° wide in ϕ and 0.1 in η, the Plug ($1.1 < |\eta| < 2.4$) and the Forward ($2.4 < |\eta| < 4.2$) with towers 5° in ϕ and 0.1 in η. While lead and steel are the interactive medium for the electromagnetic and hadronic calorimeters respectively, the collection or sampling media are regionally dependent. In the Central calorimeter scintillator is the sampling medium, while for the Plug and Forward regions gas proportional chambers, with segmented cathode pad readout, are the sampling media.

The identity of an electron, for example, is determined by the amount of energy that an incident track deposits in the electromagnetic portion of the calorimeter. Photons on the other hand deposit this energy without the presence of an incident track.

Central Calorimeters

The Central Electromagnetic(CEM)[19] and Central Hadronic (CHA)[20] Calorimeters are comprised of 48 wedges each 15° in phi and positioned around the Central Tracking Chamber(CTC) for complete azimuthal coverage. The CEM consists of 31 layers of 5 mm thick polystyrene scintillator interspersed with 30 layers of $\frac{1}{8}$ inch thick aluminum-clad lead sheets. As the polar angle changes, an average thickness of 18 radiation lengths is maintained by replacing some of the lead with acrylic and

by painting black the scintillator behind this acrylic. The scintillator light is collected by wavelength shifters located on either side of the wedge and is transmitted to acrylic light guides attached to photomultiplier tubes. There are two photomultiplier tubes per wedge positioned in the rear of the wedge at the extremes. Figure 3.5 is a cutaway view of a single wedge which contains 10 towers (from 0 at $\theta = 90°$, to 9).

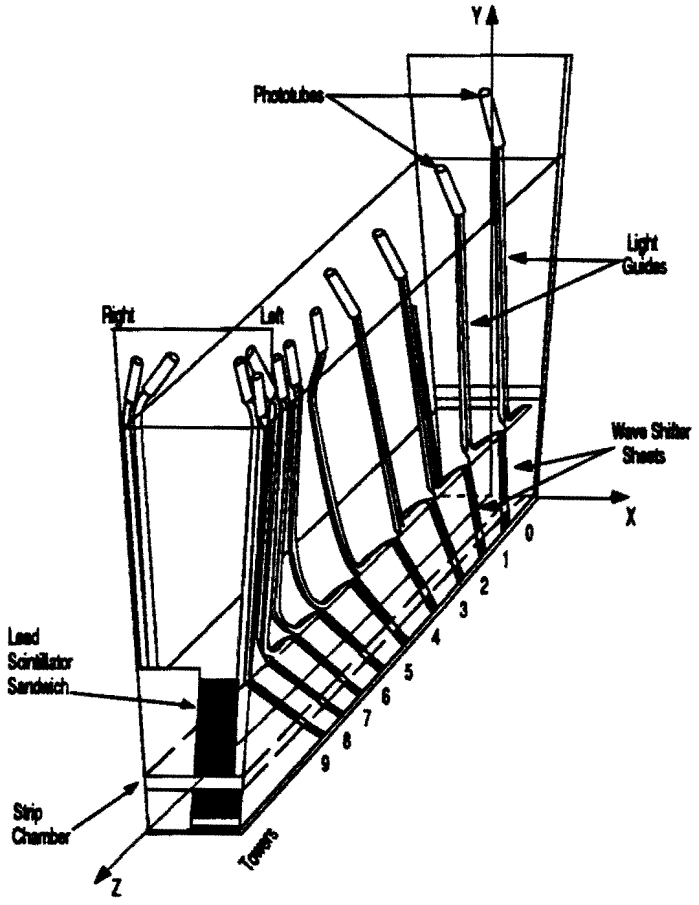

Figure 3.5: Cutaway view of a calorimeter wedge showing the central electromagnetic calorimeter, the light transmission system and the central strip chamber position.

A 50 GeV electron testbeam was used initially to calibrate each of the CEM towers. This calibration is maintained to about 1% for a few years by cross calibrating with Cs^{137} source signals[21]. Individual tower response from testbeam data fluctuates some 6% over its face because of shower leakage at the edges and variations in

light collection[22]. The measured energy resolution for the CEM is:

$$(\frac{\sigma_E}{E})^2 = (\frac{13.5\%}{\sqrt{E \sin\theta}})^2 + (1\%)^2$$

where the constant term is the average uncertainty in individual tower calibration.

Included in the CEM at shower maximum, or approximately 6 radiation lengths, is a gas proportional chamber(CES) which measures the position and shape of the electromagnetic shower. Sixty-four wires positioned parallel to the beam gather information in ϕ, while 128 strips perpendicular to the wires give z information. Position resolutions in both the strip and wire views for 50 GeV testbeam electrons are on the order of 2 mm. By measuring the charge deposition on the orthogonal strips and wires single photons are separated from multiple photon background. In addition, the Central Electromagnetic Strip Chambers(CES) provide more precise measurements of the z and ϕ positions of the electromagnetic cluster. Figure 3.6 shows the orientation of the cathode strips and anode wires. The CES determines(at shower maximum) the position and transverse development of an electromagnetic shower by measuring the charge deposition on the strips and wires[16].

The CHA measures hadronic energy and consists of 32 layers of 1.0 cm scintillator sandwiched with 2.5 cm of steel. Each wedge is comprised of 8 towers in η and in all towers a thickness of approximately 4 absorption lengths is maintained. As in the CEM light is collected by wavelength shifters and transmitted to acrylic light guides. Testbeam pions are used to initially calibrate the towers and this calibration is also maintained by Cs^{137} sources. Typical resolutions for 50 GeV pions is $(\frac{\sigma}{E}) \sim 11\%$.

Plug Calorimeters

The Plug Electromagnetic(PEM)[23] and Plug Hadronic (PHA)[24] calorimeters are gas proportional chambers whose coverage in polar angle extends 10° - 30° and 150° - 170° ($1.1 < |\eta| < 2.4$). When particles shower in the calorimeter the gas is ionized and electrons move towards the anode wire, leaving behind positive ions

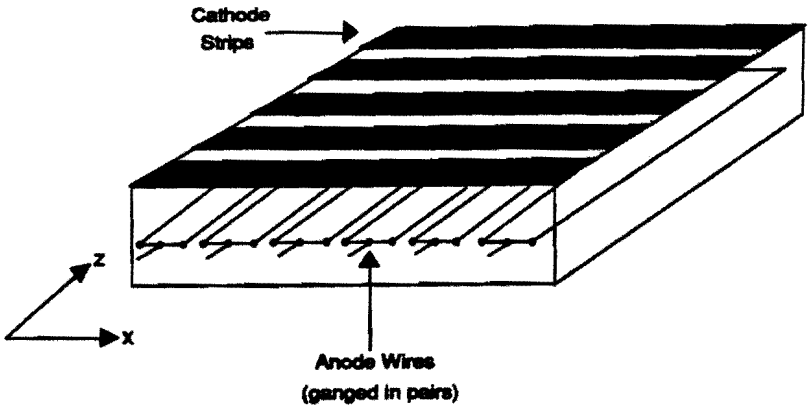

Figure 3.6: Orientation of the CES strip and wire chambers.

which induce charge on cathode pads. Since the gain is a function of the density and composition of the gas, a small system of proportional tubes and Fe^{55} sources is used to monitor the gas. If the particle's energy from the Fe^{55} source is known and deposited in the tube the gas-gain is determined by measuring the charge collected by the anode wire. The response as a function of gas-gain is measured using testbeam calibrations and data are adjusted on-line for gas-gain on a run to run basis before being written to tape.

The PEM is comprised of 34 layers of proportional tubes divided into four quadrants with 2.7 mm lead absorber panels between each layer. Figure 3.7 shows the stacking of a single quadrant.

The proportional tubes are made of resistive plastic strung with gold plated tungsten wire. The cathode pads form projective towers containing 3 radial depth segments of 5, 24 and 5 layers respectively. These segments are used for collecting information on longitudinal shower development. The anode signals for each layer in the quadrant also provide additional longitudinal information. Similar to the CEM, near shower maximum, there are 10 layers of finely segmented cathode strips in η and ϕ as well as cathode pads. The coverage extends from $1.2 < |\eta| < 1.9$ and

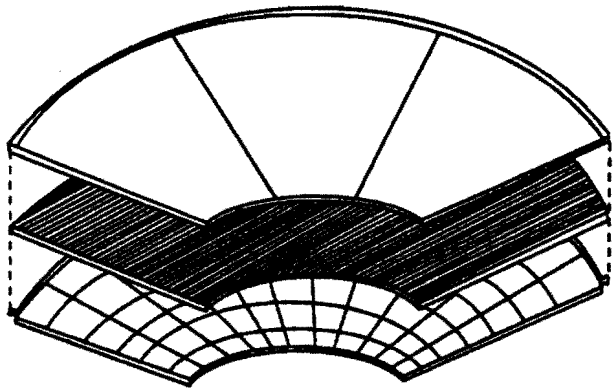

Figure 3.7: Exploded view of a layer of the proportional tube array, PC board with pad patterns and PC board for the ground plane.

provides better position and shape resolution. The resolution of the PEM obtained by an electron test beam is $(\frac{\sigma}{E}) \sim (\frac{28\%}{\sqrt{E}})$.

The PHA is divided into twelve 30° stacks and contains 24 layers of proportional tubes separated by 5 cm of steel. Cathode pads form projective towers and the anode signals are read out for each layer in the stack. The resolution obtained by a pion testbeam is $(\frac{\sigma}{E}) \sim (\frac{86\%}{\sqrt{E}})$.

Forward Calorimeters

The Forward Electromagnetic Calorimeter(FEM)[25] is divided into quadrants and covers the region from 2° to 10°($2.4 < \eta < 4.2$). The quadrants consist of 4.5 mm lead sheets sandwiched between 30 layers of proportional tubes. Projective towers with 2 depth segments are formed by cathode pads which are gathered in groups of 15 layers. Each anode plane is observed separately where the 90° anode plane has been divided into 5 regions. The energy response is calculated using electron

testbeam data and is linear up to 100 GeV. The resolution is measured to be

$$\frac{\sigma}{E} = \frac{25\%}{\sqrt{E}} + 0.5\%.$$

The Forward Hadronic Calorimeter(FHA)[26] is composed of 27 layers of proportional tubes with 5 cm steel plates interspersed and is also divided into quadrants. The anode planes for 6 different regions as well as the projective towers of the cathode pads are read out. Since the low-β quadrupoles of the accelerator cover part of the FHA, the small angle coverage is diminished to a full azimuth of only $|\eta| < 3.6$. The energy resolution for the FHA is approximately given by

$$\frac{\sigma}{E} = \frac{140\%}{\sqrt{E}}.$$

Before the system writes any forward calorimeter data to tape, variations in gas gain are corrected.

3.2.3 Triggers

The trigger system for CDF is a four stage design[27]. The initial trigger, Level 0, is both a minimum bias trigger and a luminosity monitor and is also referred to as the Beam-Beam Counter(BBC). The two planes of scintillation counters are located $\approx \pm 5.8$ meters from the nominal interaction point and directly in front of the forward/backward calorimeters. Events are selected from the inelastic collisions by requiring that at least 1 of the 16 time of flight counters, located on either side of the interaction point, be hit. This must occur within a 15 ns window centered on the beam crossing. The decision to process the event is made available within 100 ns of the collision and if valid will inhibit data gathering until the next trigger level decision.

The Level 1 trigger makes use of fast analog signals[27]. These signals are formed into trigger towers of $\Delta\eta = 0.2$ and $\Delta\phi = 15°$ and weighted by $\sin\theta$ for a crude estimate of transverse energy. Large energy deposits in the trigger towers are determined by analog comparators and summers(counters) which calculate the total

scaler transverse energy in the event. For W and Z selection, there must be at least 6 GeV found in a single trigger tower. The processing decision is made within 3.5μs which is the time between beam crossings. If the event is valid, data taking will remain inhibited until the next trigger level decision, otherwise the electronics is reset in time for the next beam crossing after the initial Level 0 trigger.

The Level 2 trigger digitizes the fast analog signals of Level 1 and utilizes data from the Central Fast Tracker(CFT)[28]. This fast hardware track processor uses fast timing information from the CTC to detect high transverse momentum tracks. The digitized calorimeter information is used to form energy clusters and the energy, position, width and track data are passed to programmable processors. Here simple algorithms identify physics signals: 1) the transverse energy of the cluster must be greater than 12 GeV; 2) the transverse momentum of the CFT track must be greater than 6 GeV/c and point at the cluster; and 3) the hadronic to electromagnetic ratio must be less than 12.5%. Level 2 requires 10μs for its decision and will reset the frontend electronics if no Level 2 trigger is satisfied. If this trigger is satisfied however, the entire event is digitized, formatted and then sent to Level 3 for further processing.

The Level 3 trigger system is comprised of 60 Motorola 68020 processors and is completely software based[29]. All data in the event are accessed and streamlined versions of the CDF offline reconstruction code are implemented. The electron clusters and associated tracks of Level 2 are required to be reconstructed with at least 12 GeV and 6 GeV/c respectively by the Level 3 filter. Events which pass these algorithms are written to tape.

The final event sample for $Z \rightarrow e^+e^-\gamma$ events is obtained via the inclusive Z data set, which uses the central electron trigger. That is, a central electromagnetic cluster with $E_t > 12$ GeV, matched to a track with $P_t > 9$ GeV/c. The details of obtaining this set are discussed in the next chapter.

Chapter 4
Methods of Analysis

This chapter describes the various steps needed to obtain a proper data sample for this analysis and the use of event generators for comparison. Section 4.1 begins by explaining event reconstruction for electrons from raw data. The event selection routines are described in section 4.2 followed by Monte Carlo simulation techniques in section 4.3.

4.1 Event Reconstruction and Selection

The process of event reconstruction begins with raw ADC and TDC data, which are quickly analyzed using on-line triggers before some are selected for further processing. Once written to tape the events will be tested further with physics dependent requirements. The end result is a sample set of Z° events which are then searched for extra isolated hard photons.

4.1.1 Energy Reconstruction

Reconstruction of electrons from the ADC calorimeter data requires that certain energy corrections be made to the raw data due to problems with amplifier gain, gas gain and huge pedestal offsets. These corrections are applied by the Data Aquisition System(DAQ) before the events are written to tape. The original ADC data are converted to energy by multiplying by a detector dependent conversion factor which has been determined from testbeam studies. An $\eta - \phi$ array of the calorimeter tower energies is created as well as a list of the anode plane energies.

In the gas calorimeters, some of the anode wires will not record any energy deposition because of broken wires[30]. This reduces the amount of signal seen in the grouped cathode pad towers and so the energy of the tower is corrected to compensate. Pedestal shifts which are fairly small are corrected for in offline analysis. Unfortunately the CDF calorimeter tower array does contain noise for various reasons:

- Anomalously large signals in single phototubes in the central calorimeter. This is due either to high voltage breakdown in the phototube itself or it is caused from Čerenkov light of particles which shower in the light guides. By requiring that both phototubes in each tower register some energy, this problem can be alleviated.

- Hadronic showers of low energy neutrons, which penetrate the calorimeters, interact with the Hydrogen gas giving rise to bare protons. The ionization which fills these proportional tubes appears as a large energy deposit in a few cathode pads for a single layer of the calorimeter. An algorithm is used to search for and weed out highly localized energy deposits.

- Localized high voltage leakage in the ends of the PEM tubes produces large signals in a single anode layer for a small number of cathode pads. The algorithm mentioned above is also used to remove these energy spikes.

4.1.2 Electron Identification

As mentioned briefly in Chapter 3, the final data sample is obtained by matching a central electromagnetic cluster of $E_t > 12$ GeV to a track of $P_t > 9$ GeV/c. This is the clustering algorithm invoked for electron identification.

Clustering

The process begins by searching the $\eta - \phi$ calorimeter tower array for seed towers with $E_t^{em} > 3$ GeV. The adjacent towers in the array are associated with the seed tower if they contain an $E_t^{em} > 0.1$ GeV. These tower energies are then added to the seed tower to form the cluster energy. The clustering algorithm will continue its search for the next seed tower until one of two conditions is met; (1) if an adjacent tower is found containing less than the threshold energy or (2) if the predetermined size of the cluster, which is regionally dependent, has been reached.

The cluster size depends on the calorimeter. For the central calorimeter the $\eta - \phi$ array is a 3×1(0.3 in eta by 0.26 in phi), for the plug calorimeter it is a 5×5 and for the forward calorimeter it is a 7×7.

The electromagnetic clusters formed are required to contain an energy of $E_t^{em} >$ 5 GeV to be retained. Furthermore, while the hadronic energy in the cluster, E_t^{had} is summed separately from the electromagnetic, the ratio of $E_t^{had}/\ E_t^{em}$ must be less than 0.125.

Once all clusters have been formed the reconstructed tracks are looped over and extrapolated back to the calorimeters. If a track lies within the electromagnetic cluster region, then the one associated with the highest P_t is taken to be the electron track.

Energy Corrections

All calorimeter energies are compared to an absolute momentum scale as determined by the CTC. A few corrections must be applied to these energies to compensate for the variations in each calorimeter type and for relative tower response. Timing offsets, drift velocities and beam position on a run to run basis are used to calibrate the CTC. The beam's center position is determined within 5μm for a 50μm beam size in the r-ϕ plane.

The drift velocities and TDC offsets are calibrated using charged particle tracks from minimum bias events. The TDC pedestal offset, t_o, for each channel is obtained by requiring tracks be continuous when crossing the plane of sense wires in a single $r-\phi$ cell. By demanding continuous tracks crossing the boundary between two $r-\phi$ cells, the drift velocity is determined. Knowing the wire positions, the t_o offset and the drift velocity one can convert the TDC track data into $r-\phi$ positions. The t_o and drift velocity data are analyzed online for each run and written to database files which are later used in offline track reconstruction.

Azimuthal alignment errors in the CTC wires were studied using 17000 inclusive electrons. By equalizing the mean E/P distribution for positrons and electrons in this sample, azimuthal offsets for each of the 84 wire layers were obtained. This alignment was checked using cosmic rays in the following way. To the track reconstruction algorithm, cosmic rays which traverse the CTC and pass near the beam axis will appear as two oppositely charged tracks which originate from the same vertex. If they are aligned correctly then these two reconstructed tracks will have the same curvature and reconstructed vertex position.

The CTC momentum scale is known using a J/Ψ sample with an absolute magnetic field uncertainty of $\pm 0.05\%$. The dominant contribution to this uncertainty stems from the fact that the solenoid was operated at a current of 4650A but mapped at a current of 5000A[31]. A sample of $J/\Psi \rightarrow \mu^+\mu^-$ events was used to check the results of the momentum scaling and measurement of the J/Ψ mass agreed with the published values within its 0.03% statistical uncertainty[32].

In the central region there were three energy corrections applied to CEM data.

- Electron tower response varies and from testbeam data this variation is found to be $\sim$6% across the tower face. The strip position is recorded and then a position dependent correction is applied.

- Tower-to-Tower response varies and is found to be an $\sim$3% variation. The

E/P distribution of 17000 inclusive electrons is used to get an average of the relative tower response.

- An overall correction factor of $1.0194 \pm 0.0024\%$ is determined by comparing the E/P distribution of a sample of 1800 $W \rightarrow e\nu$ events with that obtained using a radiative Monte Carlo generator. This process enables the CEM energy scale and the absolute momentum scale of the CTC to be matched[33, 34].

In the plug calorimeter three energy corrections must be applied.

- Calorimeter tower-to-tower variations of $\sim$6% are found using electron test-beam data. Each quadrant is measured and a correction factor is applied.

- Calorimeter response is non-linear for high energy electrons. This nonlinearity is measured in the testbeam to be $\sim$7% at 200 GeV.

- Quadrant-to-quadrant variations measured from Z^0 events where one lepton is confined to the CEM. Correction factors are determined by constraining the average Z mass found in each quadrant to the average mass from a quadrant whose response is well measured from the testbeam.

In the forward calorimeter two energy corrections are needed.

- Calorimeter response is non-linear for high energy electrons. The nonlinearity is measured in the testbeam up to 200 GeV. Unlike the plug calorimeter though there can be longitudinal boosts and the electron energies from Z^0 decay can be as high as 400 GeV. Testbeam results are then extrapolated by measuring the average Z mass as a function of FEM electron energy, where one lepton must be in the CEM. By constraining the CEM-FEM masses to the CEM-CEM Z^0 mass the energy nonlinearity is determined. This correction increases the cluster energy by as much as 10% for 200 GeV electrons.

- Quadrant-to-quadrant variations are measured using the energy spectrum neutron induced energy spikes. These data are in good agreement with the quadrant to quadrant variations seen in the Z° data.

For transverse momenta typical of W & Z decays, the CTC track fitting code reproduces track curvatures to better than 0.1%, thus a conservative estimate of the momentum scale is set to 0.2% for high momentum tracks.

Electron Quality Parameters

The separation of true electrons from jets and other backgrounds requires that specific parameters be checked. For all calorimeters then both the ratio of E_t^{had} / E_t^{em} and an isolation quantity, I, are defined. The isolation of the electron is defined to be: $I \equiv \frac{E_t^{cone} - E_t^{em}}{E_t^{cone}}$, where E_t^{cone} is defined to be the total transverse energy in a cone of radius $R = (\Delta\eta^2 + \Delta\phi^2)^{1/2} < 0.4$ centered on the electromagnetic cluster.

The production of low energy charged particles along with some jets fragmenting into very energetic π^o's, makes it difficult to distinguish whether or not the electromagnetic track associated with the cluster comes from a single electron. The decay of the π^o into two photons which deposit their energy in the EM calorimeter may be matched with a track left by the low energy charged particles. Similar problems arise with the low energy spray of particles or underlying event which is a direct result of the $\bar{p}p$ collisions. Backgrounds of this type can be removed to a certain exent by invoking the HAD/EM and Isolation quality parameters mentioned above.

In addition to these two overall quaility parameters, each specific calorimeter has other quantities which it uses to insure the selection of good electrons. These quantities are defined using the shower shapes as determined in an electron testbeam[35].

- CEM: In this calorimeter there are 4 additional parameters.

  1. E/P: Ratio of the cluster energy to the matched CTC track momentum.

2. LSHR: Measure of the lateral shower distribution of energy in the cluster. The z-position of the electron shower as measured using the strips in conjunction with other testbeam parameters is used to predict the energy distribution among the towers of the cluster. The measured distribution is then compared with this prediction. The quantity LSHR is defined by

$$\mathrm{LSHR} = 0.14 * \sum_i \frac{\mathrm{E}_i^{adj} - \mathrm{E}_i^{prob}}{\sqrt{0.14^2 * \mathrm{E} + (\Delta \mathrm{E}_i^{prob})^2}}$$

where E_i^{adj} is the measured energy in the tower adjacent to the seed, E_i^{prob} is the expected energy in that tower based on the strip information, E is the cluster energy and $\Delta \mathrm{E}_i^{prob}$ is the uncertainty on E_i^{prob} with a 1 cm uncertainty in the strip measurement.

3. χ^2_{strip}: Measure of the shower shape in the strip chambers. The energy distribution of the cathode strips is compared with the parameters derived from the electron testbeam.

4. Δx,Δz: Difference in x and in z, in centimeters between the strip cluster and the extrapolated CTC track.

- PEM: There are two additional electron selection parameters in this calorimeter.

1. $\chi^2_{3\times3}$: Measurement of transverse shape of the calorimeter cluster. The energy distribution of the towers in the 3×3 region centered on the seed tower is compared to electron testbeam parameters.

2. VTPC occupancy: A "road" which begins at the collision point and points at a calorimeter cluster is defined(with a loose track requirement). The occupancy is defined to be the number of VTPC hits detected in this road divided by the number of VTPC wires crossed by this road. If the road is too near an internal VTPC structure(edge) the occupancy is set to 1.0 by default.

- FEM: There is a single quality parameter invoked for electron selection in this calorimeter.

    1. $\frac{E_{front}}{E_{total}}$: Ratio of the cluster energy deposited in the front half of the FEM to the total energy deposited. Real electrons will deposit most of their energy in the 1st half of the forward calorimeter.

Figures 4.1 and 4.2 show the distributions of various electron quality parameters in the Z° data sample. For each of the parameters, the electrons are required to pass all quality cuts except for the one being plotted.

4.2 Event selection

The standard procedure for the processing of events begins with what is referred to as production code. The ADC calorimeter data is converted into energies using full track reconstruction and algorithms are implemented which can identify particle types(e.g. electron, jet, muon algorithms). Events with one or more electromagnetic clusters are written to tape. This tape is then processed by applying a simple program which includes more electron energy quality cuts and results in the initial W and Z data samples.

The Z° events must have two electromagnetic clusters with a transverse energy greater than 10 GeV, while the $W^{\pm}$ events must contain one CEM cluster of $E_t >$ 10 GeV and whose missing transverse energy, $\not\!\!E_t$, is greater than 20 GeV. $\not\!\!E_t$ is an indirect measure of neutrinos with large transverse momentum that can escape the detector without interacting.

These candidate events are written to a second summary tape where final event selection is made using the energy corrections mentioned above. All energy dependent quality parameters are recalculated for this sample. For samples of well measured W and Z's to be produced, this second data tape must pass more restrictive quality cuts and energy thresholds as well as additional fiducial, event vertex

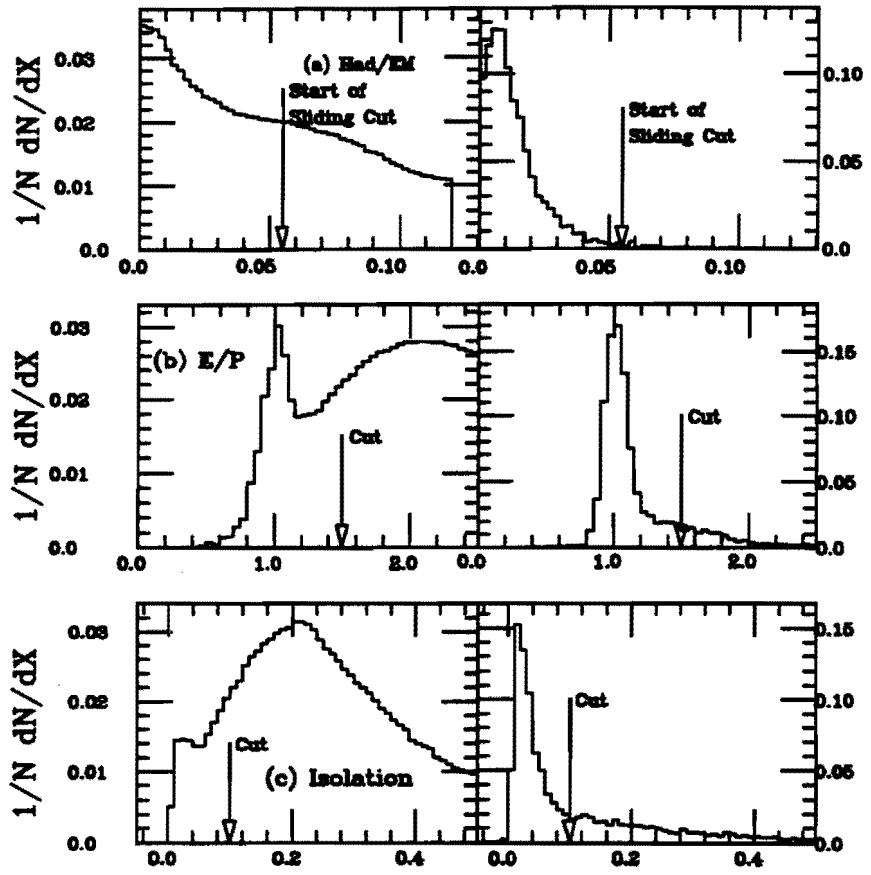

Figure 4.1: Electron quality cut distributions for Had/EM, E/P and Isolation. The left-side plot of the parameters contains only those cuts intrinsic to the trigger and the 20 GeV P_t cut, while the right-side plot shows the distributions with all quality cuts applied except for the one being plotted[36].

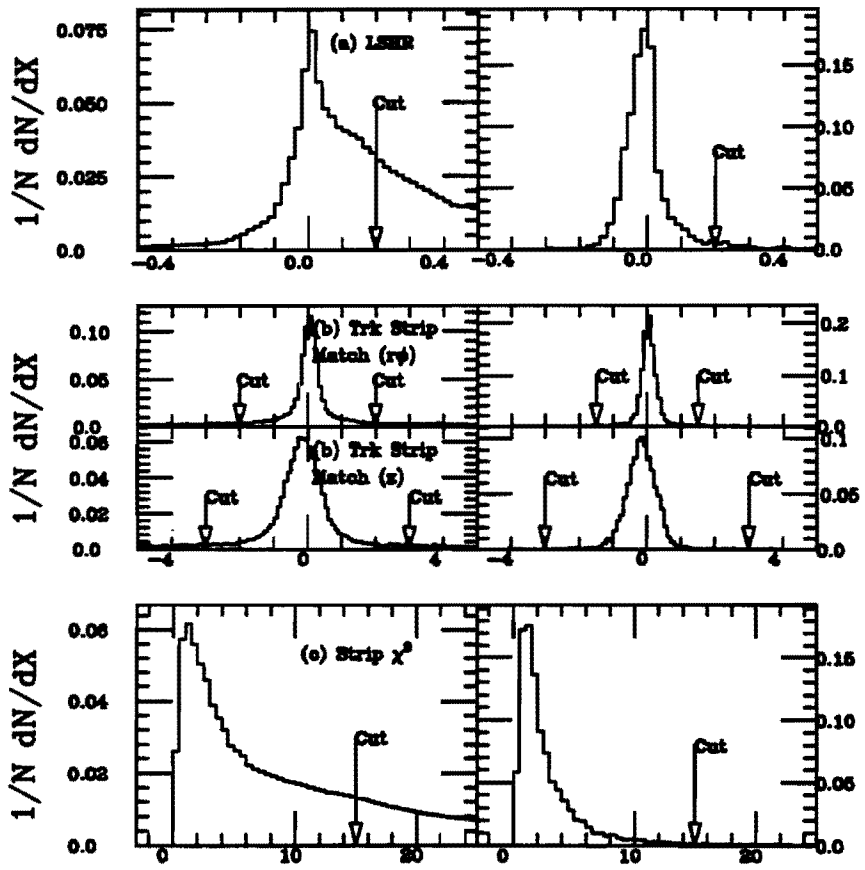

Figure 4.2: Same as Figure 4.1 for the electron quality cuts LSHR, $r\phi$ and z track match and the strip chamber χ^2[36].

and trigger requirements.

These samples are referred to as the "Standard W & Z Data Sets"[35] and were used for the electron and muon W & Z cross-section times branching ratio[37] and W/Z cross-section ratio analyses[38]. They are also the sets used for the $Z\gamma$ & $W\gamma$ analysis. The uncertainty associated with the total inelastic $\bar{p}p$ cross-section, which was determined from the BBC to be $\sigma_{BBC} = 46.8 \pm 3.2$ mb[38], is the primary uncertainty attributed to the integrated luminosity and is $\approx 6.8\%$. The integrated luminosity in the electron channel for the 1988-1989 CDF run was $\int \mathcal{L}dt = 4.05 \pm 0.28 \text{pb}^{-1}$. Before discussing photon selection a brief description of the quality cuts used to obtain these starting samples is warrented.

4.2.1 Fiducial Requirements

W & Z samples are restricted to detector areas where the calorimeter response is well understood and where the energies can be reliably measured. In general this means avoiding cracks and dead space between modules.

In the CEM, there are a few additional restrictions applied.

1. Dead spaces between adjacent wedges are excluded by requiring that the extrapolated track position be within 21 cm in ϕ of the tower center. That is electrons must be 3 cm from the 15° wedge boundary.

2. The crack, located at $\theta = 90°$, between two halves of the central calorimeter is excluded by requiring the extrapolated track position to have $|z| > 9$ cm.

3. The cluster's seed tower can not be the outermost tower in the central wedge. The projective tower geometry for this tower is somewhat extreme, where large amounts of radiator and scintillator were removed to maintain a constant thickness in radiation length and large energy corrections are applied.

4. The superconducting solenoid contains some cryogenic and electrical material

which penetrates one of the calorimeter wedges. This wedge contains 7 normal towers, one highly modified and two which are missing. The electrons are excluded from these missing and modified towers.

In the PEM, the EM clusters are restricted from the border regions and dead towers as follows:

1. The seed tower can not be in any towers which are adjacent to the ϕ boundary between quadrants.

2. The seed tower can not be in the two outermost or the two innermost eta annuli. This excludes the cracks between the CEM-PEM and the PEM-FEM.

3. The seed tower is excluded from the 16 dead PEM towers; of these 16 towers, 13 are in regions excluded already by the quadrant boundaries.

For the FEM, the EM clusters are restricted from quadrant borders and from regions with partial hadronic coverage by:

1. The seed tower can't be in any towers adjacent to the ϕ boundary between quadrants.

2. The seed tower can't be in the 5 innermost η annuli, which excludes the low beta quads which penetrate the FHA and limit the hadronic coverage in this region.

4.2.2 Vertex Requirement

The $\bar{p}p$ collisions can occur at points other than the nominal interaction point of the detector. The VTPC tracks which determine the position are Gaussian distributed about the nominal interaction point with a sigma of 30 cm. Since projective tower geometry can be distorted for large vertex displacements and some particles from displaced vertices can escape without detection through cracks between the

plug and forward calorimeters, detector geometry is preserved by requiring that events have their vertex positions within ±60 cm of the nominal interaction point.

4.2.3 Electron Trigger Requirement

All events must pass the Level-2 or ELECTRON_12 trigger requirements which are as follows:

1. EM cluster in CEM with $E_t > 12$ GeV
2. Ratio of Hadronic to Electromagnetic transverse energy, E_t^{had} / $E_t^{em} < 12.5\%$
3. Track from the fast track processor is matched in ϕ to the calorimeter cluster and has $P_t > 6$ GeV

Prerequisites to the Level-2 trigger include a valid Level-0 trigger from the Beam-Beam Counters and a Level-1 trigger which requires at least one CEM trigger tower with $E_t > 6$ GeV

The Level-3 trigger was introduced in the last part of the run and used the ELECTRON_12 trigger as a prerequisite. This trigger calculated the LSHR variable and used a more sophisticated tracking algorithm to ensure the $P_t > 6$ GeV threshold. The final analysis requirements for the W and Z analyses were more restrictive than the Level-3 algorithm, thus the fundamental trigger efficiency of the Level-2 trigger was used.

4.2.4 The Z sample

The standard W & Z data sets were made from the 5.1 EWK spin version which contains a common sample of central, high-P_t electron candidates. An initial requirement of a central electron cluster is imposed with the following properties:

- A transverse energy of the central EM cluster of $E_t > 20$ GeV

- Had/EM $< 0.055 + 0.00045 * E$, where E is the total energy of the EM cluster in GeV
- Isolation I $\equiv \frac{(E_t^{cone} - E_t^{cluster})}{E_t^{cone}} < 0.1$, in a cone of $\Delta R = \sqrt{\Delta\eta^2 + \Delta\phi^2} = 0.4$ centered on the EM cluster(location defined from CES shower centroid information)
- The event vertex be within $|Z_{vertex}| < 60.0$ cm of the nominal Z = 0.0 position
- The electron cluster have $|\eta| < 1.1$ and be within the good fiducial region of the CEM calorimeter
- The total EM cluster energy divided by the CTC track momentum, E/P $<$ 1.5
- Using 11-channel clustering in the strip view, the CES strip χ^2 for a fit of testbeam electron shower profiles to the leading cluster profile must each be $\chi^2_{strip} < 15.0$
- Lateral shower shape, $L_{shr} < 0.2$, comparing the observed lateral shower profile to testbeam electron lateral shower profile
- A single reconstructed 3-dimensional track associated with the EM cluster must match the CES position within $|\Delta z| < 3.0$cm and $|\Delta R - \phi| < 1.5$ cm

A total of 5012 events passed the above requirements. The electron Z candidates are then obtained by additionally requiring a second EM cluster located in either the central, plug, or forward calorimeters which also are in a good fiducial region and satisfy the following criteria:

- A transverse energy of the second EM cluster of $E_t > 10.0$ GeV
- Had/EM < 0.1

- Isolation I $\equiv \frac{(E_t^{cone} - E_t^{cluster})}{E_t^{cone}} < 0.1$, in a cone of $\Delta R = \sqrt{\Delta\eta^2 + \Delta\phi^2} = 0.4$ centered on the EM cluster(location defined from CES shower centroid information)

- In the central region, a second EM cluster is required to have a 3-dimensional track associated with it and an E/P < 2.0

- In the plug region, a second EM cluster is required to have a 3×3 $\chi^2 < 20.0$ and a VTPC hit fraction > 0.5 in a road centered on the PEM cluster

- The invariant mass of the two selected EM clusters lies between $70 < M_{ee} < 110$ Gev/c^2

A total of 243 events satisfy the electron Z requirements.

4.2.5 Photon Selection

An additional photon event selection routine was applied to the standard Z data set to obtain the electron $Z^o\gamma$ data sub-set. Before subjection to this selection routine however, the original standard Z data set was reclustered with lower seed tower and sum E_t thresholds, E_t (seed) = 1.0 GeV & E_t (sum) = 1.5 GeV . The reclustering is needed because the original energy clustering algorithm used to obtain the Z data sample unfortunately contains inefficiencies at the $E_t > 5$ GeV threshold. These inefficiencies are due mainly to the fact that the seed tower and the summed cluster energies are calculated with raw energies as discussed in section 4.1.2 and also their E_t is determined using the $z = 0$ position instead of the actual event vertex. The energy response map, which is position dependent and the energy corrections, as previously described, were applied to this reclustered data. The cluster's transverse energy was determined using the actual event vertex and then the original threshold of $E_t > 5$ GeV was implemented.

These threshold effects were studied using Monte Carlo(MC) generated photons which were simulated in the detector by the QFL program(described in section 3 of this Chapter). Flat distributions of photon energies from $0.5 < E_t < 12.5$ were generated in all calorimeters and the results were compared with those obtained with the default clustering algorithm. Figure 4.3 shows the efficiencies of each calorimeter for the default clustering of E_t (seed) = 3.0 GeV & E_t (sum) = 5.0 GeV, versus the reclustered MC photons of E_t (seed) = 1.0 GeV & E_t (sum) = 1.5 GeV. Based on this study, the default clustering isn't fully efficient for the CEM/PEM/FEM until E_t of about 6/9/8 GeV respectively.

A photon candidate from this reclustered Z data sample was then required to satisfy the following:

- There must be a 1-3$(\phi - \eta)$ tower cluster of EM energy deposited in the central calorimeter of at least $E_t \geq 5$ GeV, after position response & CEM energy scale corrections have been applied. This assumes a seed tower energy of at least $E_t \geq 1.0$ GeV.

- The location of the CEM cluster is required to be in a good fiducial region of the central as defined by the CES shower centroid position.

- The distance between the Z decay leptons and the photon, $\Delta R_{e\gamma}$, must be greater than 0.7(which corresponds to an opening angle of $\sim 40^{\circ}$ in the r-ϕ plane). This cut is used to suppress the contribution of radiative decay diagrams to the signal.

- The extra E_t deposited in a cone of $\Delta R = 0.4$ centered on the CEM cluster, but not including the EM cluster, must be < 2.0 GeV(ET4 < 2.0 GeV).

- The extra summed P_t due to charged tracks within a cone of $\Delta R = 0.4$ centered on the CEM cluster must also be < 2.0 GeV($\sum$PT4 < 2.0 GeV). The tracks used in the sum must have a $|Z_{vtx} - Z_o| < 10$ cm.

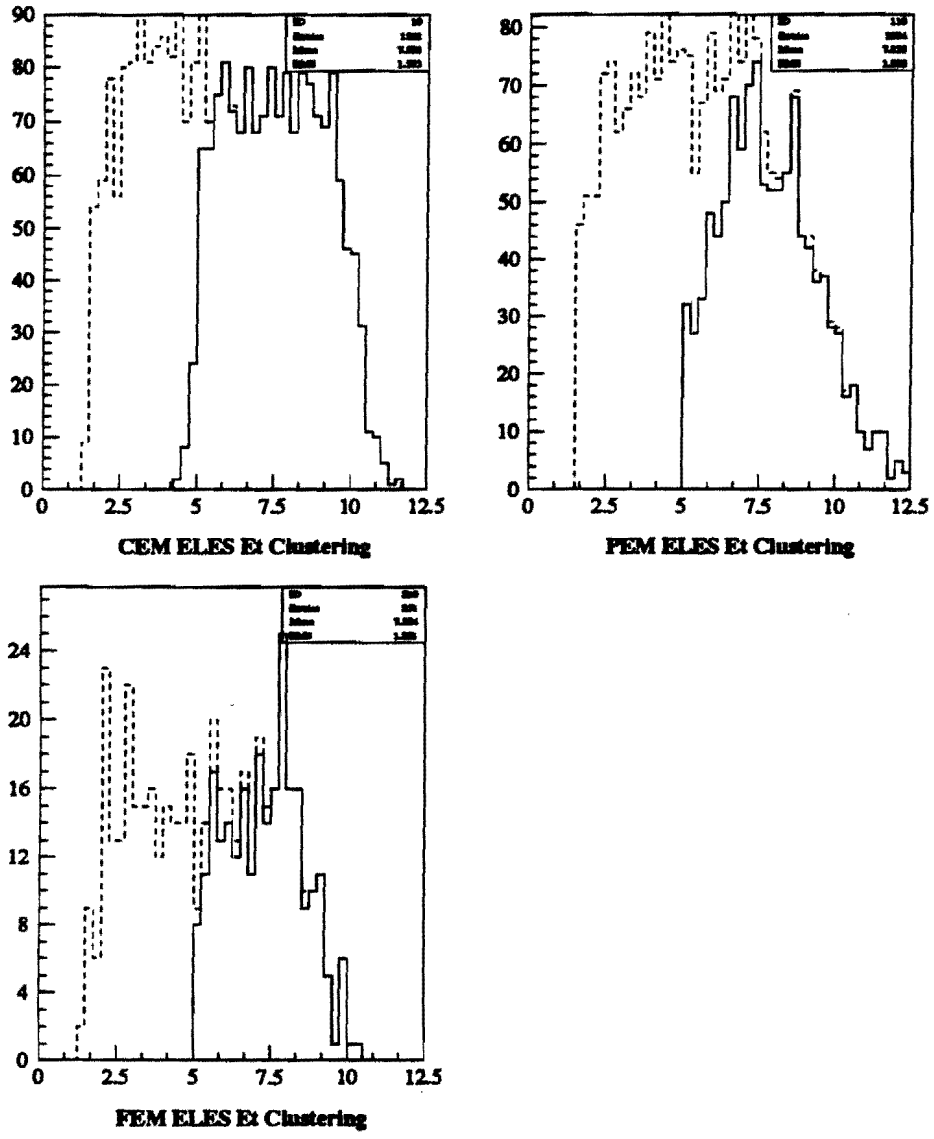

Figure 4.3: QFL MC determination of the clustering efficiencies for the CEM, PEM and FEM. The solid histogram is the default clustering and the dashed is reclustered with Seed=1.0, Sum=1.5[39].

- No 3-dimensional CTC track can point to the EM cluster from any vertex(N3D=0).

- A Had/EM $< 0.055+0.00045*$E, where E is the total energy of the EM cluster in GeV.

- Have a lateral shower shape for the CEM cluster of $L_{shr} < 0.5$.

- Using 11-channel clustering in both the strip and wire views, the CES strip and wire χ^2's of a fit of testbeam electron shower profiles to the leading cluster profile must each be < 20.0.

- There must be no 2nd CES strip or wire clusters with an energy greater than 1 Gev, $E_{CES\ 2^{nd}} > 1$ GeV, within the CEM cluster. This requirement is used to further suppress π^o and multi-photon backgrounds.

Figure 4.4 and Figure 4.5 show distributions of these photon quality parameters. For each parameter, the photons are required to pass all succesive quality cuts except the one being plotted. Notice that once the calorimeter isolation cut, ET4, is applied the remaining two events survive all other imposed requirements.

4.3 Monte Carlo Simulation

To understand the experimental data, the technique of computer event generation based on current theories is implemented in conjunction with detector simulated routines. That is, events are made randomly by a computer and then subjected to a simulated version of the device used to detect real data. The results of this Monte Carlo simulation and the real experimental data are then capable of comparison.

In this analysis the major event generator used is the Baur Monte Carlo(MC) for the $Z\gamma$ processes[7]. This MC contains all Feynman diagrams for the process including additional anomalous coupling graphs. Two other event generators, WZRAD

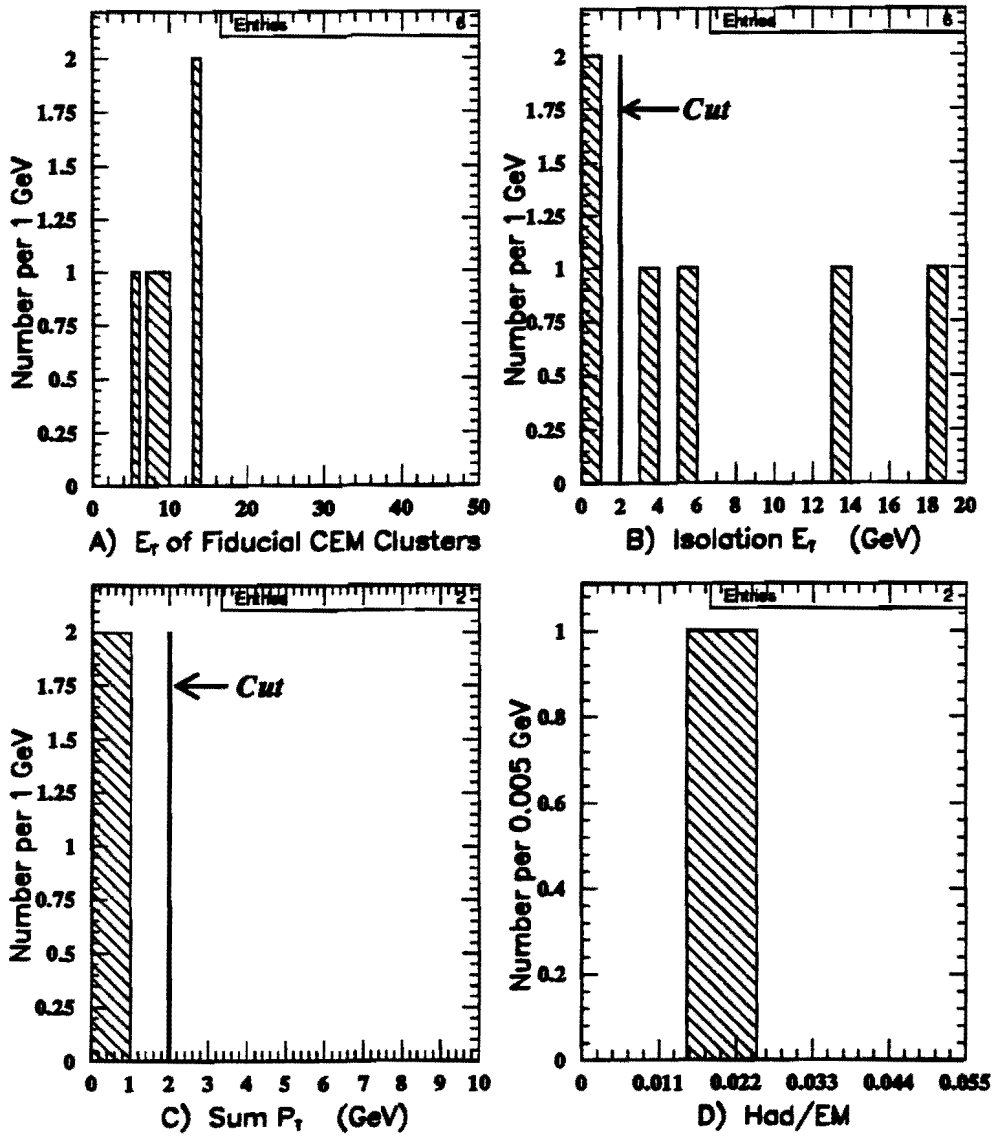

Figure 4.4: Photon quality cut distributions for Cluster E_t, Isolation E_t, ΣP_t and Had/EM. Where the distributions with all quality cuts applied except for the one being plotted are shown.

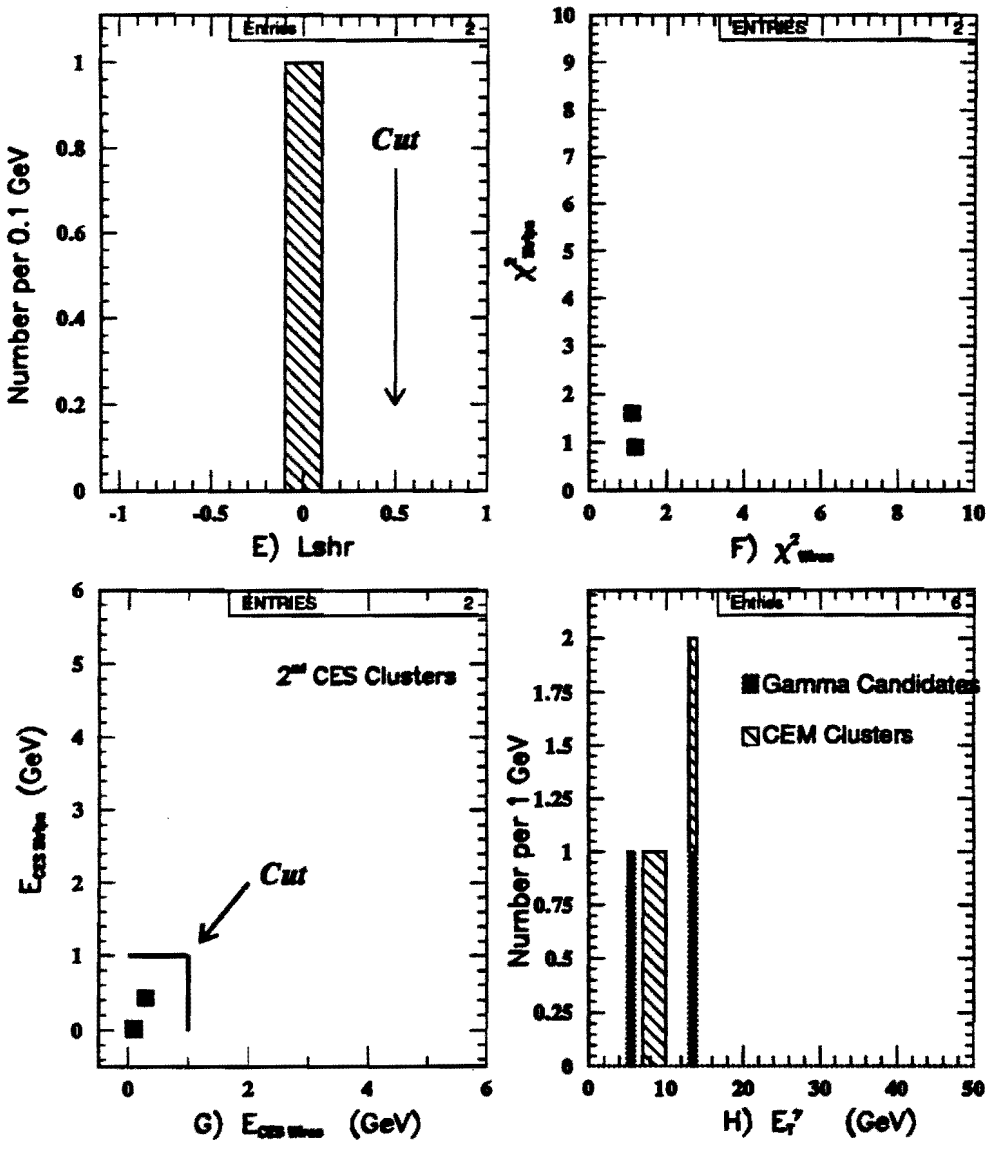

Figure 4.5: Same as Figure 4.4 for the Lshr, χ^2_{strip} vs χ^2_{wire}, $E_{CES\ wires}$ vs $E_{CES\ Strips}$ and Photon E_t.

and Pythia, were used to show differences between radiative decay off final state decay leptons and radiative production off initial state quark lines, respectively. Both of these are commonly referred to as inner-bremsstrahlung processes. The results for this analysis do not use these two MC's since neither is able to completely model the $Z\gamma$ process as in the Baur case; however, comparisons of the three separate programs are made in section 4.3.2 and are in good agreement with each other.

The detector simulation programs used come in two varieties; a Fast detector simulator[40, 41] and QFL. Both are complete detector simulations which include energy reconstruction and specific detector corrections. Each program simulates parameters such as underlying event, P_t boosts, fiducial geometry, $\sum E_t$ and vertex smearing. The major difference between QFL and the Fast simulator is that the latter doesn't have the handicap of the Analysis-Control(AC) package. AC allows the user to interface directly with the analysis package.

4.3.1 The Baur MC

The Baur Monte Carlo, the first complete $Z\gamma$ generator, generates weighted events. The contributions of each of the Feynman diagrams in Figures 2.2 and 2.3 are added together by implementing a helicity-amplitude formalism. The kinematic phase space for the system is created by the VEGAS routine, a multi-dimensional integration code[42]. The calculated cross-section includes a k-factor of $[1+\frac{8\pi}{9}\alpha_s(M_V^2)] \approx 1.35$ to account for higher order QCD processes such as $q+\overline{q} \rightarrow g + V + \gamma$ and $q+g \rightarrow q + V + \gamma$. We have compared the Baur MC radiative Standard Model results with the following additional Monte Carlo's;ISAJET[43], PAPAGENO[44],PYTHIA[45] and WZRAD[46]. The cross-section determined using the Baur MC is in good agreement with these other MC's.

Initially large samples of greater than 500,000 events are generated with as few kinematic cuts as possible. This limits any biases which may result from the detectors' finite resolution and smearing effects and allows as much of the

total $Z\gamma$ cross-section as possible. In addition it is important for obtaining the $(h^Z_{30,10} - h^Z_{40,20})\sigma \cdot B(Z+\gamma)$ surfaces for $ZZ\gamma$ and $Z\gamma\gamma$ anomalous couplings. At the generator level, the kinematic cuts used are as follows: $P_t^l > 1.0$ GeV, $P_t^\gamma > 1.0$ GeV, $\Delta R_{l-\gamma} > 0.3$, $|\eta_l| < 6.0$ and $|\eta_\gamma| < 6.0$. For events which pass these initial kinematic cuts, the 4-vector momentum information is written to an unformatted output file. The original Monte Carlo has been modified to include the lastest PDFLIB[47] structure functions(SF), version 3.10 and includes all parton-parton luminosities. For this analysis however, the HMRS-B SF is taken for nominal as was done in the W/Z analysis. The systematic uncertainties associated with these SF's, as well as P_t and Q^2-scale dependencies will be discussed in Chapter 6.

The Fast Detector Simulator

As was done for the W & Z analysis[40], a similar fast detector simulation routine was used in the $Z\gamma$ analysis. The main purpose of this program is to determine both geometric and kinematic acceptances. It is also used to obtain the predicted cross-section for $Z\gamma$ events above the Z selection cuts and photon selection cuts of $\Delta R_{\gamma-l} > 0.7$ and $E_t^\gamma > 5.0$ GeV. By inputting all relevant electron and photon efficiencies, the number of expected events in the CDF electron $Z\gamma$ data sample can be obtained. The electron efficiencies are the same as those used in the W/Z analysis. The determination of both electron and photon efficiencies will be discussed in the next chapter.

The unformatted 4-vector files which are output from the generation level, are read in by this fast detector routine. Each event is given a random P_t boost according to the "nominal" P_t distribution based on the Z boson P_t distributions[48]. The Z-vertex of the event is obtained from a Gaussian distribution, $\sigma_z = 30$ cm. The electron and photon energies are smeared by the appropriate detector resolution, CEM/PEM/FEM. These smeared electrons and photons are propagated from the event vertex through the solenoid and into the calorimeter. Fiduciality of these

particles is determined using a modified stand alone version of the standard FIDELE routine.

QFL Simulation

Similar to the fast detector simulation, QFL is a complete detector simulation program. It will account for energy corrections and known detector problems such as cracks, thereby fully reconstructing the event as if it had been real data.

The Baur MC output files are not directly input into QFL; first the events are unweighted according to the procedure outlined in CDF-note 1665[49]. These unweighted distributions are then processed through the ISAJET routine to properly simulate the underlying event. Some parameters in ISAJET are tuned so that the underlying event is in decent agreement with that observed in the electron Z data sample. Once this is accomplished, the tuned output is sent through the QFL '88-'89 detector simulation routine. The QFL output is then directly input into an the same analysis as for the Z sample, but with the added photon analysis, making sure that the proper production code(version 4.6) is implemented for reconstruction.

Table 4.1 summarizes the predicted number of SM $Z\gamma$ events based on the fast MC detector simulation and the Baur QFL/ISAJET MC; the uncertainty expressed is statistical. In addition the contribution from Drell-Yan, (DY) + $Z\gamma$ is listed. This contribution is small but is corrected for in the F_{DY} term as listed in Chapter 5, Table 5.2.

Table 4.1: $Z\gamma$ MC Predictions.

Baur Monte Carlo	Prediction
Fast $Z\gamma$:	1.15 ± 0.11
Fast $Z + DY\gamma$:	1.19 ± 0.11
QFL $Z\gamma$:	1.37 ± 0.18

4.3.2 Comparison of Baur, WZRAD and Pythia Monte Carlo's

As previously mentioned, the WZRAD and Pythia Monte Carlo's illustrate the two radiative processes for $Z\gamma$. The radiative production events are generated using Pythia[45], where the total cross-section for the desired process is calculated. The WZRAD Monte Carlo[46] generates both $Z \rightarrow e^+e^-$ and $Z \rightarrow e^+e^-\gamma$ events, where the photon radiates off the final-state electrons. Although the Baur, WZRAD and Pythia Monte Carlo's are independent programs there is reasonable agreement between the combination of WZRAD & Pythia with the Baur MC. For example, the Baur and WZRAD programs use HMRSB structure functions whereas Pythia uses ELHQ-1 and it is not interfaced with PDFLIB. In addition, the WZRAD MC consists only of a very rudimentary gaussian P_t -boosting subroutine.

The number of events generated for the Baur MC was 500,000 where $\approx$ 50,000 events passed all cuts. For Pythia 50,000 events were generated and $\approx$ 5000 passed, while for WZRAD 2 million events were generated and $\approx$ 200,000 survived. The generated cross-sections determined from each program are:

$$\begin{aligned}
\sigma_{gen}^{Baur} &= 17.722 \pm 0.055 \text{ pb} \\
\sigma_{gen}^{Pythia} &= 4.428 \pm 0.024 \text{ pb} \\
\sigma_{gen}^{WZRAD}\dagger &= 125.086 \pm 11.529 \text{ pb.}
\end{aligned}$$

† The WZRAD generator cross-section is obtained from the relation

$$\sigma * BR(WZRAD)_{gen} = \sigma * BR(Z) * f_{rad}$$

where $\sigma * BR(Z) = 217.0 \pm 20.0$ pb and $f_{rad} = 0.5764310$ is the fraction of generated events which are radiative. The photon cuts used at the generator level in WZRAD create photons down to $E_\gamma = 100$ MeV.

while the cross-section after cuts was determined to be:

$$\begin{aligned}
\sigma_{cuts}^{Baur} &= 4.619 \pm 0.041 \text{ pb} \\
\sigma_{cuts}^{Pythia} &= 1.476 \pm 0.028 \text{ pb} \\
\sigma_{cuts}^{WZRAD} &= 2.109 \pm 0.196 \text{ pb} \\
\sigma_{cuts}^{WZRAD\&Pythia} &= 3.585 \pm 0.200 \text{ pb.}
\end{aligned}$$

To compare this MC with the others we must determine the total number of $Z\gamma$ events for each program. To do this we use the following equation:

$$N_{Z\gamma} = \sigma_{cuts} \cdot \mathcal{L} \cdot \epsilon_{overall}$$

where $\mathcal{L}$ is the Luminosity for electron data and $\epsilon_{overall}$ is the efficiency or the total number of events passing all cuts divided by the total number of events generated.

For illustative purposes, the combination of detector acceptance and cut efficiencies gives overall efficiency estimates of:

$$\begin{aligned}
\epsilon_{overall}^{Baur} &\approx 50000/500000 = 0.1 \pm 0.4\% \\
\epsilon_{overall}^{Pythia} &\approx 5000/50000 = 0.1 \pm 1.0\% \\
\epsilon_{overall}^{WZRAD} &\approx 200000/2000000 = 0.1 \pm 0.2\%
\end{aligned}$$

Table 4.2 contains the actual values of the total number of $Z\gamma$ events based on the actual efficiency calculations for each MC as determined by the Fast detector simulator.

Table 4.2: $N_{Z\gamma}$ events for the Baur, Pythia and WZRAD MC's.

MC	$N_{Z\gamma}$
Baur	1.773 ± 0.150
Pythia	0.792 ± 0.068
WZRAD	0.937 ± 0.120

As was discussed in section 2.2, angular distributions between the charged leptons and the produced photons are indicators of the different radiative processes. In a

three body decay, for instance, the minimum angle between the photon and its parent electron will be fairly small(collinear). For radiative production however the photon is not created from the decay particles of the Z° but rather comes from the quark lines and the angular separations can be quite large. Figure 4.6 shows the minimum angle between the electron and photon in the rest frame of the Z° for the three MC's, where each has been normalized to the real data. The $\Delta R_{min}(e\gamma)$ cutoff of 0.7 is apparent and all three MC's are compatible.

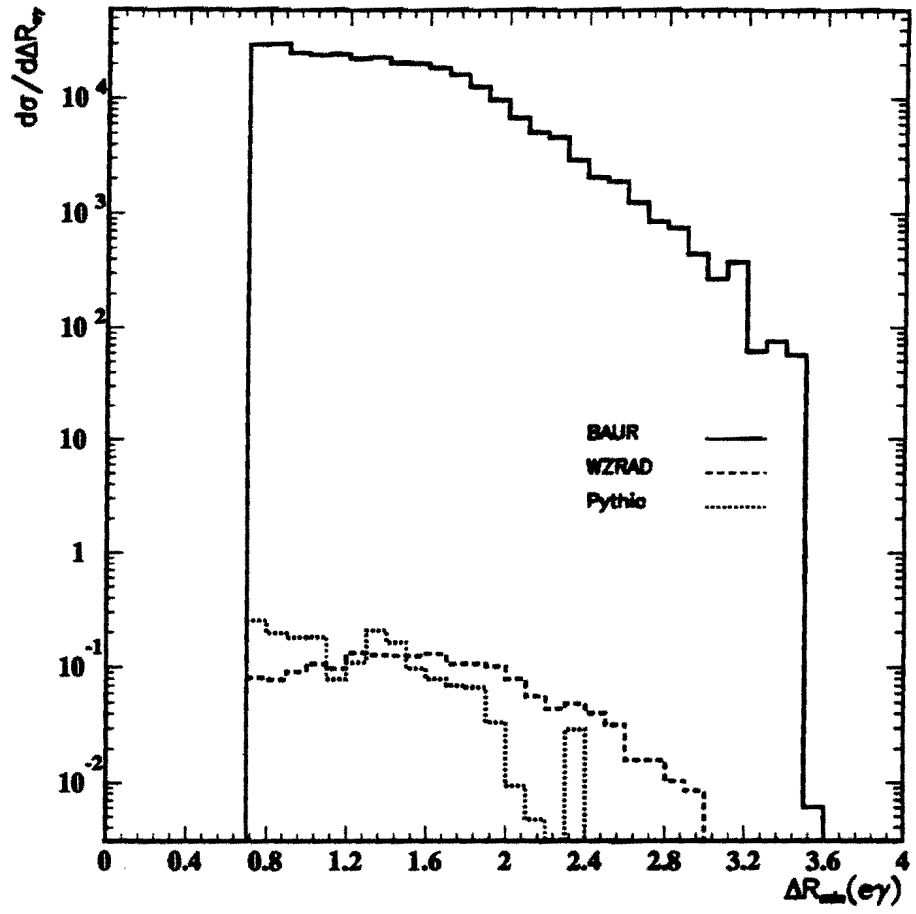

Figure 4.6: $\Delta R_{min}(e\gamma)$:Minimum Angle between electron and photon.

Chapter 5

Determination of Acceptances, Efficiencies and Backgrounds

5.1 Acceptance

The $Z\gamma$ cross section, the geometric & kinematic acceptances and the predicted number of CEM/PEM electron $Z\gamma$ events are all determined using an unweighted version of the Baur Monte Carlo[49, 50]. The cross-section experimentally is given by

$$\sigma_Z \cdot B(Z \rightarrow e^+e^-\gamma) = \frac{\mathcal{N}^{Z\gamma}_{observed} - \sum \mathcal{N}^{Z\gamma}_{background}}{A_{Z\gamma} \cdot \epsilon_{Z\gamma} \cdot \int \mathcal{L}dt}$$

where $\mathcal{N}^{Z\gamma}_{observed}$ is the number of observed $Z\gamma$ events in the electron decay channel; $\sum \mathcal{N}^{Z\gamma}_{background}$ is the number of background events expected in the data sample. The product terms $A_{Z\gamma} \cdot \epsilon_{Z\gamma}$ are the acceptance $\times$ efficiency factors for detecting the $Z\gamma$ events, respectively. The integrated luminosity ($\int \mathcal{L}dt$) in the denominator normalizes the number of events to the data sample.

Since the P_t spectrum of the photon is steeply falling, it is not possible to measure the total cross section $\times$ branching ratio for the $Z\gamma$ process. Both the photon, P_t and the angular separation, $\Delta R_{e\gamma}$, of the photon and lepton are kinematical parameters which are subjet to event selection cuts. Therefore only part of the $\sigma \times BR(Z\gamma)$ above a particular P_t cut for the photon energy is able to be determined. Furthermore, the additional cut on the angular separation between the photon and the lepton is done to suppress the final-state radiative or inner bremsstrahlung contributions.

Thus, the cross-section output from the Baur MC event generator is used to determine the Zγ production cross-section $\times$ decay branching ratio for all events passing the photon cuts, by using the following:

$$N^{Z+\gamma}_{MC signal} = \sigma \cdot B(Z+\gamma)_{cuts} \cdot \int \mathcal{L}dt \cdot (A_{Z\gamma} \cdot \epsilon_{Z\gamma})$$

and

$$N^{Z+\gamma}_{MC signal} = \sigma \cdot B(Z+\gamma)_{gen} \cdot \int \mathcal{L}dt \cdot (A'_{Z\gamma} \cdot \epsilon_{Z\gamma})$$

where $A'_{Z\gamma}$ is the overall kinematic and geometrical acceptance factor for the generated Zγ events which pass the $E_t^\gamma > 5.0$ GeV and $\Delta R_{e\gamma} > 0.7$ photon cuts. By equating the two equations we obtain:

$$\sigma \cdot B(Z+\gamma)_{cuts} = \sigma \cdot B(Z+\gamma)_{gen} \cdot [\frac{A'_{Z\gamma} \cdot \epsilon_{Z\gamma}}{A_{Z\gamma} \cdot \epsilon_{Z\gamma}}].$$

The product acceptance $\times$ efficiency terms are actually products of all the separate acceptances $\times$ efficiencies:

$$A_{Z\gamma} \cdot \epsilon_{Z\gamma} = A_Z \cdot A^\gamma_{\text{geom}} \cdot \epsilon_{\text{lepton}} \cdot \epsilon_{\text{photon}} \cdot \epsilon_{\text{trigger}} \cdot \epsilon_{\text{Analysis cuts}}.$$

The acceptance A_Z is the combined electron fiducial & electron kinematic acceptance for the Z boson($A_{oo} = CEM, A_{ox} = PEM, A_{oy} = FEM$); the acceptance A^γ_{geom} is the combined geometric and kinematic acceptance of the photon to pass through a particular calorimeter. The ϵ terms are product efficiencies for detecting a lepton or a photon once they have passed through their respective detectors. The term ϵ_{lepton} is the efficiency for the CEM system to record the electron in the event, whereas ϵ_{photon} is the efficiency for the calorimeters to record the passage of the photon. The term $\epsilon_{\text{trigger}}$ is the lepton trigger efficiency. The term $\epsilon_{\text{analysis cuts}}$ is itself a product of efficiencies of the cuts used to make the data sample, e.g. electron isolation.

Appendix B contains a complete description of all acceptance and efficiency variables determined for electron Zγ events, while Table 5.1 contains the Z and photon acceptances in the electron channel for $Z\gamma$ as determined from the fast Monte Carlo detector simulation.

Table 5.1: Z & Photon Acceptances for $Z\gamma$

Z Acceptance	
A_Z	$28.6 \pm 0.1\%$
A_{oo}	$12.8 \pm 0.1\%$
A_{ox}	$13.2 \pm 0.1\%$
A_{oy}	$2.6 \pm 0.1\%$

Photon Fractions & Acceptances			
$\sigma \cdot B(Z\gamma)_{cuts}$		$\sigma \cdot B(Z\gamma)_{gen}$	
f^{γ}_{coo}	$69.6 \pm 0.4\%$	f'^{γ}_{coo}	$70.8 \pm 0.2\%$
f^{γ}_{cox}	$55.5 \pm 0.5\%$	f'^{γ}_{cox}	$50.8 \pm 0.2\%$
f^{γ}_{coy}	$33.7 \pm 1.1\%$	f'^{γ}_{coy}	$39.5 \pm 0.2\%$
A^{γ}_{coo}	$77.2 \pm 0.3\%$	A'^{γ}_{coo}	$18.9 \pm 0.2\%$
A^{γ}_{cox}	$74.4 \pm 0.4\%$	A'^{γ}_{cox}	$20.3 \pm 0.2\%$
A^{γ}_{coy}	$69.8 \pm 1.4\%$	A'^{γ}_{coy}	$14.7 \pm 0.6\%$

5.2 Efficiencies

The electron W & Z samples which come from the central electron sample have common efficiencies and backgrounds. The $Z\gamma$ analysis incorporates these efficiencies directly and uses them in conjunction with the determined photon efficiencies(as will be discussed in the photon efficiency section of this thesis).

5.2.1 Electron Efficiency

The efficiencies of the electron quality cuts for the Z° data sample, as mentioned above, are obtained for each individual cut in succession. A particular quality requirement for the sample will have all previous cuts made except for the one being determined. Data samples which are selected in this fashion contain good electrons

with little background and are unbiased to the particular quality parameter in question. The efficiency for a quality cut can be defined as:

$$\epsilon \equiv \frac{N_{pass}}{N_{unbiased}}$$

where N_{pass} is the number of electrons satisfying all quality requirements and $N_{unbiased}$ is the number of electrons in the unbiased data sample.

The isolation efficiency for electrons is required for both electrons of the Z^0 and is determined in a separate calculation. A Monte Carlo(MC) event generator, ISAJET, is used in combination with a simple detector simulation program to determine the acceptance of the CDF detector cuts as well as the analysis cuts. The electron quality cuts and the isolation cuts are simulated by simply accepting or rejecting events based on the measured efficiency of the cuts. This technique is much faster than a full simulation of each detector component. The total electron efficiency is then obtained from the product of the separately determined isolation efficiency and the measured efficiency of the electron quality cuts. The individual efficiencies are listed in Table 5.2, while in Table 5.3 the overall electron efficiencies are summarized.

5.2.2 Photon Efficiency

The overall photon efficiencies were obtained from the product of the efficiencies for each of the CEM photon cuts as described in section 4.2.5. As was done in the W/Z analysis, isolation efficiency is determined in a separate calculation. Two methods were employed to determine the central calorimeter photon isolation efficiency.

1. Random Cones in the inclusive Z data sample were used to obtain the calorimeter isolation efficiency in the central calorimeter, $|\eta| < 1.1$, for cut ET4 $<$ 2.0 Gev (ET4 $\equiv$ the amount of extra transverse energy deposited in a cone of $\Delta R = 0.4$, but not including the EM cluster energy), where a cone of

Table 5.2: Individual Electron Efficiencies for $Z\gamma$

$\mathcal{L}_e \cdot dt$	$4.05 \pm 0.28\ pb^{-1}$	Integrated Luminosity
F_{DY}	$98.5 \pm 0.5\%$	$70 < M_Z < 110$ Gev/c^2
ϵ_{zvx}	$95.4 \pm 0.1\%$	$\mid Z_{vtx} \mid < 60\ cm$
ϵ^{cem}_{iso}	$96.0 \pm 1.0\%$	Isolation I ($R = 0.4$) Cut
$\epsilon^{cem}_{Had/EM_T}$	$99.0 \pm 1.0\%$	*Tight* Had/EM Cut
$\epsilon^{cem}_{Had/EM_L}$	$99.0 \pm 1.0\%$	*Loose* Had/EM Cut
$\epsilon^{cem}_{\chi^2_{strip}}$	$97.0 \pm 1.0\%$	$\chi^2_{strip} < 15.0$ Cut
$\epsilon^{cem}_{L_{shr}}$	$97.0 \pm 1.0\%$	$L_{shr} < 0.2$ Cut
ϵ^{cem}_{E/P_T}	$93.0 \pm 1.0\%$	Tight E/P < 1.5 Cut
ϵ^{cem}_{E/P_L}	$97.0 \pm 1.0\%$	Loose E/P < 2.0 Cut
ϵ^{cem}_{trk}	$100.0^{+0.0}_{-0.1}\%$	CTC Track Reconstruction
$\epsilon^{cem}_{\Delta x}$	$97.0 \pm 1.0\%$	$\Delta x < 1.5\ cm$ Matching Cut
$\epsilon^{cem}_{\Delta z}$	$98.0 \pm 1.0\%$	$\Delta z < 3.0\ cm$ Matching Cut
ϵ^{pem}_{iso}	$96.0 \pm 1.0\%$	Isolation I ($R = 0.4$)
$\epsilon^{pem}_{Had/EM}$	$99.0 \pm 1.0\%$	Had/EM Cut
$\epsilon^{pem}_{\chi^2_{3\times3}}$	$94.0 \pm 1.0\%$	$\chi^2_{3\times3} < 20.0$ Cut
ϵ^{pem}_{vtpc}	$93.0 \pm 2.0\%$	VTPC Hit Fraction > 0.5 Cut
ϵ^{fem}_{iso}	$91.0 \pm 1.0\%$	Isolation I ($R = 0.4$) Cut
$\epsilon^{fem}_{Had/EM}$	$100.0^{+0.0}_{-0.1}\%$	Had/EM Cut
ϵ_{L1}	$99.3 \pm 0.3\%$	Level-1 Central Electron Trigger
ϵ_{L2}	$98.0 \pm 0.4\%$	Level-2 Central Electron Trigger
ϵ_{L3}	$100.0^{+0.0}_{-0.1}\%$	Level-3 Central Electron Trigger

Table 5.3: Overall Electron Efficiencies for $Z\gamma$

T	97.3 ± 0.5%	Central Fiducial Electron Trigger
ϵ_{cent_T}	84.0 ± 3.0%	*Tight* Central Fiducial Electron
ϵ_{cent_L}	93.0 ± 3.0%	*Loose* Central Fiducial Electron
ϵ_{plug}	90.0 ± 3.0%	Plug Fiducial Electron
ϵ_{fwrd}	91.0 ± 3.0%	Forward Fiducial Electron

$\Delta R = \sqrt{\Delta\eta^2 + \Delta\phi^2} = 0.4$ was required to be more than $\Delta R = 0.7$ away from the decay leptons.

2. Minumum Bias and Jet-20 data samples were also used to determine the efficiency of the ET4 calorimeter isolation cut. For the Jet-20 data, random cones of $\Delta R = 0.4$ were thrown for events which satisfy the following:

   - $|Z_{vertex}| < 60.0$ cm
   - $\not\!\!E_t < 20.0$ GeV, $\not\!\!E_t$ significance, $\sigma_{\not\!\!E_t} < 2.4$. These cuts were imposed to suppress badly mis-measured and/or junk events in the Jet-20 sample.
   - At least three jets in a Jet-20 event
   - QDJSCO-corrected[51] jets
   - For the two leading or highest E_t jets (after QDJSCO corrections have been applied), require that at least one of the two be in the central($|\eta|_{det} <$ 1.1) region of the detector and the other in the central or plug($|\eta|det <$ 2.4)
   - For the two leading jets, require that each QDJSCO-corrected jet have $E_t > 15.0$ GeV and that $M_{JJ} > 40.0$ GeV/c^2

For the Jet-20 data of method 2, two separate studies were done. The first(Jet-20a) study required that the random cones of $\Delta R = 0.4$ be more than $\Delta R = 1.4$ away from *all* jets in the event, so as not to overlap with the default $\Delta R = 0.7$

jet-cone clustering radius of the JETCLU algorithm. The second study(Jet-20b) required the random cones be away from the two leading (i.e. trigger) jets in the event.

The QFL Baur MC for $Z\gamma$ was used as a check for the above two methods. The underlying event was simulated using ISAJET as discussed in section 4.2.2 and as was done in the inclusive Z sample the $\Delta R = 0.4$ cone was required to be more than $\Delta R = 0.7$ away from the decay leptons.

Individual efficiencies are obtained for each of the data sets or methods used in determining the calorimeter isolation efficiency. For the $\sum PT4$ cut, the efficiency is determined downstream of the ET4 cut and similarly the efficiency for the No 3D track cut is made downstream of the $\sum$PT4 cut. The efficiencies for the Had/EM, Lshare, χ^2_{wire}, χ^2_{strip}, & No 2nd CES cluster cuts are all obtained using 5, 10 and 50 GeV CEM testbeam electron data and from the QFL Baur MC $Z\gamma$ simulated data. Figures 5.1 and 5.2 show the analogous plots for the Jet-20 data as Figures 4.1 and 4.2 did in the electron selection section.

All the CEM photon efficiencies for individual cuts are listed in Tables 5.4. The photon efficiencies using random cones in the Minimum Bias data sample are systematically higher than those from the inclusive Z data sample, similarly the Jet-20a data sample is higher by about 5%. The Jet-20b data sample, however is lower by $\approx$ 5% than the Z data sample. The QFL Baur MC $Z\gamma$ data samples efficiency of the ET4-$\sum$PT4 cut is systematically higher than the Z data sample due to ISAJET producing a "less-noisy" underlying event.

The overall CEM photon efficiencies for individual and combined cuts are summarized in Table 5.5 and include both statistical and systematic uncertainties. This also includes the photon survival probability factor, P^{γ}_{conv} and the EM shower development difference factor, $S^{cem}_{e\to\gamma}$, between electrons and photons. Both of these contributions are discussed in Appendix B.

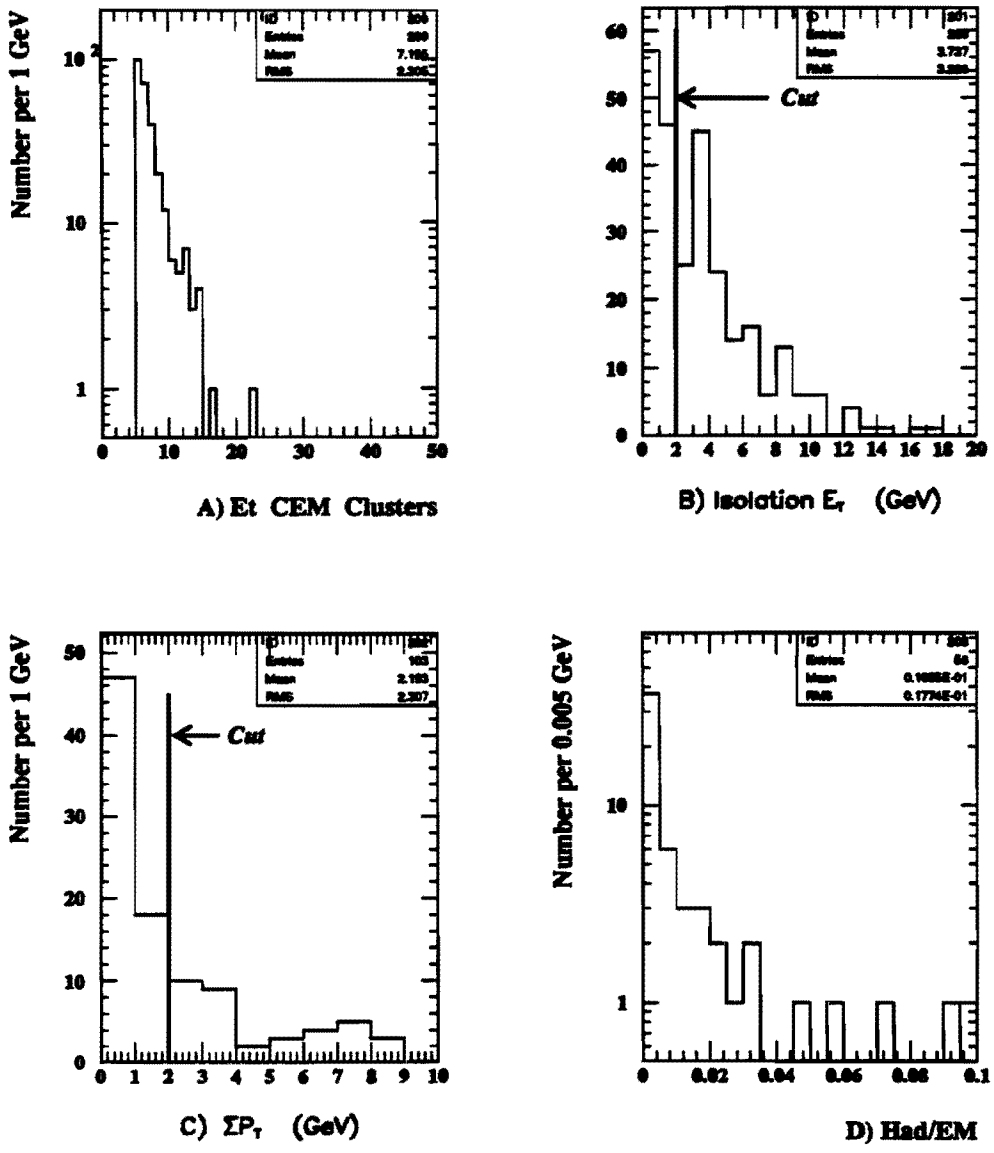

Figure 5.1: Jet-20 Photon variables, E_t^{CEM}, Isolation E_t, $\sum P_t$ and Had/EM as a function of photon cuts.

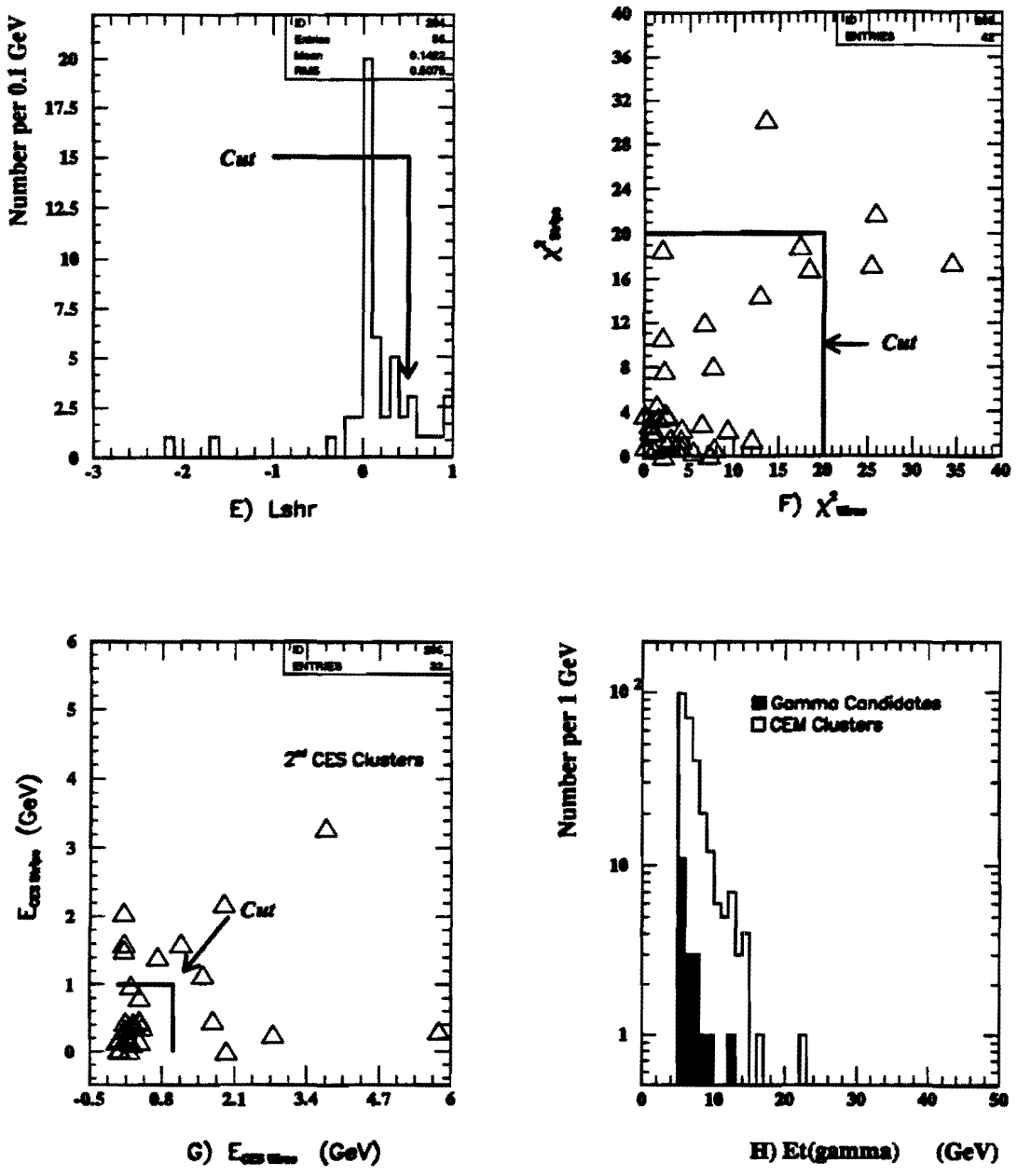

Figure 5.2: Same as 5.1 for the variables, Lshr, χ^2_{strip} vs χ^2_{wire} and E_{strip} vs E_{wire} and Photon E_t.

Table 5.4 : $Z\gamma$ Individual Efficiencies for Monte Carlo, Random Cone and Testbeam Data.

Individual Efficiency ϵ	QFL MC $Z\gamma$	Random Cones			
		Z_e	MinBias	Jet-20a	Jet-20b
$ET4 < 2.0$	$97.9 \pm 1.2\%$	$95.8 \pm 0.6\%$	$98.6 \pm 0.2\%$	$99.1 \pm 0.1\%$	$92.7 \pm 0.2\%$
$ET4 < 2.0 \sum PT4 < 2.0$	$97.0 \pm 1.3\%$	$93.6 \pm 0.7\%$	$97.7 \pm 0.2\%$	$97.6 \pm 0.1\%$	$89.3 \pm 0.3\%$
$ET4 < 2.0 \sum PT4 < 2.0 N3D = 0$	$91.9 \pm 2.0\%$	$89.1 \pm 0.9\%$	$92.8 \pm 0.2\%$	$92.7 \pm 0.2\%$	$84.2 \pm 0.3\%$

Individual Efficiency ϵ	QFL MC $Z\gamma$	Electron Test Beam				
		5 GeV	10 GeV	18 GeV	30 GeV	50 GeV
$Had/EM < ABW$	$99.2 \pm 0.8\%$	$98.9 \pm 0.2\%$	$99.6 \pm 0.1\%$	$99.1 \pm 0.9\%$	$98.9 \pm 0.9\%$	$98.0 \pm 0.3\%$
$L_{shr} < 0.5$	$100.00^{+0.0}_{-0.5}\%$	$99.9 \pm 0.1\%$	$98.8 \pm 0.4\%$	$100.0^{+0.0}_{-1.7}\%$	$100.0^{+0.0}_{-1.1}\%$	$99.9 \pm 0.1\%$
$\chi^2_{stp}, \chi^2_{wir} < 20$	$95.4 \pm 1.6\%$	$97.3 \pm 0.3\%$	$96.2 \pm 0.4\%$	$98.2 \pm 1.8\%$	$99.2 \pm 0.7\%$	$99.2 \pm 0.2\%$
$No\ 2^{nd} CES > 1GeV$	$95.0 \pm 2.4\%$	$98.0 \pm 0.1\%$	$97.9 \pm 0.1\%$	$98.2 \pm 1.6\%$	$98.2 \pm 1.0\%$	$97.6 \pm 0.2\%$

Table 5.5: Overall CEM Photon Efficiency Determination.

ϵ^{γ}_{ET4}	$95.7 \pm 0.3 \pm 0.5\%$	Calorimeter Isolation Cut
$\epsilon^{\gamma}_{\sum PT4}$	$97.4 \pm 0.4 \pm 0.8\%$	Tracking Isolation Cut
ϵ^{γ}_{N3D}	$95.3 \pm 0.5 \pm 0.7\%$	No track at EM Cluster Cut
$\epsilon^{\gamma}_{Had/EM}$	$99.2 \pm 0.1 \pm 0.8\%$	Had/EM Cut
ϵ^{γ}_{Lshr}	$99.9 \pm 0.1 \pm 0.3\%$	Lateral Shower Cut
$\epsilon^{\gamma}_{chi^2_{stp}+chi^2_{wir}}$	$98.4 \pm 0.1 \pm 0.9\%$	CES strip/wire chi^2 Cut
$\epsilon^{\gamma}_{no\ 2^{nd}\ CES}$	$97.9 \pm 0.7 \pm 1.0\%$	No 2^{nd} CES Clusters
P^{γ}_{conv}	$96.5 \pm 0.2 \pm 1.0\%$	Photon Survival
$S^{cem}_{e\rightarrow\gamma}$	$100.4 \pm 0.6 \pm 1.0\%$	e *vs.* γ Shower Development
ϵ^{γ}_{cem}	$82.0 \pm 1.5 \pm 2.1\%$	Overall Photon Efficiency

Data Sample	$\epsilon^{\gamma}_{Had/EM}$	ϵ^{γ}_{Lshr}	$\epsilon^{\gamma}_{chi^2_{stp}+chi^2_{wir}}$	$\epsilon_{no\ 2^{nd}\ CES}$
QFL γ MC 5 - 15 GeV	$99.7 \pm 0.1\%$	$99.8 \pm 0.1\%$	$97.4 \pm 0.3\%$	$96.8 \pm 0.3\%$
QFL e MC 5 - 15 GeV	$99.9 \pm 0.1\%$	$99.9 \pm 0.1\%$	$97.9 \pm 0.2\%$	$95.8 \pm 0.3\%$

5.3 Backgrounds

The backgrounds for $Z\gamma$ are mainly due to QCD jet-faking photons and prompt isolated photons from quark and QED bremsstrahlung. These initial/final-state radiative processes are considered part of the $Z\gamma$ signal and are explicitly accounted for in the Baur MC by the use of the k-factor ≈ 1.35. The generated events will therefore approximate contributions from higher order QCD processes as was previously mentioned in section 4.3.2.

The QCD jet-faking photon background is determined using Jet-20 data and VECBOS[52]/HERWIG[53] Z+njet MC data. HERWIG is used for both the underlying event and jet fragmentation.

The Jet-20 data selection criteria are the same as those used for the photon efficiency determination as stated in the last section. The physics motivation of using two leading jets is to obtain a sample that closely resembles an actual Z+jet data set. The dijets of the two leading jets are required to be near the Z mass with the extra requirement that there be an extra jet in the event.

In the Z sample, the product of the two leading central jets, which have been QDJSCO-corrected[51], is summed E_t -bin by E_t-bin in a given E_t -bin of width 2.5 Gev. Here $E_t^{Jet} > 5$ GeV and $\Delta R_{l-j} > 0.7$ away from the decay leptons. This number is then multiplied by the total number of ELES objects in the same E_t -bin of the Jet-20 sample, where again the $E_t^{Jet} > 5$ GeV, must pass all γcuts, & $\Delta R_{TJ-ELES} > 1.4$ away from the 2 leading trigger jets. This value must then be divided by the total number of QDJSCO-corrected extra central jets in the same E_t -bin of the Jet-20 data, where $E_t^{Jet} > 5$ GeV & $\Delta R_{TJ-XJ} > 1.4$ away from the 2 leading trigger jets. More clearly stated, the number of QCD jet-faking photon background events in the Z data sample for a corrected $E_t > 5$ GeV is the following:

$$N_{bknd}^{Jet\ Ze} = \sum_{i}^{JetZe} N_i^{Jet\ Ze}(|\eta_j| < 1.1, \Delta R_{l-j} > 0.7) * \frac{N_i^{FidCEMJ20}(\Delta R_{TJ-ELES} > 1.4)}{N_i^{ExtraCEMJ20}(\Delta R_{TJ-XJ} > 1.4)}$$

The number passing the trigger-jet selection for the Jet-20 data is 11726 events,

where 431 central ELES objects had $E_t > 5$ GeV and were $\Delta R > 1.4$ away from a jet. Implementing the fiducial CEM cut leaves a total of 269 events. Of these, a total of 20 events survive the $ET4 < 2.0$ GeV and $\sum PT4 < 2.0$ GeV photon cuts. For the inclusive Z data sample with central jets there are 175 jets for the electron channel.

The predictions for the number of QCD jet-faking CEM photons in the central electron $Z\gamma$ data sample were also determined from the normalized, luminosity weighted VECBOS/HERWIG Z + 0,1,2 jet QFL MC data which were required to pass the same inclusive central Z cuts and CEM γ cuts. The predicted number of CEM QCD jet-faking photon background events obtained using the above two processes are summarized in Table 5.6. The uncertainties are statistical only, except for the combined prediction, where the systematic error is on the Jet-20 determination of the QCD jet-faking photon background. The systematic uncertainty is defined to be the difference between the QCD background as found from the Jet-20 data minus the QCD background from the VECBOS/HERWIG/QFL Z+n-jets MC simulation.

Table 5.6: QCD γ Background Estimates for $Z\gamma$

CEM γ Cut $ET4 < 2.0 \sum PT4 < 2.0$	N^Z_{QCD}
Inclusive $Z + Jets$ Data	0.30 ± 0.07
Jet-20 ($\Delta R_{JJ} > 1.4$)†	0.30 ± 0.07
VECBOS $Z + nJets$ MC	0.20 ± 0.09
Overall CEM γ Cut	$0.30 \pm 0.07 \pm 0.14$

† For these data we used both a Standard and Summed Method of Analysis. Each method determined the background using uncorrected and corrected jet energies. Of the four possibilities, only the Standard Uncorrected Method had a different result, 0.28 ± 0.07.

Plots of the transverse energy in both the Jet-20 background for $Z\gamma$ with the $ET4 < 2.0$ GeV and $\sum PT4 < 2.0$ GeV photon cuts as well as the jet E_t spectrum

for the data sample, can be seen in Figure 5.3. Also in Figure 5.4 the fake γ rates are shown.

Other backgrounds to the Zγ process include $(Z \rightarrow \tau\tau)+\gamma$ and $(Z \rightarrow \tau\tau)+Jet$. Since the original Baur MC did not include tau decay as one of the possible Z decay modes, tau lepton decay subroutines were written[12, 41], $\tau \rightarrow \nu_\tau l \bar{\nu}_\tau$ and where the proper tau decay polarization effects have been included. The tau decay contribution in the electron channel is found to be very small compared with the QCD background($<<$ 1 *event*) and is therefore neglected.

The QCD background obtained by the VECBOS/HERWIG/QFL Z+njets MC is systematically lower than the Jet-20 data. Various attempts were made to understand this discrepancy,

- The original version of HERWIG(V5.3) used did not include photon bremsstrahlung off the incoming quark lines. The latest version of HERWIG(V5.6) includes initial quark bremsstrahlung, however there is no observable increase in the final number of background events. Possible reasons for not detecting an increase may come from the following:
  - The code implemented in VECBOS is better at generating small angle or collinear bremsstrahlung than wide angle where $\Delta R_{q-\gamma} > 0.7$ away from a jet.
  - The number of background Zγ events with a photon from wide angle final state quark bremsstrahlung, where the quark jets fragment into photons which pass all cuts and that are scaled with the radiative WZRAD and J/Ψ Monte Carlo event generators, show that the contribution is small for the Z+jet process.
- The minimum E_t jet cutoff, at parton level, for the VECBOS/HERWIG/ QFL Z+njet MC simulation was investigated. The results show that the QCD background predictions are insensitive to this cutoff parameter, where the lowest

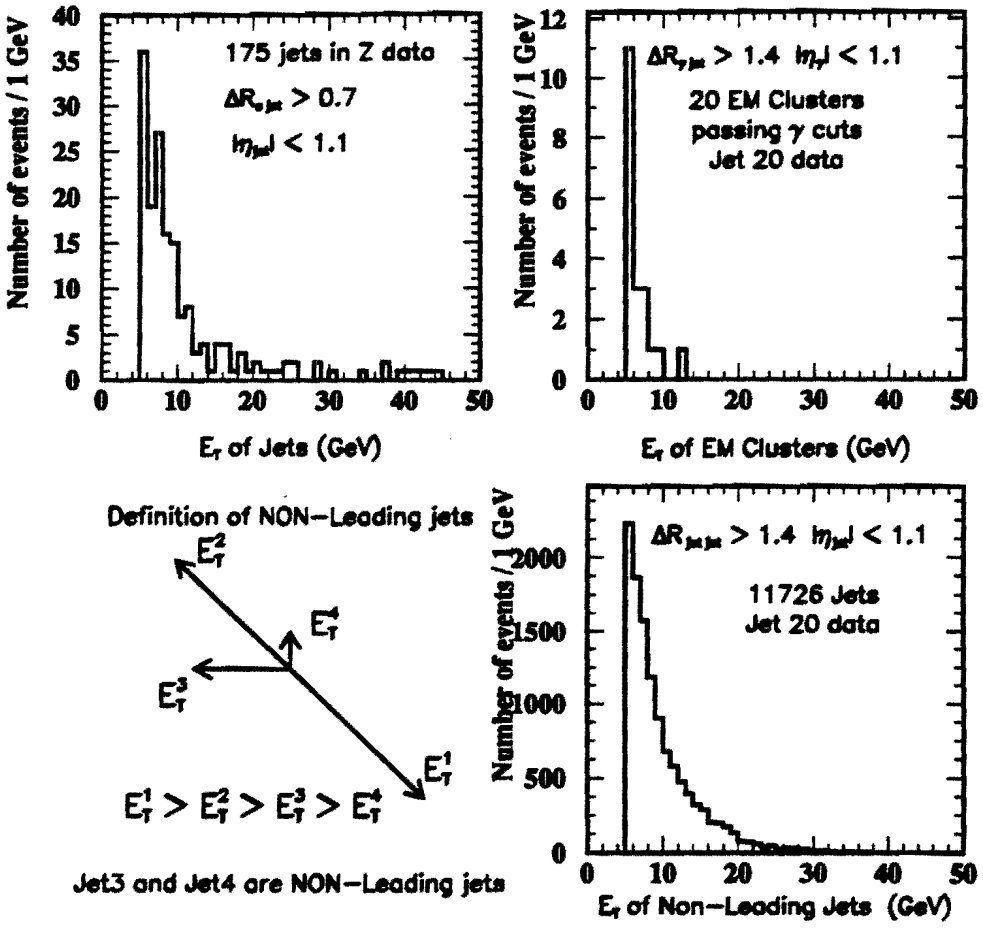

Figure 5.3: Jet-20 QCD background determination and the Inclusive Z data set Jet E_t spectrum.

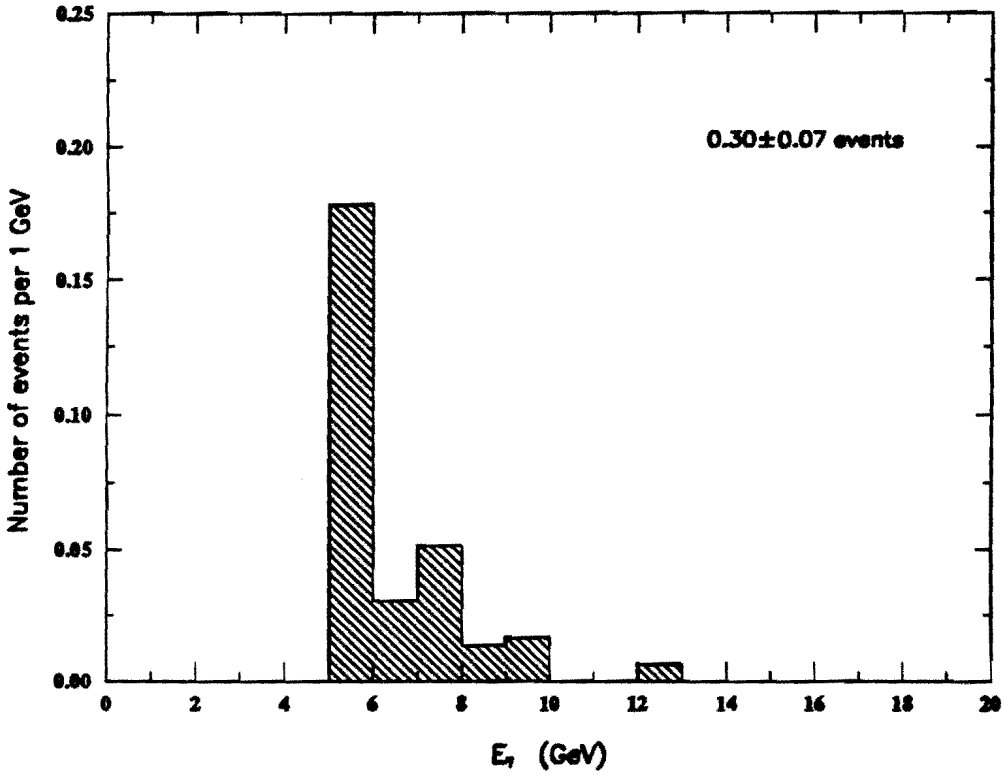

Figure 5.4: Transverse energy of jet-faking photon background.

threshold of $E_T^j > 8$ GeV was used as recommended by one of the authors of VECBOS, Walter Giele.

- For the range of jet fragmentation giving QCD jet-faking photons which pass all cuts, the possibility of the jet energy scale of VECBOS being mis-calibrated was investigated. By increasing the observed E_t spectrum by a factor between 15-25%, the Z+njet MC simulation was found to be in good agreement with the Jet-20 data.

- The CEM energy scale calibration at $E_t^\gamma \approx 5$ GeV, based on studies done by CDF[54] using low-energy electrons, was found to be correct at this energy to within $\approx 1\%$. Thus the impact on $Z\gamma$ events expected or predicted is negligible at this level of uncertainty.

Since both the Jet-20 and VECBOS data samples have very low statistics, not one of the factors listed above can be pinpointed as the major source of discrepancy. Therefore a conservative estimate of the systematic uncertainty comes directly from the Jet-20 background minus that from the VECBOS/HERWIG/QFL Z+njets MC as stated previously.

Chapter 6

The $Z\gamma$ Event Sample, $\sigma * BR(Z+\gamma)$ Results and Systematic Uncertainties

There are two $Z\gamma$ candidate events in the electron channel from the CDF '88-'89 collider run. Table 6.1 summarizes some of the kinematical properties of each of the candidates, while Figure 6.1 shows these results graphically with the MC expectations overlaid(the two events have been normalized to the number of predicted MC events).

Table 6.1: Kinematic Properties of $Z\gamma$ Candidates.

	Run # Event #	E_t^γ (GeV)	$\Delta R_{e\gamma}$	$M_{e^+e^-}$ (GeV)	$M_{Z\gamma}$ (GeV)
1	17025-5219	13.47	1.50	91.0	104.6
2	18170-14254	5.44	0.88	82.0	88.2

Figures 6.2, 6.3 and 6.4 contain distributions of the real $Z\gamma$ data for the CDF 1988-1989 run. Figure 6.2 is a lego plot distribution where the cylindrical detector has its azimuthal angle ϕ flattened into the pseudorapidity η plane. Figures 6.3 and 6.4 are distributions of a ϕ slice of the detector where the center is the interaction point(or where the Z° is at rest when it decays).

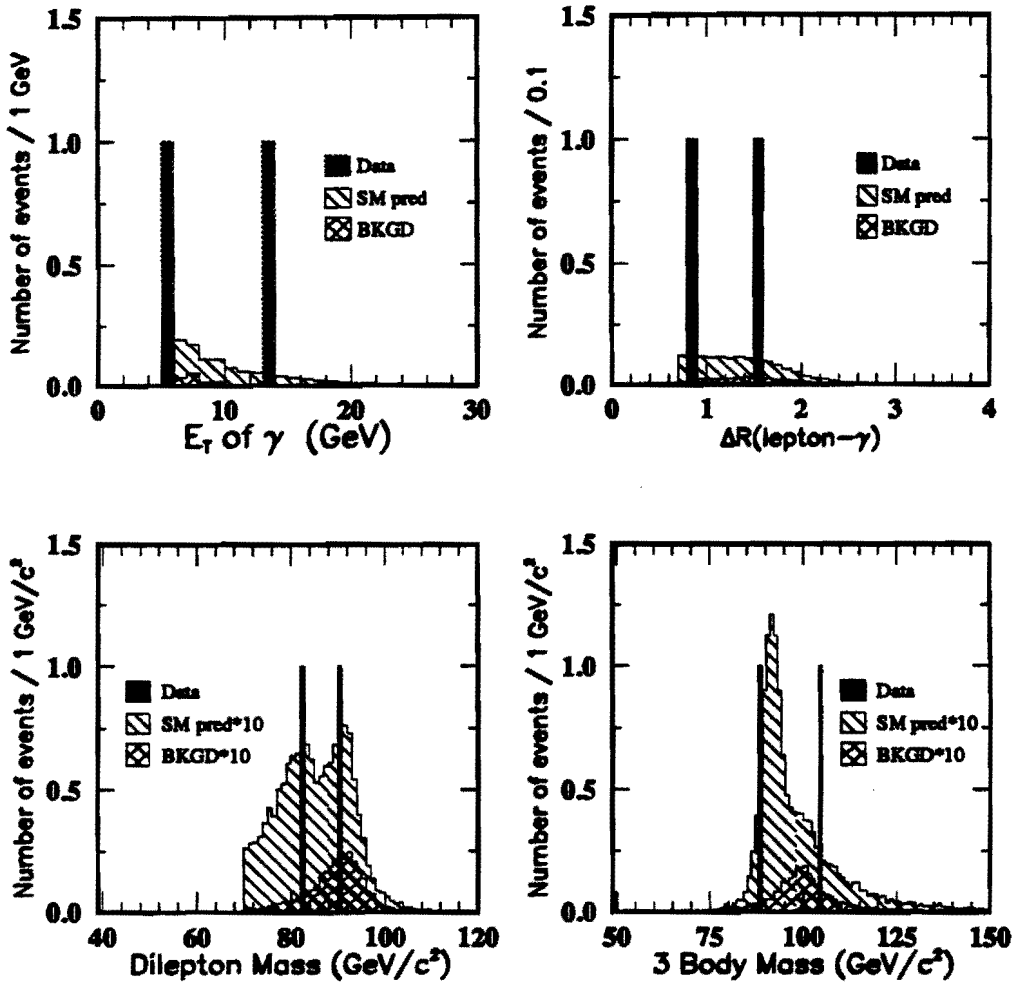

Figure 6.1: Kinematic properties of MC Signal, Background and Observed events for $Z\gamma$.

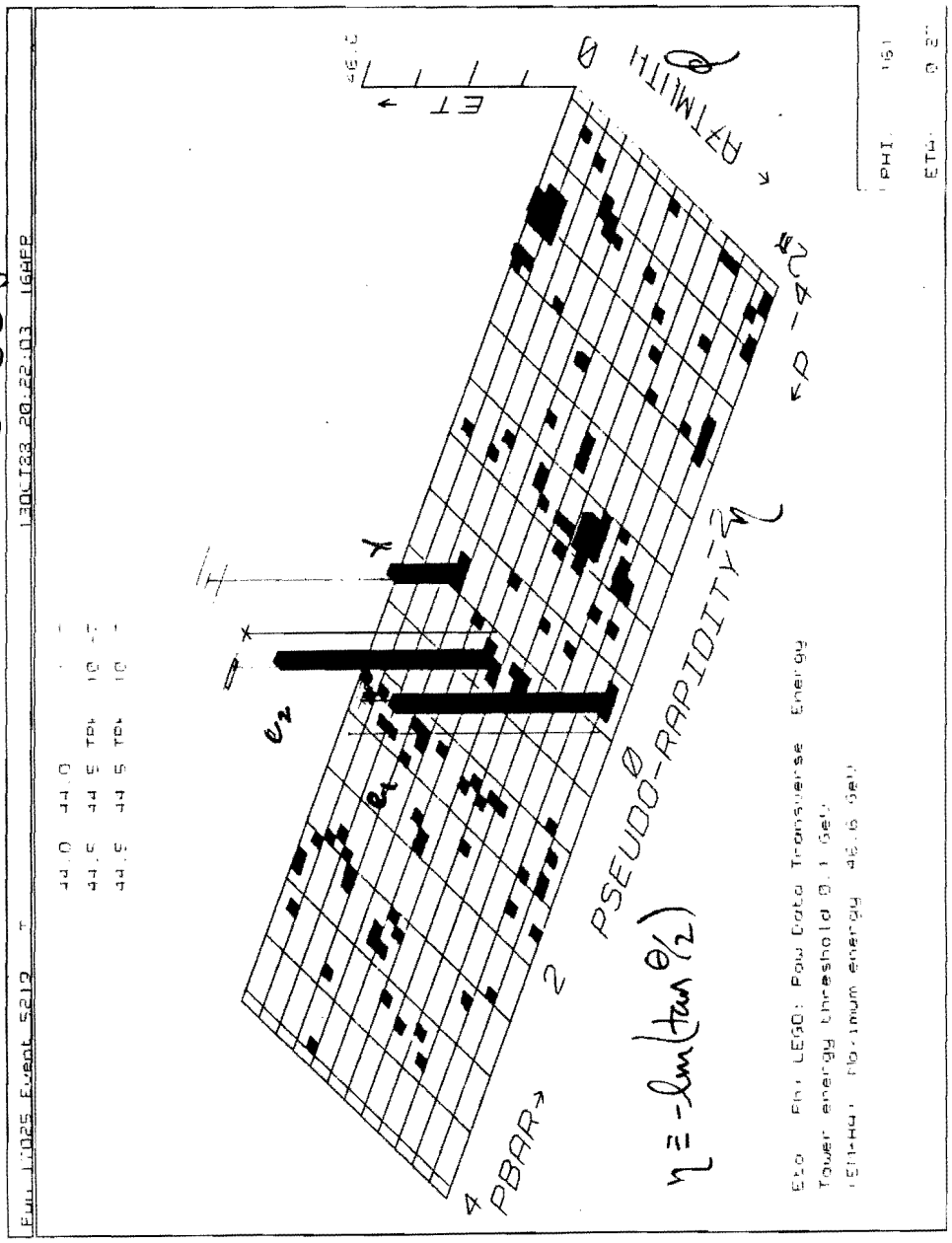

Figure 6.2: Lego Distribution Plot of Real $Z\gamma$ Data(Run 17025 Event 5219).

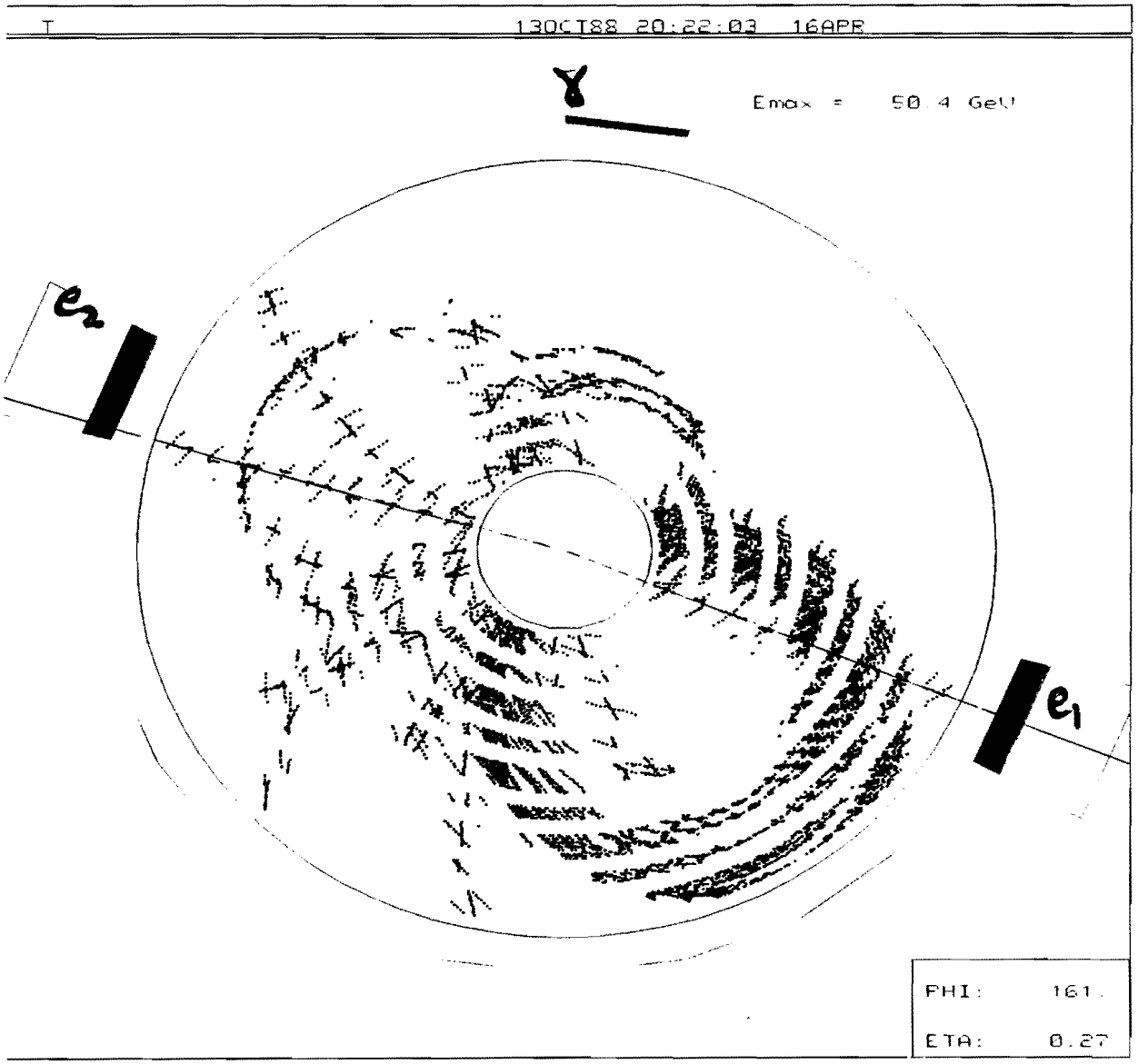

Figure 6.3: Azimuthal Slice Distribution of Real $Z\gamma$ Data(Run 17025 Event 5219).

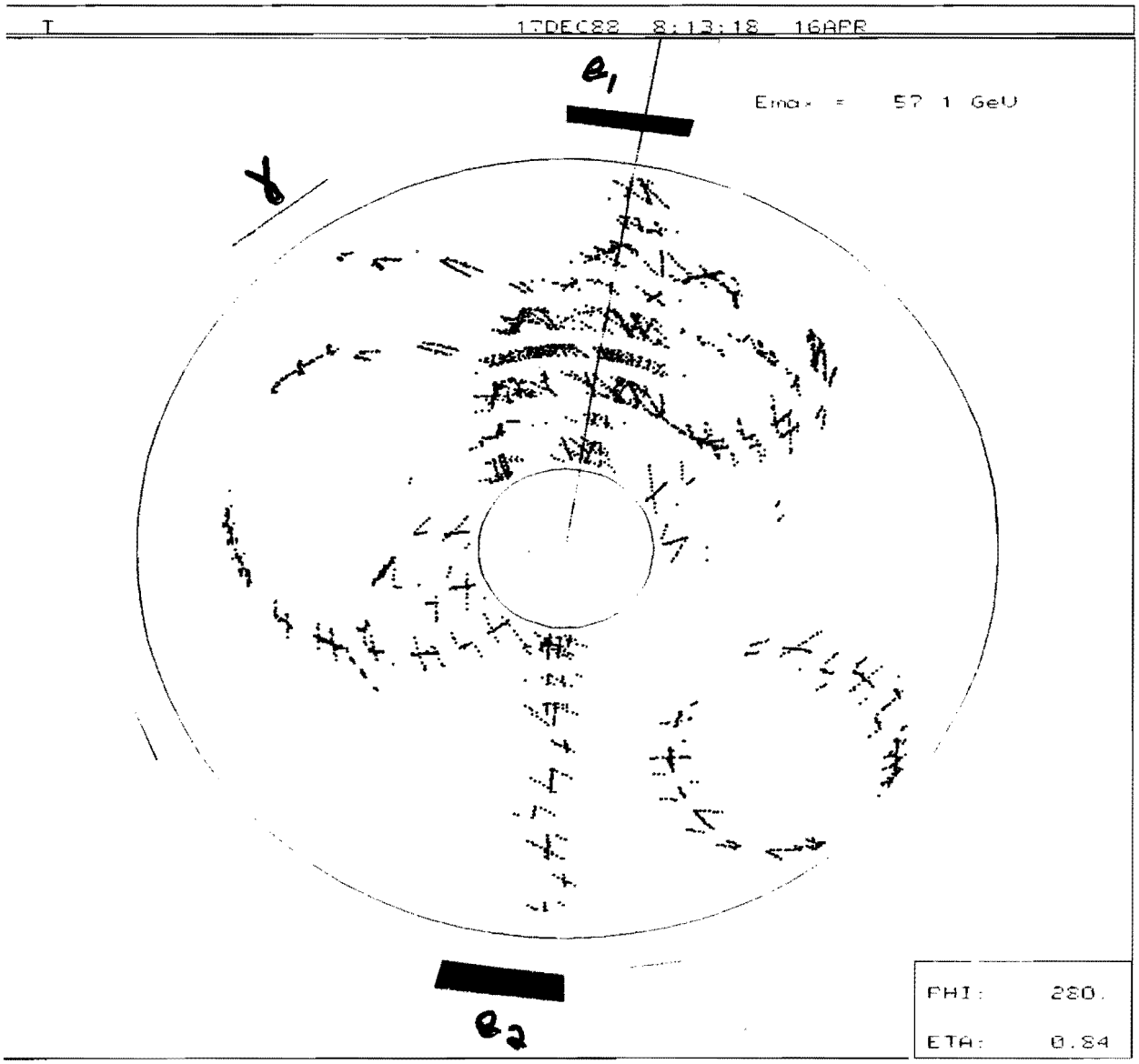

Figure 6.4: Azimuthal Slice Distribution of Real $Z\gamma$ Data(Run 18170 Event 14254).

6.1 Determination of $\sigma * BR(Z + \gamma)$

As discussed in Section 5.1, the results for the cross section × branching ratio for Zγ were determined using the relation

$$\sigma_Z \cdot B(Z \to \ell^+\ell^-\gamma) = \frac{N^{Z\gamma}_{observed} - \sum N^{Z\gamma}_{background}}{A_{Z\gamma} \cdot \epsilon_{Z\gamma} \cdot \int \mathcal{L}_\ell dt}$$

The number of observed candidates was input to a complete MC program which simulated 10^6 CDF experiments, where the number of observed events were Poisson-fluctuated, the integrated luminosity was Gaussian-fluctuated and using all $A \cdot \epsilon$ terms as given in Tables 5.1 and 5.2. The backgrounds were also gaussian-fluctuated and then subtracted from the observed number of events on an "experiment-by-experiment" basis. The experimental cross-section $\sigma \cdot BR$ was calculated from a cumulative histogram. Using the Particle Data Group(PDG) method of a bounded physical region[55], the 68.3%, 90.0% and 95.0% C.L. upper limits as well as the mean and $\pm 1\sigma$ (double-sided) uncertainties on the mean of $\sigma \cdot BR$ were obtained.

Table 6.2 lists the number of signal events found for Zγ , where the first uncertainty is statistical and the second is the systematic uncertainty associated with the QCD photon background determination.

Table 6.2: Zγ Signal Results.

N_{obs}	$\sum N_{bkgnd}$	N_{signal}	N^{SM}_{pred}
2	$0.3 \pm 0.1 \pm 0.1$	$1.7 \pm 1.4 \pm 0.1$	1.2 ± 0.1

Figure 6.5 shows the electron Zγ $\sigma \cdot BR$ probability distribution, where the Poisson nature of these results can be seen by the small statistics. The fractional number of QCD jet-faking photon background is on the order of 10%. These distributions are binned extremely fine so that the $\pm 1\sigma$ (68.3%) double-sided and 68.3%, 90.0% and 95.0% single-sided CL limits to $\sigma \cdot BR(Z\gamma)$ can be determined.

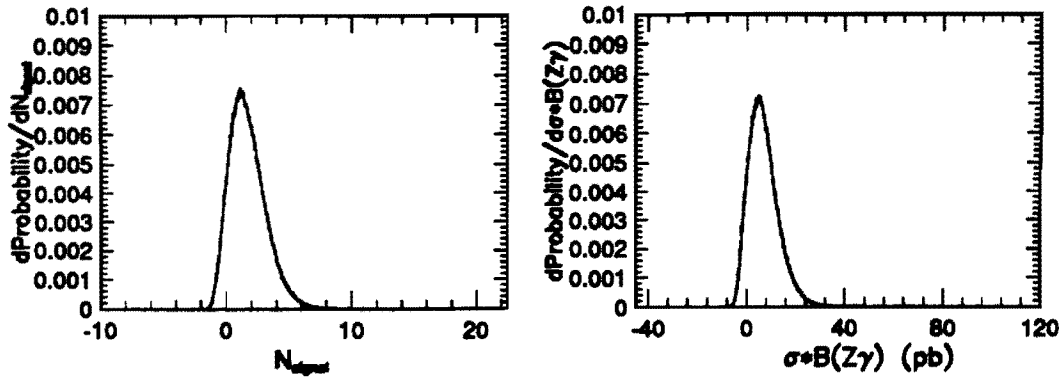

Figure 6.5: $N_{signal}^{Z+\gamma}$ and $\sigma * BR(Z+\gamma)$ probability distributions.

Table 6.3: $\sigma \cdot BR(Z\gamma)$ Results.

$Z\gamma$ Sample	$\sigma \cdot BR_{expt}(pb)$	$\sigma \cdot BR_{pred}^{SM}(pb)$
68.3% DS C.L.	$6.8^{+5.6}_{-5.6}\ ^{+0.5}_{-0.5}\ ^{+0.4}_{-0.4} = 6.8^{+5.7}_{-5.7}$	4.6 ± 0.1
68.3% SS C.L.	< 9.6	
90.0% SS C.L.	< 15.1	
95.0% SS C.L.	< 17.9	

The $Z\gamma$ cross-section results are summarized in Table 6.3, where the first uncertainty is statistical only, the second is the systematic uncertainty due to the integrated luminosity and the third is the systematic uncertainty based on the QCD photon background determination.

6.2 Systematic Uncertainties

By varying the $Z+\gamma$ P_t -distribution, the structure function(SF) choice and the Q^2 -scale for the nominal SF (HMRS-B) the systematic effects were studied. Since the diboson P_t spectrum has neither a detailed theoretical prediction or an experimental measurement, the $Z+\gamma$ P_t -distribution is approximated by the measured CDF Z P_t distribution [48], which for the photon P_t region we are sensitive to is reasonable. Using the same method as applied in the muon R analysis[56], the MC

diboson P_t distributions, for the nominal SF choice, were varied within the $\pm 1\sigma$ limits allowed by the fit to the $d\sigma/dP_T$ distribution. This method involves the use of a fast MC detector simulation program which obtains the MC $\sigma * BR(Z+\gamma)$ and all kinematical and geometrical acceptances, where the MC events are required to pass all event selection cuts and the efficiencies of each cut are included. These acceptance results for each P_t choice were input to the experimental determination of the $\sigma * BR(Z+\gamma)$. Four P_t distributions were investigated to obtain both MC and experimental results: (1) No P_t boost, (2) a "soft" P_t boost, (3) a nominal P_t boost and (4) a "hard" P_t boost. The "No" P_t boost was included for completeness sake but was not used to determine any of the systematic uncertainties.

Figure 6.6 shows the P_t distributions for the "soft", "nominal" and "hard" boosts of the Z P_t distribution, while Figure 6.7 shows the variation of the $Z\gamma$ cross-section as a function of P_t choice for both MC and experiment. The error bars come from the statistical uncertainty on the acceptance determination and that of the MC generated $\sigma * BR(Z+\gamma)$. The difference between MC and experiment, defined as $\Delta\sigma(Z+\gamma)_{MC-Expt} \equiv 0$ for the nominal P_t distribution, is also shown in Figure 6.7. All other differences shown have been calculated relative to the nominal P_t distribution. The systematic trends of the MC and experimental data can be seen separately in Figure 6.7.

The systematic uncertainties associated with the Q^2 -scale dependence, for the range between $M^2_{V+\gamma}/4 < Q^2 < 4M^2_{V+\gamma}$, were investigated using the nominal SF choice(HMRS-B). The results are shown in Figure 6.8 for the three cases, (1) $Q^2 = M^2_{V+\gamma}/4$, (2) $Q^2 = M^2_{V+\gamma}$ (nominal) and (3) $Q^2 = 4M^2_{V+\gamma}$. The Q^2 scale dependence and the shape of the diboson P_t distribution are treated independently, which tends to overestimate the sensitivity of these effects since these variables are correlated by four-momentum conservation in the $Z+\gamma$ production process.

Various structure function choices were used to determine their contributions to the systematic uncertainty. The MC $\sigma * BR_{gen}$ results for the *generated* cross section

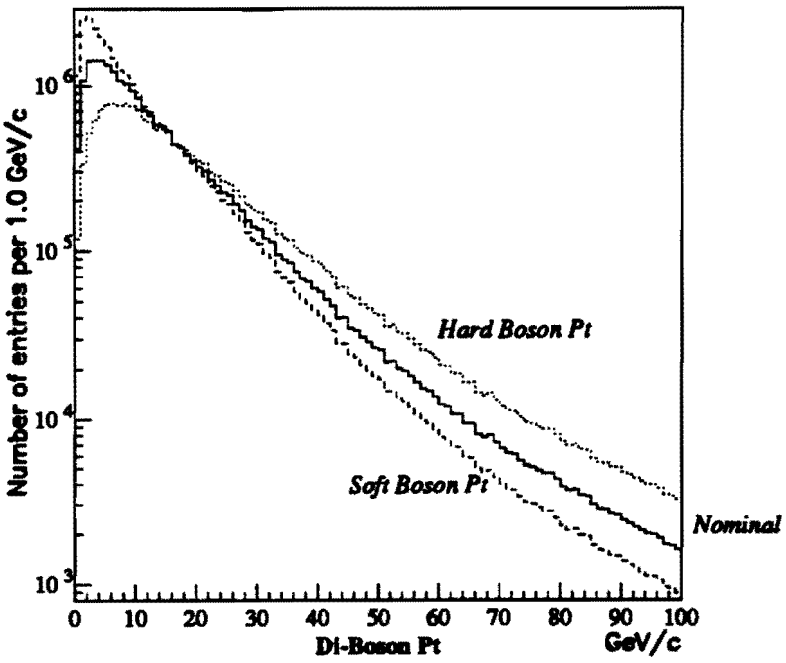

Figure 6.6: Di-Boson P_t Distribution(CDF 1504 parameterization).

output from the Baur Zγ MC for thirteen different SF choices is shown in Figure 6.10. Only the DFLM-260, MRS-B, HMRS-B, MRS-S0 and MT-B1 choices were analyzed using the fast MC detector simulation program. Here the MC $\sigma * BR_{cuts}$ was obtained as well as the kinematical and geometrical acceptances. Figure 6.9 shows the analogous plots as for the P_t and Q^2 studies discussed above.

There is a correlation found in the systematic uncertainties associated with varying the diboson P_t distributions, the Q^2 -scale dependence and the SF choices of the MC and experimental data. The MC and experimental $\sigma * BR(Z + \gamma)$ results must include the contributions of these three systematic uncertainties to obtain the overall uncertainty. However, since these uncertainties are all correlated the $\Delta\sigma(Z+\gamma)_{MC-Expt}$ *difference* must be used for determining the limits on the h_{30}^Z and h_{40}^Z parameters.

In Table 6.4 the $\pm 1\sigma$ individual systematic uncertainties $\Delta\sigma_{MC}$, $\Delta\sigma_{Expt}$ and

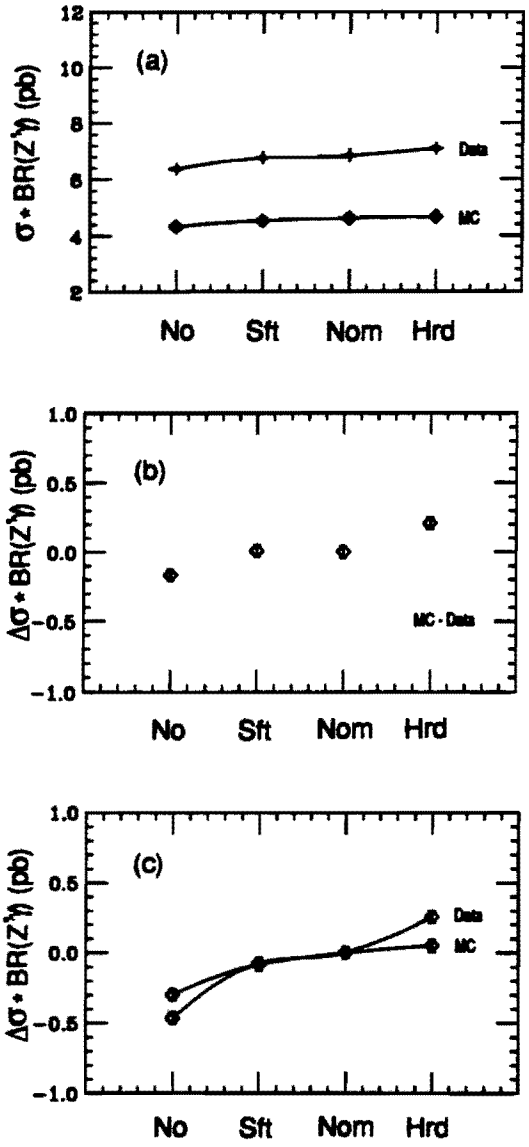

Figure 6.7: Systematic Studies of Di-Boson P_t Distributions with $\Delta R_{l\gamma} > 0.7$ and $P_t^{\gamma} > 5.0$ Gev/c using nominal HMRSB SF choice: (a)Variation of $Z\gamma$ cross-section vs. P_t choice, (b)Difference between MC and experiment for the P_t choices, (c)Systematic trends of MC and experiment separately for the P_t choices.

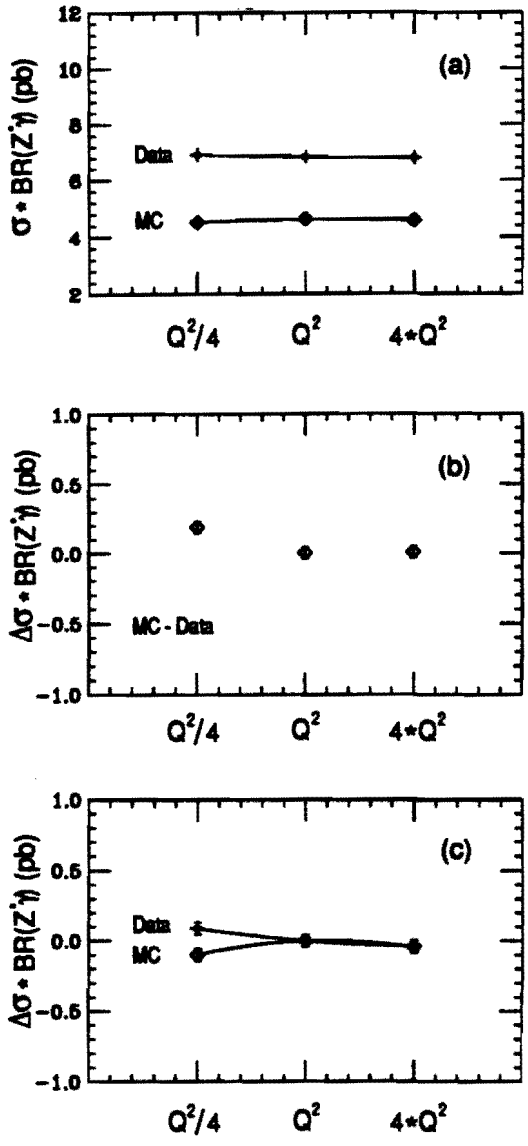

Figure 6.8: Systematic Studies of Di-Boson Q^2-scale dependence for three values of Q^2 with $\Delta R_{l\gamma} > 0.7$ and $P_t^{\gamma} > 5.0$ Gev/c using nominal HMRSB SF choice: (a)Variation of Zγ cross-section vs. Q^2 choice, (b)Difference between MC and experiment for the Q^2 choices, (c)Systematic trends of MC and experiment separately for the Q^2 choices

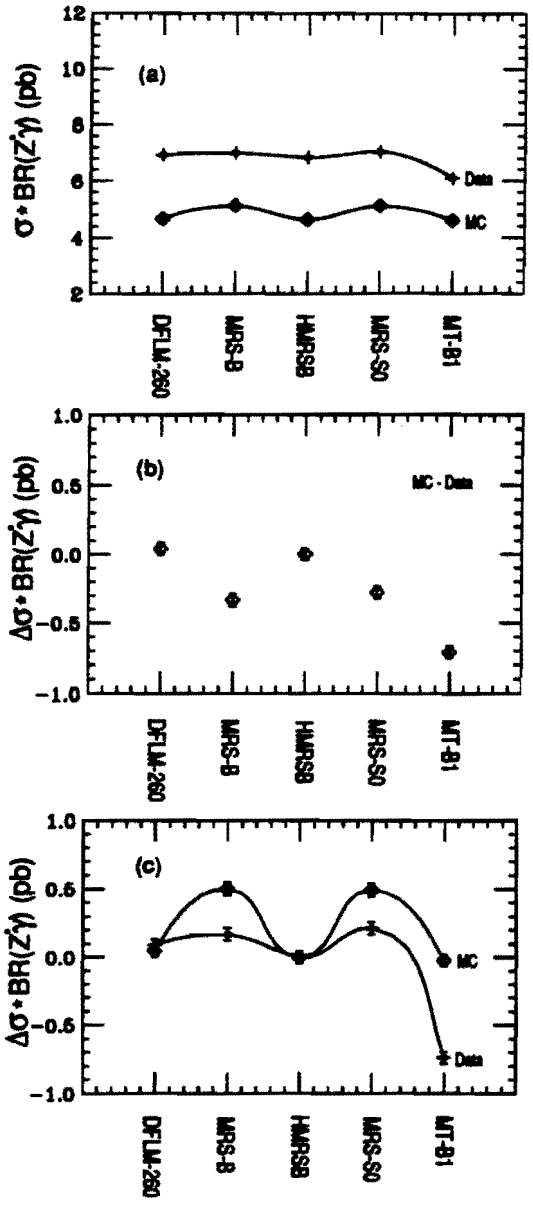

Figure 6.9: Systematic Studies of Di-Boson Structure Functions with $\Delta R_{l\gamma} > 0.7$ and $P_t^{\gamma} > 5.0$ Gev/c: (a)Variation of Zγ cross-section vs. SF choice, (b)Difference between MC and experiment for the SF choices, (c)Systematic trends of MC and experiment separately for the SF choices

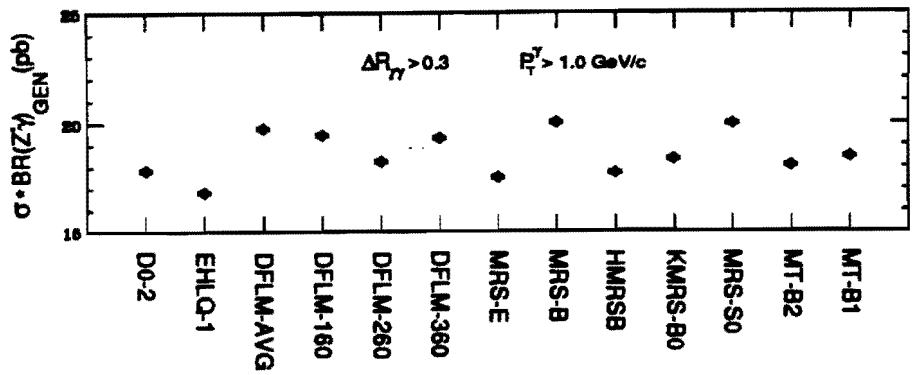

Figure 6.10: $\sigma * BR(Z^{\circ}\gamma)_{gen}$ for 13 different Di-Boson Structure Functions.

$\Delta\sigma_{MC-Expt}$ for the Q^2 scale dependency, the structure functions and the $\pm 1\sigma$ systematic excursions in the diboson P_t distributions are listed as well as the combined(in quadrature) systematic uncertainties. The details of obtaining limits on the h_{30}^Z and h_{40}^Z parameters for Zγ will be discussed in the next Chapter.

Table 6.4: Diboson Systematic Uncertainties.

$e\ Z\gamma$	$\Delta\sigma \cdot B(Z\gamma)_{MC}(pb)$	$\Delta\sigma \cdot B(Z\gamma)_{Expt}(pb)$	$\Delta\sigma \cdot B(Z\gamma)_{MC-Expt}(pb)$
P_t	$+0.05\ {}_{-0.08}$	$+0.26\ {}_{-0.07}$	$+0.21\ {}_{-0.05}$
Q^2	$+0.1\ {}_{-0.1}$	$+0.1\ {}_{-0.1}$	$+0.1\ {}_{-0.2}$
SF	$+0.5\ {}_{-0.2}$	$+0.2\ {}_{-0.7}$	$+0.7\ {}_{-0.3}$
$P_t \oplus Q^2 \oplus SF$	$+0.5\ {}_{-0.2}$	$+0.3\ {}_{-0.7}$	$+0.7\ {}_{-0.4}$

The final result for the Zγ cross section, taking into account the P_t $(Z+\gamma)$, Q^2 -scale dependence and SF systematic uncertainties, is in good agreement with the SM predictions.

$$\sigma * BR(Z+\gamma)_e = 6.8^{+5.7}_{-5.7}(stat\ +\ syst)pb$$

$$\sigma * BR(Z+\gamma)_{SM} = 4.7^{+0.7}_{-0.2}(stat\ +\ syst)pb$$

Chapter 7

Limits on $Z\gamma$ Anomalous Couplings and Summary of Results.

As mentioned briefly in Section 2.3, large values of anomalous $ZZ\gamma$ and $Z\gamma\gamma$ couplings would indicate compositeness for the Z-boson. In addition to the SM prediction for $Z\gamma$ rates, an excess of high-E_t photons accompanying the Z boson production would be expected. This is further dependent upon the nature and magnitude of the assumed non-standard couplings. Such non-SM $Z\gamma$ couplings tend to have angular distributions for hard photons that are more centrally produced than for the SM counterpart[41]. Furthermore, the behavior of the non-SM coupling values for both $ZZ\gamma$ and $Z\gamma\gamma$ processes are very similar. By obtaining an upper limit on the experimental cross-section the sensitivity to possible anomalous couplings and their upper limits can be made.

7.1 Determination of Limits.

The 68.3%, 90.0% and 95.0% CL limits on the h_{30}^Z and h_{40}^Z anomalous couplings of the $Z\gamma$ process are obtained with the Baur MC. A matrix of 58 h_{30}^Z and h_{40}^Z parameters are stepped through and the events are analyzed with the use of the fast $Z\gamma$ MC detector simulation. The cross-section $(\sigma \cdot BR(Z+\gamma)_{gen,cuts})$, the kinematical & geometrical acceptances and the predicted number of MC electron events for each cross-section point in the $h_{30}^Z - h_{40}^Z$ plane are recorded, including all statistical uncertainties for these variables.

Due to a large sensitivity to the compositeness scale Λ_Z, three different values

were studied: $\Lambda_Z = 250,\ 500$ and 750 GeV. The MC $\sigma \cdot BR(Z+\gamma)_{cuts}$ data points for the three choices are then fitted using MINUIT[57] to obtain a 3-dimensional cross-sectional view in the $h_{30}^Z - h_{40}^Z$ plane. The fit parametrization is as follows:

$$\sigma(x,y) = \sigma_{SM} + ax + bx^2 + cy + dy^2 + exy$$

where $x = (h_{30}^Z)$ and $y = (h_{40}^Z)$. Since the invariant amplitude $\mathcal{M}$ which contains the anomalous Zγ contributions is linear in its anomalous parameters; no higher-order terms in x and y are needed. The linear terms of x and y in the above equation are products of interference between the various amplitudes associated with the Zγ process. If these terms' coefficients(a,c) were zero, then the above equation would describe the surface of an elliptic paraboloid. MINUIT then returns the fitted values of σ_{SM}, a,b,c,d,e and their uncertainties. Also returned are the χ^2 of the fits and the fit residuals. The χ^2 and fit residuals are in general quite good in the region of interest(i.e. the SM) but the largest fit residuals are due to extreme values for the anomalous coupling parameters. An example of the fitted values of the coefficients for the $\sigma \cdot BR(Z+\gamma)_{e+\mu}$ cross-section surface at $\Lambda_Z = 500$ GeV is given by:

$$\sigma(h_{30}^Z, h_{40}^Z)_{Z\gamma} = 4.72 - 0.02h_{30}^Z + 0.16(h_{30}^Z)^2 - 0.06h_{40}^Z + 2.31(h_{40}^Z)^2 - 1.01(h_{30}^Z \cdot h_{40}^Z)\ \text{(pb)}$$

The systematic uncertainties for $\Delta\sigma(Z+\gamma)_{MC-Expt}$ that are associated with the diboson P_t distribution, Q^2-scale dependence and SF choice are included in the MC $\sigma * BR(Z+\gamma)_{cuts}$ curves as a function of h_{30}^Z and h_{40}^Z. By comparing MC prediction, $\sigma * BR(Z+\gamma)_{cuts}$ with the experimental result, $\sigma * BR(Z+\gamma)_{expt}$, the CL limits are obtained. Since the MC and experimental results are correlated, by virtue of their common kinematic acceptances, only the relative overall systematic uncertainty between them is relevant rather than the absolute overall systematic uncertainty. That is, the difference between the MC prediction and the experimental result, $\sigma * BR(Z+\gamma)^{overall}_{MC-expt}$.

To obtain limits on these parameters the MC surfaces are down-shifted relative to their nominal MC central-value prediction, by $-\Delta\sigma * BR(Z+\gamma)^{overall}_{MC-expt}$, where

σ is the quadrature sum of the MC statistical uncertainty on $\sigma * BR(Z+\gamma)$ and the *MC-Expt* systematic uncertainties. The limits on the h_{30}^Z and h_{40}^Z parameters are determined from the intersection of the plane containing a particular CL limit of the experimental $\sigma * BR(Z+\gamma)$ with the downshifted MC $\sigma * BR(Z+\gamma)$ surface.

We limit exploration of possible Non-SM anomalous couplings to only four cases due to large phase space combinations. Therefore only the following are considered:

$$\begin{aligned}
&(1)\ ZZ\gamma: \quad h_{30}^Z \ \&\ h_{40}^Z \quad \text{non}-\text{zero only}\\
&(2)\ ZZ\gamma: \quad h_{10}^Z \ \&\ h_{20}^Z \quad \text{non}-\text{zero only}\\
&(3)\ Z\gamma\gamma: \quad h_{30}^Z \ \&\ h_{40}^Z \quad \text{non}-\text{zero only}\\
&(4)\ Z\gamma\gamma: \quad h_{10}^Z \ \&\ h_{20}^Z \quad \text{non}-\text{zero only.}
\end{aligned}$$

Furthermore, between the CP-conserving, $h_{30,40}^{Z,\gamma}$, and CP- violating, $h_{10,20}^{Z,\gamma}$, couplings, there are no interference effects. In addition, there is only a weak interference between the ZZγ and Z$\gamma\gamma$ cases. The limits obtained on the couplings in (1) are almost the same to within $\sim 1\%$ of those obtained for (2). A similar situation holds between (3) and (4) and is a result of the nature of the ZZγ & Z$\gamma\gamma$ vertex functions.

Since the limits for Z$\gamma\gamma$ are only about 5% higher than those for ZZγ the experimental upper limits will be presented using the h_{30}^Z and h_{40}^Z ZZγ anomalous couplings of (1). These limits are within $\sim 1\%$ of the corresponding h_{10}^Z and h_{20}^Z couplings of (2), and can be further translated into the limits for (3) and (4) by inflating them with a 1.05 factor. The accuracy of these Z$\gamma\gamma$ limits computed in this fashion, therefore will be to within a few tenths of a percent.

The 68.3%, 90.0% and 95.0% CL limits on the h_{30}^Z and h_{40}^Z parameters are summarized in Table 7.1. Figure 7.1 shows the projection of the Zγ cross section on the h_{30}^Z and h_{40}^Z axes. The central value is given by the solid horizontal line, the $\pm 1\sigma$ $(stat + syst)$ uncertainty for the 68.3% double-sided CL is shown with the dotted horizontal line. The 90.0% and 95.0% single-sided CL upper limits to the experimental cross section are depicted by horizontal dashed and solid lines respectively.

Table 7.1: $Z\gamma$ $h^Z_{30,10} - h^Z_{40,20}$ Limits.

CL	$\Lambda_Z = 250$ GeV	
Range	$h^Z_{30,10}(h^Z_{40,20}=0)$	$h^Z_{40,20}(h^Z_{30,10}=0)$
68.3% DS	$0.0^{+24.6}_{-24.8}(stat+syst)$	$0.0^{+21.4}_{-21.5}(stat+syst)$
68.3% SS	$-19.7 < h^Z_{30,10} < +19.4$	$-17.0 < h^Z_{40,20} < +17.0$
90.0% SS	$-28.4 < h^Z_{30,10} < +28.1$	$-24.6 < h^Z_{40,20} < +24.5$
95.0% SS	$-32.0 < h^Z_{30,10} < +31.7$	$-27.7 < h^Z_{40,20} < +27.6$
CL	$\Lambda_Z = 500$ GeV	
Range	$h^Z_{30,10}(h^Z_{40,20}=0)$	$h^Z_{40,20}(h^Z_{30,10}=0)$
68.3% DS	$0.0^{+7.0}_{-6.9}(stat+syst)$	$0.0^{+1.9}_{-1.8}(stat+syst)$
68.3% SS	$-5.4 < h^Z_{30,10} < +5.5$	$-1.5 < h^Z_{40,20} < +1.5$†
90.0% SS	$-7.9 < h^Z_{30,10} < +8.0$	$-2.1 < h^Z_{40,20} < +2.1$†
95.0% SS	$-8.9 < h^Z_{30,10} < +9.0$†	$-2.4 < h^Z_{40,20} < +2.4$†
CL	$\Lambda_Z = 750$ GeV	
Range	$h^Z_{30,10}(h^Z_{40,20}=0)$	$h^Z_{40,20}(h^Z_{30,10}=0)$
68.3% DS	$0.0^{+3.9}_{-3.9}(stat+syst)$	$0.0^{+0.7}_{-0.7}(stat+syst)$
68.3% SS	$-3.1 < h^Z_{30,10} < +3.1$†	$-0.5 < h^Z_{40,20} < +0.5$†
90.0% SS	$-4.4 < h^Z_{30,10} < +4.4$†	$-0.8 < h^Z_{40,20} < +0.8$†
95.0% SS	$-5.0 < h^Z_{30,10} < +5.0$†	$-0.9 < h^Z_{40,20} < +0.9$†

† Exceeds unitarity limit.

The dotted line in Figure 7.1 shows the unitarity limit. The regions above the intersection of these dotted lines and the MC $\sigma * BR(Z+\gamma)_{cuts}$ curves are excluded by unitarity considerations. If the intersection of the experimental CL limit with the MC $\sigma * BR(Z+\gamma)_{cuts}$ curve happens above the unitarity line, then the experimental result doesn't have sensitivity to the anomalous parameters for the given compositeness scale Λ_Z. Note: The CL limits are derived from the $\sigma * BR(Z+\gamma)_{Expt}$ result and the h^Z_{i0} and h^Z_{i0} values are given by the Experimental - MC

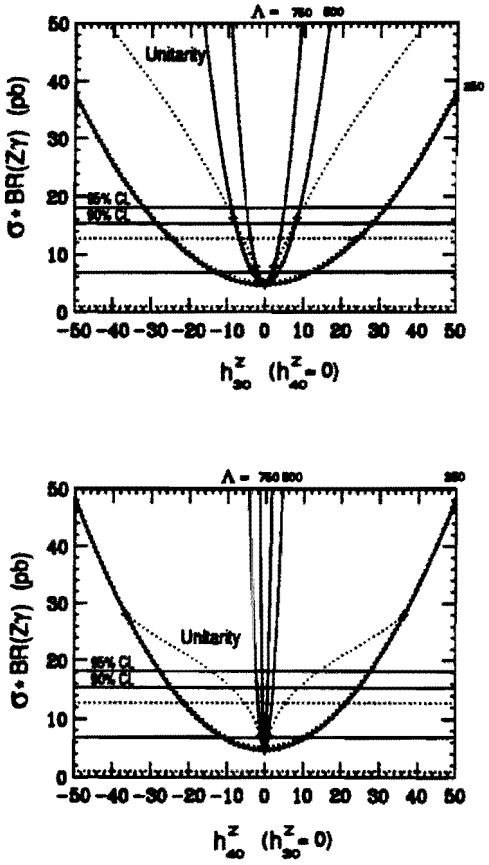

Figure 7.1: CDF limits on h^Z_{30}/h^Z_{10} and h^Z_{40}/h^Z_{20} anomalous couplings.

$\sigma * BR(Z+\gamma)$ intersection points. Those parameter values which violate unitarity for a given Λ_Z scale are denoted by a † in Table 7.1. Furthermore, the experimental limits on h_{i0}^{γ} $Z\gamma\gamma$ couplings are $\sim 5\%$ higher than the corresponding $ZZ\gamma$ couplings.

The 68.3%, 90.0% and 95.0% single-sided CL contours in the $h_{30}^Z - h_{40}^Z$ plane for $\Lambda_Z = 250,\ 500$ and 750 GeV, are shown in Figure 7.2. The 2-dimensional unitarity limit in the plane is depicted by a dotted line, where the allowed regions are those contained within these lines. For $\Lambda_Z = 250$ GeV the limits are entirely within the allowed region. The CDF sensitivity to anomalous $ZZ\gamma$ couplings from $\approx 4\ pb^{-1}$ of data are then limited by a compositeness scale of $\Lambda_Z \sim< 500$ GeV.

7.2 $Z\gamma$ Unitarity Constraints and Λ_Z Sensitivity.

Restrictions on the reduced amplitudes for arbitrary $ZZ\gamma$ coupling values are made by imposing Partial Wave Unitarity[7, 41]:

$$\sum_{\lambda_Z\lambda_\gamma} \left|A^Z_{\lambda_Z\lambda_\gamma}\right|^2 \leq \frac{24\sin^2\theta_W\cos^2\theta_W}{5\alpha^2(\hat{s})(1-\frac{M_Z^2}{\hat{s}})^3}$$

where λ_Z, λ_γ are the Z boson and photon helicities, respectively. Unitarity is violated if

$$\frac{(\frac{\hat{s}}{M_Z^2}-1)^3}{(1+\frac{\hat{s}}{\Lambda_Z^2})^6}\left[\left(h_{30}^Z - \frac{1}{2}h_{40}^Z\frac{(\frac{\hat{s}}{M_Z^2}-1)}{(1+\frac{\hat{s}}{\Lambda_Z^2})}\right)^2 + (h_{30}^Z)^2\frac{M_Z^2}{\hat{s}}\right] \geq \frac{48\sin^2\theta_W\ \cos^2\theta_W}{5\alpha^2(\hat{s})}$$

Assume the generalized form factor and its powers(n=3 for h_{30}^Z n=4 for h_{40}^Z) and that the center-of-mass energy range is $M_Z < \sqrt{\hat{s}} < 1.8$ TeV. In addition, one can replace $h_{30}^Z \rightarrow h_{10}^Z$ and $h_{40}^Z \rightarrow h_{20}^Z$ to get the analogous unitarity relation for those parameters [58].

Similarly for the $Z\gamma\gamma$ case, partial wave unitarity restricts the reduced amplitudes for arbitrary coupling values to:

$$\sum_{\lambda_Z\lambda_\gamma} \left|A^Z_{\lambda_Z\lambda_\gamma}\right|^2 \leq \frac{3(3-6\sin^2\theta_W+8\sin^4\theta_W)}{5\alpha^2(\hat{s})(1-\frac{M_Z^2}{\hat{s}})^3}$$

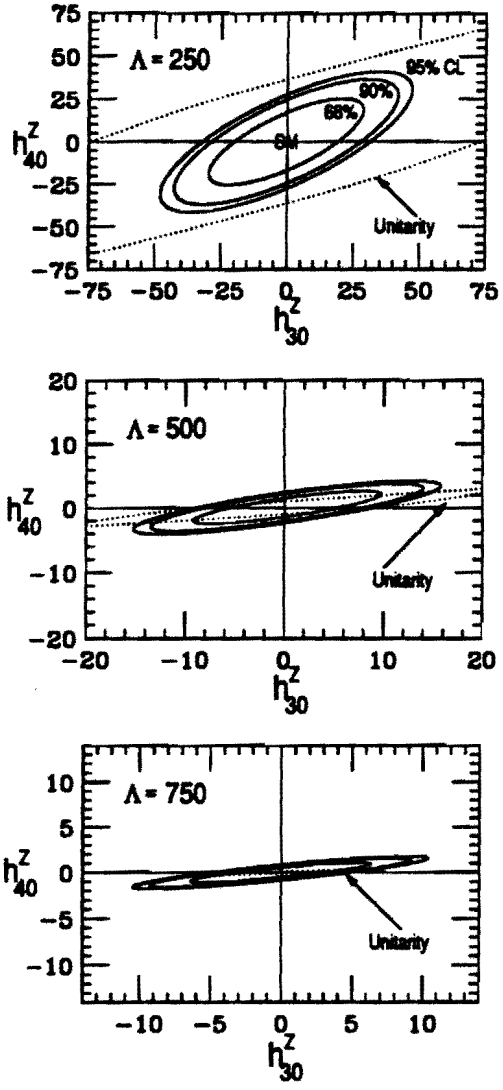

Figure 7.2: CDF h_{30}^Z/h_{10}^Z - h_{40}^Z/h_{20}^Z contours for $Z\gamma$ in the electron channel.

and unitarity for the h_{30}^{γ} and h_{40}^{γ} parameters is violated if:

$$\frac{(\frac{\hat{s}}{M_Z^2}-1)^3}{(1+\frac{\hat{s}}{\Lambda_Z^2})^6}\left[\left(h_{30}^{\gamma}-\frac{1}{2}h_{40}^{\gamma}\frac{(\frac{\hat{s}}{M_Z^2}-1)}{(1+\frac{\hat{s}}{\Lambda_Z^2})}\right)^2+(h_{30}^{\gamma})^2\frac{M_Z^2}{\hat{s}}\right] \geq \frac{6(3-6\sin^2\theta_W+8\sin^4\theta_W)}{5\alpha^2(\hat{s})}$$

Assuming that $\Lambda_Z >> M_Z$ and that only one anomalous coupling is non-zero at a time, the maximum values of h_{i0}^Z and h_{i0}^Z are restricted by tree-level unitarity to be[7]:

$$\begin{aligned} |h_{10}^Z|, |h_{30}^Z| &< \tfrac{1.00\ TeV^3}{\Lambda_Z^3} \quad (h_{20}^Z = h_{40}^Z = 0, n = 3) \\ |h_{20}^Z|, |h_{30}^Z| &< \tfrac{1.00\ TeV^5}{\Lambda_Z^5} \quad (h_{10}^Z = h_{30}^Z = 0, n = 4). \end{aligned}$$

Figure 7.3 is a 2-dimensional representation of the ZZγ and Z$\gamma\gamma$ unitarity limits for Λ_Z = 250, 500 and 750 GeV in the $h_{30}^Z - h_{40}^Z(h_{10}^Z - h_{20}^Z)$ plane. The dotted line indicates the unitarity limit and those regions contained within these confines are allowed by unitarity considerations. The limits for $\Lambda_Z = 250$ are entirely within the allowed region but as Λ_Z increases to 500 and 750 GeV this allowed region becomes tighter. In particular, nearly all the limits for $\Lambda_Z = 750$ are outside the unitarity bound for the $h_{30}^Z - h_{40}^Z(h_{10}^Z - h_{20}^Z)$ plane.

The experimental limits for the ZZγ and Z$\gamma\gamma$ anomalous couplings are superimposed on the unitarity curve as a function of energy Λ_Z, as shown in Figure 7.3. At the 95% CL, the upper limits on these couplings corresponds to a compositeness scale sensitivity of $\Lambda_Z \sim 450 - 500$ GeV for $h_{30}^{Z,\gamma}/h_{10}^{Z,\gamma}$ and $\Lambda_Z \sim 300$ GeV for $h_{40}^{Z,\gamma}/h_{20}^{Z,\gamma}$.

This scale sensitivity can be further expressed in terms of distance for possible internal Z-boson structure of

$$\begin{aligned} L_Z = \tfrac{\hbar c}{\Lambda_Z} &\leq (3.9 - 6.6) \times 10^{-4} \text{ fm} \\ &\leq (0.18 - 0.30)\lambda\!\!\!^{-}_Z \end{aligned}$$

where $\lambda\!\!\!^{-}_Z = \frac{\hbar c}{M_Z c^2}$ is the reduced Compton wavelength of the Z-boson.

7.3 Comparison with L3 Limits.

Recently the L3 Collaboration published limits on the h_3^Z form factor (which they denote as β). The limits were derived from a measurement of the $e^+e^- \rightarrow Z^o \rightarrow \nu\bar{\nu}\gamma$ cross-section. Their 95% CL limit for 11.2 pb^{-1} of data based on the absence of excess events in the Z resonance region is given as $|\beta| < 1.6$, where $E_\gamma > \frac{1}{2}E_{beam}$[59]. The corresponding limits on the h_{30}^Z parameter translates as $|h_{30}^Z| < 2.3, 1.8, 1.7$ for Λ_Z = 250, 500 and 750 GeV respectively. For these Λ_Z values, their parameter results are well within the unitarity limit. It takes a $\Lambda_Z > 840$ GeV before the L3 $|h_{30}^Z|$ unitarity limit is exceeded. We have analyzed the CDF $Z\gamma$ data in terms of limits on the $ZZ\gamma$ couplings, and the LEP $Z \rightarrow \nu\bar{\nu}\gamma$ results are also sensitive to this process where no constraint has been made on the $Z\gamma\gamma$ couplings. However, as mentioned in Chapter 2 the $Z\gamma\gamma$ couplings differ from the $ZZ\gamma$ by only a few percent.

7.4 Z-boson Transition Moment Limits

As stated in Chapter 2 the transition moments of the Z-boson are related to the h_{io}^Z anomalous $ZZ\gamma$ coulings by:

$$\begin{aligned} d_{Z_T} &= -\frac{e}{M_Z}\frac{1}{\sqrt{2}}\frac{k^2}{M_Z^2}(h_{30}^Z - h_{40}^Z) \\ Q_{Z_T}^m &= \frac{e}{M_Z^2}\sqrt{10}\,(2h_{30}^Z) \\ \mu_{Z_T} &= -\frac{e}{M_Z}\frac{1}{\sqrt{2}}\frac{k^2}{M_Z^2}(h_{10}^Z - h_{20}^Z) \\ Q_{Z_T}^e &= \frac{e}{M_Z^2}\sqrt{10}\,(2h_{10}^Z). \end{aligned}$$

These relations allow the experimental limits of the h_{io}^Z anomalous couplings to place bounds on the transition moments. At tree level all the SM $ZZ\gamma$ couplings vanish($h_{io}^Z = 0$) thus all SM transition moments must also vanish. The following

classical parameters for the Z-boson are defined and their numerical values are calculated to be:

$$\begin{aligned}
d^{o}_{Z_T} &= -\tfrac{1}{2}e\lambda\!\!\!^{-}_{Z} &&= -1.0820 \pm 0.0001 \times 10^{-3}\ e-\text{fm} \\
Q^{mo}_{Z_T} &= \tfrac{e\hbar^2}{M_Z^2 c} &&= 1.4038 \pm 0.0002 \times 10^{-18}\ \text{MeV}-\text{fm/T} \\
\mu^{o}_{Z_T} &= -\tfrac{e\hbar}{2M_Z} &&= -3.2437 \pm 0.0003 \times 10^{-16}\ \text{MeV/T} \\
Q^{eo}_{Z_T} &= e\lambda\!\!\!^{-2}_{Z} &&= 4.6828 \pm 0.0007 \times 10^{-6}\ e-\text{fm}^2 \\
\lambda\!\!\!^{-}_{Z} &= \tfrac{\hbar c}{M_Z c^2} &&= 2.1640 \pm 0.0002 \times 10^{-3}\ \text{fm}
\end{aligned}$$

The following dimensionless(scaled) classical quantities for the Z-boson we have defined to be:

$$\begin{aligned}
\delta_{Z_T} \equiv \frac{d_{Z_T}}{d^{o}_{Z_T}} &= \sqrt{2}\left[\frac{k^2}{M_Z^2}\right](h^Z_{30} - h^Z_{40}) \\
q^{m}_{Z_T} \equiv \frac{Q^{m}_{Z_T}}{Q^{mo}_{Z_T}} &= \sqrt{10}\,(2h^Z_{30}) \\
g_{Z_T} \equiv \frac{\mu_{Z_T}}{\mu^{o}_{Z_T}} &= \sqrt{2}\left[\frac{k^2}{M_Z^2}\right](h^Z_{10} - h^Z_{20}) \\
q^{e}_{Z_T} \equiv \frac{Q^{e}_{Z_T}}{Q^{eo}_{Z_T}} &= \sqrt{10}\,(2h^Z_{10})
\end{aligned}$$

However, the factor $(\frac{k^2}{M_Z^2})$ is somewhat ill-defined for setting limits on δ_{Z_T} and g_{Z_T} due to the nature of the $Z+\gamma$ process and we therefore define the variables $\delta^{*}_{Z_T}$ and $g^{*}_{Z_T}$ as:

$$\begin{aligned}
\delta^{*}_{Z_T} \equiv \delta_{Z_T}\left[\frac{M_Z^2}{k^2}\right] &= \sqrt{2}(h^Z_{30} - h^Z_{40}) \\
g^{*}_{Z_T} \equiv g_{Z_T}\left[\frac{M_Z^2}{k^2}\right] &= \sqrt{2}(h^Z_{10} - h^Z_{20})
\end{aligned}$$

These $\delta^{*}_{Z_T}$ and $g^{*}_{Z_T}$ limits are a factor of $\sqrt{2}$ greater than the corresponding limits on the $(h^Z_{io} - h^Z_{jo})$ parameters. Similarly the $q^{m}_{Z_T}$ and $q^{e}_{Z_T}$ limits are a factor of $2\sqrt{10}$ larger than those in Table 7.1 for the individual electron Zγ results. Note: Since experimental limits on $h^Z_{30}(h^Z_{40})$ are the same as for $h^Z_{10}(h^Z_{20})$, the limits on $\delta^{*}_{Z_T}$ and $g^{*}_{Z_T}$ are also the same; likewise for $q^{m}_{Z_T}$ and $q^{e}_{Z_T}$. Figure 7.4 show the 68% and 95% CL contours in the $\delta^{*}_{Z_T} - q^{m}_{Z_T}$ plane analogous to the contours in Figure 7.2 of the $h^Z_{30} - h^Z_{40}$ planes.

7.5 Summary of Results

The analysis of CDF $Z\gamma$ data, as described in this document has provided a measurement of the $Z\gamma$ cross-section which itself has made possible the determination of the limits on the $ZZ\gamma$ and $Z\gamma\gamma$ anomalous couplings.

Our experimental results on the measurement of $\sigma * BR(Z+\gamma)$ are in good agreement with the SM prediction. To summarize; the observed $Z\gamma$ cross-section and the Standard Model $Z\gamma$ cross-section are given by:

$$\sigma * BR(Z+\gamma)_e = 6.8^{+5.7}_{-5.7}(stat \ + \ syst)pb$$

$$\sigma * BR(Z+\gamma)_{SM} = 4.7^{+0.7}_{-0.2}(stat \ + \ syst)pb$$

In addition, from this cross-section result, direct limits on the anomalous coupling parameters ($h_{30}^{Z,\gamma}$ and $h_{40}^{Z,\gamma}$) and ($h_{10}^{Z,\gamma}$ and $h_{20}^{Z,\gamma}$) for $ZZ\gamma$ and $Z\gamma\gamma$ have been obtained for the three different choices of compositeness scale sensitivity Λ_Z. Therefore, the compositeness sensitivity scale of such anomalous couplings for saturation at unitarity, shows $\Lambda_Z \approx 450 - 500$ GeV for $h_{30,10}^{Z,\gamma}$ and $\Lambda_Z \approx 300$ GeV for $h_{40,20}^{Z,\gamma}$. Furthermore, these experimental limits for the anomalous $ZZ\gamma$ couplings place restrictions on the transition moments and are sensitive to $\Lambda_Z \geq 300 - 500$ GeV. This compositeness scale then probes possible internal Z-boson structure at a distance scale of order $L_Z \leq (3.9 - 6.6) \times 10^{-4}$ fm $= (0.18 - 0.30)\lambda\!\!\!^{-}_Z$ at the 95% CL.

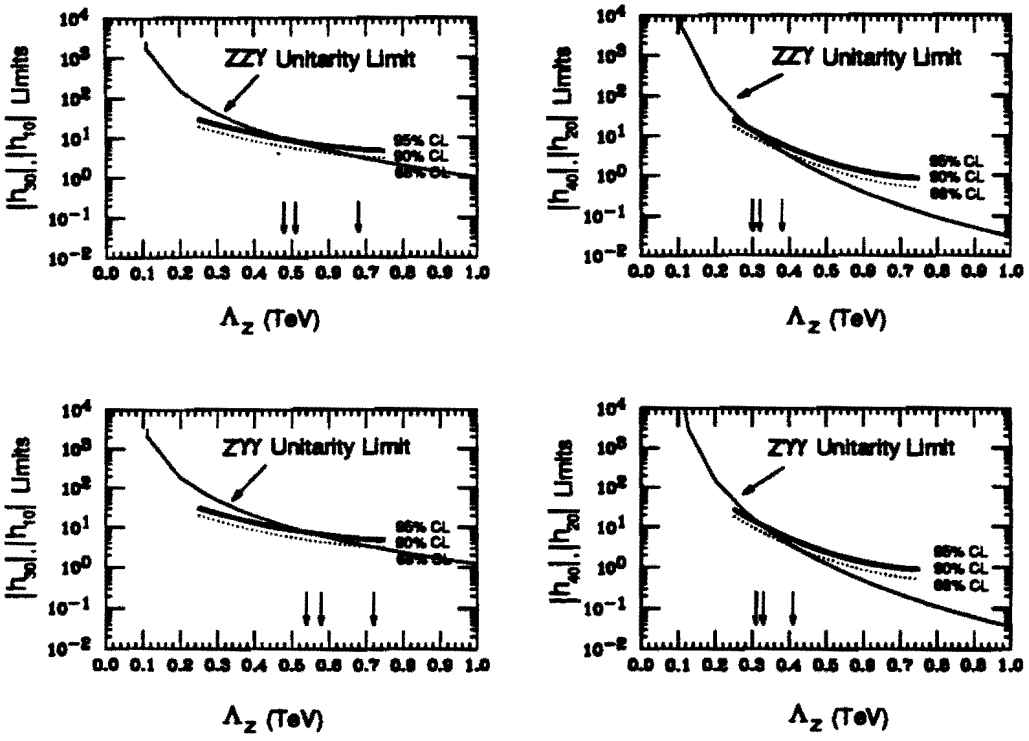

Figure 7.3: Unitarity limits as a function of Λ_Z for anomalous $ZZ\gamma$ and $Z\gamma\gamma$ couplings.

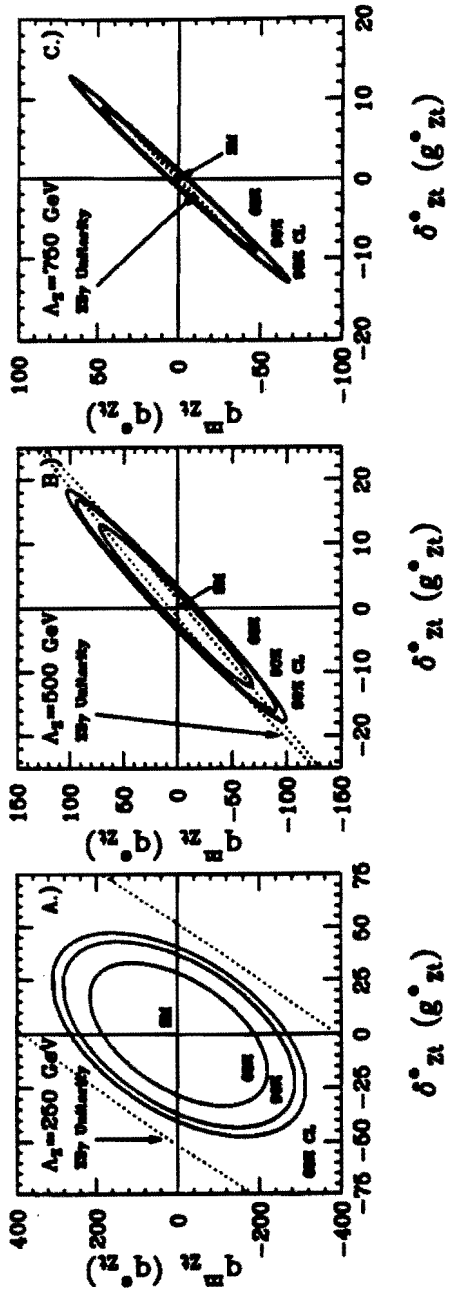

Figure 7.4: $\delta^s_{Z_T} - q^m_{Z_T}(g^s_{Z_T} - q^e_{Z_T})$ transition moment contour limits. The solid ellipses show the 68 and 95% CL limits in the $\delta^s_{Z_T} - q^m_{Z_T}(g^s_{Z_T} - q^e_{Z_T})$ planes for anomalous $ZZ\gamma$ couplings with Λ_Z = 250, 500 and 750 GeV, respectively. The $ZZ\gamma$ unitarity limits for the relevant compositeness scale Λ_Z are indicated by dotted curves in Figs. (A)-(C).

Appendix A
CDF Collaboration

F. Abe,[12] M. Albrow,[6] D. Amidei,[15] C. Anway-Wiese,[3] G. Apollinari,[23] M. Atac,[6] P. Auchincloss,[22] P. Azzi,[17] N. Bacchetta,[16] A. R. Baden,[8] W. Badgett,[15] M. W. Bailey,[21] A. Bamberger,[6,a] P. de Barbaro,[22] A. Barbaro-Galtieri,[13] V. E. Barnes,[21] B. A. Barnett,[11] G. Bauer,[14] T. Baumann,[8] F. Bedeschi,[20] S. Behrends,[2] S. Belforte,[20] G. Bellettini,[20] J. Bellinger,[28] D. Benjamin,[27] J. Benlloch,[14] J. Bensinger,[2] A. Beretvas,[6] J. P. Berge,[6] S. Bertolucci,[7] K. Biery,[10] S. Bhadra,[9] M. Binkley,[6] D. Bisello,[17] R. Blair,[1] C. Blocker,[2] A. Bodek,[22] V. Bolognesi,[20] A. W. Booth,[6] C. Boswell,[11] G. Brandenburg,[8] D. Brown,[8] E. Buckley-Geer,[6] H. S. Budd,[22] G. Busetto,[17] A. Byon-Wagner,[6] K. L. Byrum,[1] C. Campagnari,[6] M. Campbell,[15] A. Caner,[6] R. Carey,[8] W. Carithers,[13] D. Carlsmith,[28] J. T. Carroll,[6] R. Cashmore,[6,a] A. Castro,[17] Y. Cen,[18] F. Cervelli,[20] K. Chadwick,[6] J. Chapman,[15] G. Chiarelli,[7] W. Chinowsky,[13] S. Cihangir,[6] A. G. Clark,[6] M. Cobal,[20] D. Connor,[18] M. Contreras,[4] J. Cooper,[6] M. Cordelli,[7] D. Crane,[6] J. D. Cunningham,[2] C. Day,[6] F. DeJongh,[6] S. Dell'Agnello,[20] M. Dell'Orso,[20] L. Demortier,[23] B. Denby,[6] P. F. Derwent,[15] T. Devlin,[24] D. DiBitonto,[25] M. Dickson,[22] R. B. Drucker,[13] A. Dunn,[15] K. Einsweiler,[13] J. E. Elias,[6] R. Ely,[13] S. Eno,[4] D. Errede,[9] S. Errede,[9] A. Etchegoyen,[6,a] B. Farhat,[14] M. Frautschi,[16] G. J. Feldman,[8] B. Flaugher,[6] G. W. Foster,[6] M. Franklin,[8] J. Freeman,[6] H. Frisch,[4] T. Fuess,[6] Y. Fukui,[12] A. F. Garfinkel,[21] A. Gauthier,[9] S. Geer,[6] D. W. Gerdes,[15] P. Giannetti,[20] N. Giokaris,[23] P. Giromini,[7] L. Gladney,[18] M. Gold,[16] J. Gonzalez,[18] K. Goulianos,[23]

H. Grassmann,[17] G. M. Grieco,[20] R. Grindley,[10] C. Grosso-Pilcher,[4] C. Haber,[13] S. R. Hahn,[6] R. Handler,[28] K. Hara,[26] B. Harral,[18] R. M. Harris,[6] S. A. Hauger,[5] J. Hauser,[3] C. Hawk,[24] T. Hessing,[25] R. Hollebeek,[18] L. Holloway,[9] A. Hölscher,[10] S. Hong,[15] G. Houk,[18] P. Hu,[19] B. Hubbard,[13] B. T. Huffman,[19] R. Hughes,[22] P. Hurst,[8] J. Huth,[6] J. Hylen,[6] M. Incagli,[20] T. Ino,[26] H. Iso,[26] H. Jensen,[6] C. P. Jessop,[8] R. P. Johnson,[6] U. Joshi,[6] R. W. Kadel,[13] T. Kamon,[25] S. Kanda,[26] D. A. Kardelis,[9] I. Karliner,[9] E. Kearns,[8] L. Keeble,[25] R. Kephart,[6] P. Kesten,[2] R. M. Keup,[9] H. Keutelian,[6] D. Kim,[6] S. B. Kim,[15] S. H. Kim,[26] Y. K. Kim,[13] L. Kirsch,[2] K. Kondo,[26] J. Konigsberg,[8] K. Kordas,[10] E. Kovacs,[6] M. Krasberg,[15] S. E. Kuhlmann,[1] E. Kuns,[24] A. T. Laasanen,[21] S. Lammel,[3] J. I. Lamoureux,[28] S. Leone,[20] J. D. Lewis,[6] W. Li,[1] P. Limon,[6] M. Lindgren,[3] T. M. Liss,[9] N. Lockyer,[18] M. Loreti,[17] E. H. Low,[18] D. Lucchesi,[20] C. B. Luchini,[9] P. Lukens,[6] P. Maas,[28] K. Maeshima,[6] M. Mangano,[20] J. P. Marriner,[6] M. Mariotti,[20] R. Markeloff,[28] L. A. Markosky,[28] J. A. J. Matthews,[16] R. Mattingly,[2] P. McIntyre,[25] A. Menzione,[20] E. Meschi,[20] T. Meyer,[25] S. Mikamo,[12] M. Miller,[4] T. Mimashi,[26] S. Miscetti,[7] M. Mishina,[12] S. Miyashita,[26] Y. Morita,[26] S. Moulding,[23] J. Mueller,[24] A. Mukherjee,[6] T. Muller,[3] L. F. Nakae,[2] I. Nakano,[26] C. Nelson,[6] D. Neuberger,[3] C. Newman-Holmes,[6] J. S. T. Ng,[8] M. Ninomiya,[26] L. Nodulman,[1] S. Ogawa,[26] R. Paoletti,[20] V. Papadimitriou,[6] A. Para,[6] E. Pare,[8] S. Park,[6] J. Patrick,[6] G. Pauletta,[20] L. Pescara,[17] T. J. Phillips,[5] A. G. Piacentino,[20] R. Plunkett,[6] L. Pondrom,[28] J. Proudfoot,[1] F. Ptohos,[8] G. Punzi,[20] D. Quarrie,[6] K. Ragan,[10] G. Redlinger,[4] J. Rhoades,[28] M. Roach,[27] F. Rimondi,[6,a] L. Ristori,[20] W. J. Robertson,[5] T. Rodrigo,[6] T. Rohaly,[18] A. Roodman,[4] W. K. Sakumoto,[22] A. Sansoni,[7] R. D. Sard,[9] A. Savoy-Navarro,[6] V. Scarpine,[9] P. Schlabach,[8], E. E. Schmidt,[6] O. Schneider,[13] M. H. Schub,[21] R. Schwitters,[8] G. Sciacca,[20] A. Scribano,[20]

S. Segler,[6] S. Seidel,[16] Y. Seiya,[26] G. Sganos,[10] M. Shapiro,[13] N. M. Shaw,[21] M. Sheaff,[28] M. Shochet,[4] J. Siegrist,[13] A. Sill,[22] P. Sinervo,[10] J. Skarha,[11] K. Sliwa,[27] D. A. Smith,[20] F. D. Snider,[11] L. Song,[6] T. Song,[15] M. Spahn,[13] P. Sphicas,[14] A. Spies,[11] R. St. Denis,[8] L. Stanco,[17] A. Stefanini,[20] G. Sullivan,[4] K. Sumorok,[14] R. L. Swartz, Jr.,[9] M. Takano,[26] K. Takikawa,[26] S. Tarem,[2] F. Tartarelli,[20] S. Tether,[14] D. Theriot,[6] M. Timko,[27] P. Tipton,[22] S. Tkaczyk,[6] A. Tollestrup,[6] J. Tonnison,[21] W. Trischuk,[8] Y. Tsay,[4] J. Tseng,[11] N. Turini,[20] F. Ukegawa,[26] D. Underwood,[1] S. Vejcik, III,[15] R. Vidal,[6] R. G. Wagner,[1] R. L. Wagner,[6] N. Wainer,[6] R. C. Walker,[22] J. Walsh,[18] A. Warburton,[10] G. Watts,[22] T. Watts,[24] R. Webb,[25] C. Wendt,[28] H. Wenzel,[20] W. C. Wester, III,[13] T. Westhusing,[9] S. N. White,[23] A. B. Wicklund,[1] E. Wicklund,[6] H. H. Williams,[18] B. L. Winer,[22] J. Wolinski,[25] D. Y. Wu,[15] X. Wu,[20] J. Wyss,[17] A. Yagil,[6] K. Yasuoka,[26] Y. Ye,[10] G. P. Yeh,[6] J. Yoh,[6] M. Yokoyama,[26] J. C. Yun,[6] A. Zanetti,[20] F. Zetti,[20] S. Zhang,[15] W. Zhang,[18] S. Zucchelli,[6,a]

[1] *Argonne National Laboratory, Argonne, Illinois 60439*

[2] *Brandeis University, Waltham, Massachusetts 02254*

[3] *University of California at Los Angeles, Los Angeles, California 90024*

[4] *University of Chicago, Chicago, Illinois 60637*

[5] *Duke University, Durham, North Carolina 27706*

[6] *Fermi National Accelerator Laboratory, Batavia, Illinois 60510*

[7] *Laboratori Nazionali di Frascati, Istituto Nazionale di Fisica Nucleare, Frascati, Italy*

[8] *Harvard University, Cambridge, Massachusetts 02138*

[9] *University of Illinois, Urbana, Illinois 61801*

[10] *Institute of Particle Physics, McGill University, Montreal, and University of Toronto, Toronto, Canada*

[11] *The Johns Hopkins University, Baltimore, Maryland 21218*

[12] *National Laboratory for High Energy Physics (KEK), Japan*

[13] *Lawrence Berkeley Laboratory, Berkeley, California 94720*

[14] *Massachusetts Institute of Technology, Cambridge, Massachusetts 02139*

[15] *University of Michigan, Ann Arbor, Michigan 48109*

[16] *University of New Mexico, Albuquerque, New Mexico 87131*

[17] *Universita di Padova, Instituto Nazionale di Fisica Nucleare, Sezione di Padova, I-35131 Padova, Italy*

[18] *University of Pennsylvania, Philadelphia, Pennsylvania 19104*

[19] *University of Pittsburgh, Pittsburgh, Pennsylvania 15260*

[20] *Istituto Nazionale di Fisica Nucleare, University and Scuola Normale Superiore of Pisa, I-56100 Pisa, Italy*

[21] *Purdue University, West Lafayette, Indiana 47907*

[22] *University of Rochester, Rochester, New York 15627*

[23] *Rockefeller University, New York, New York 10021*

[24] *Rutgers University, Piscataway, New Jersey 08854*

[25] *Texas A&M University, College Station, Texas 77843*

[26] *University of Tsukuba, Tsukuba, Ibaraki 305, Japan*

[27] *Tufts University, Medford, Massachusetts 02155*

[28] *University of Wisconsin, Madison, Wisconsin 53706*

Appendix B

Acceptance × Efficiency Factors for the Determination of $\sigma \cdot B(Z+\gamma)$ in the Electron Channel

The explicit forms of the product term $(A_{Z\gamma} \cdot \epsilon_{Z\gamma})$ are given below:

$$\begin{aligned} A_{Z\gamma} \cdot \epsilon_{Z\gamma} &= \frac{1}{f_{DY}} \cdot \epsilon_{zvx} \cdot A_{M_Z} \cdot (A_Z \cdot T \cdot \epsilon_{cent_T}) \\ &\quad \times \Big[\{ f_{Zcc} \cdot (2\epsilon_{cent_L} - T \cdot \epsilon_{cent_T}) \} \cdot (f^{\gamma}_{Zcc} \cdot A^{\gamma}_{Zcc} \cdot \epsilon^{\gamma}_{cem}) \\ &\quad + (f_{Zcp} \cdot \epsilon_{plug}) \cdot \left(f^{\gamma}_{Zcp} \cdot A^{\gamma}_{Zcp} \cdot \epsilon^{\gamma}_{cem} \right) \\ &\quad + (f_{Zcf} \cdot \epsilon_{fwrd}) \cdot \left(f^{\gamma}_{Zcf} \cdot A^{\gamma}_{Zcf} \cdot \epsilon^{\gamma}_{cem} \right) \Big] \\ &= \frac{1}{f_{DY}} \cdot \epsilon_{zvx} \cdot A_{M_Z} \cdot (T \cdot \epsilon_{cent_T}) \\ &\quad \times \Big[\{ A_{Zcc} \cdot (2\epsilon_{cent_L} - T \cdot \epsilon_{cent_T}) \} \cdot (f^{\gamma}_{Zcc} \cdot A^{\gamma}_{Zcc} \cdot \epsilon^{\gamma}_{cem}) \\ &\quad + (A_{Zcp} \cdot \epsilon_{plug}) \cdot \left(f^{\gamma}_{Zcp} \cdot A^{\gamma}_{Zcp} \cdot \epsilon^{\gamma}_{cem} \right) \\ &\quad + (A_{Zcf} \cdot \epsilon_{fwrd}) \cdot \left(f^{\gamma}_{Zcf} \cdot A^{\gamma}_{Zcf} \cdot \epsilon^{\gamma}_{cem} \right) \Big] \end{aligned} \tag{B.1}$$

For $Z\gamma$ events, f_{DY} (< 1) is a small correction factor which explicitly takes into account the removal of the Drell-Yan $DY + \gamma$ contribution within the $Z \rightarrow e^+e^-$ mass window, and also corrects for the loss of $Z + \gamma$ events outside the $Z \rightarrow e^+e^-$ mass window. The factor ϵ_{zvx} is the efficiency of the $|z_{\text{vertex}}| < 60$ cm cut.

The overall kinematic × geometrical acceptance factor, $A_Z = A_{Zcc} + A_{Zcp} + A_{Zcf}$, consists of three fiducial classes of central-central, central-plug and central-forward dielectrons from Z decay, respectively. These factors are themselves products of individual kinematic × geometrical acceptance factors:

$$A_{Zcx} = \left(A^{e_1}_{Zc\ E_T} \cdot A^{e_1}_{Zc\ fid\ cem} \right) \cdot \left(A^{e_2}_{Zx\ E_T} \cdot A^{e_2}_{Zx\ fid} \right) \tag{B.2}$$

where $cx = cc$, cp or cf. $A^{e_1}_{Zc\ E_T}$ is the kinematic acceptance of an electron passing the "tight" $E_T > 20$ GeV selection cut and $A^{e_1}_{Zc\ fid\ cem}$ is the geometrical fiducial acceptance associated with the central EM calorimeter. $A^{e_2}_{Zx\ E_T}$ is the kinematic acceptance of an electron passing the "loose" $E_T > 10$ GeV selection cut, and $A^{e_2}_{Zx\ fid}$ is the geometrical acceptance associated with the fiducial acceptance of the central, plug or forward EM calorimeters ($x = c$, p, or f). Furthermore, acceptance fractions f_{Zcc}, f_{Zcp} and f_{Zcf} are related by $f_{Zcc} = A_{Zcc}/A_Z$, $f_{Zcp} = A_{Zcp}/A_Z$ and $f_{Zcf} = A_{Zcf}/A_Z$.

$T = \epsilon_{L1} \cdot \epsilon_{L2} \cdot \epsilon_{L3}$ is the overall Z lepton trigger efficiency for the "tight" central lepton selection, where ϵ_{L1}, ϵ_{L2}, and ϵ_{L3} are the individual level-1 - level-3 lepton trigger efficiencies, respectively. The overall "tight" and "loose" central fiducial electron selection efficiencies, are given by:

$$\epsilon_{cent_T} = \epsilon^{cem}_{iso} \cdot \epsilon^{cem}_{(Had/EM)_T} \cdot \epsilon^{cem}_{\chi^2_{strip}} \cdot \epsilon^{cem}_{Lshr} \cdot \epsilon^{cem}_{(E/P)_T} \cdot \epsilon^{cem}_{trk} \cdot \epsilon^{cem}_{\Delta z} \cdot \epsilon^{cem}_{\Delta x}. \quad \text{(B.3)}$$

$$\epsilon_{cent_L} = \epsilon^{cem}_{iso} \cdot \epsilon^{cem}_{(Had/EM)_L} \cdot \epsilon^{cem}_{(E/P)_L}. \quad \text{(B.4)}$$

where the individual efficiencies for the common central electron selection are listed in section 4.2.4.

The overall plug and forward electron selection efficiencies are given by

$$\epsilon_{plug} = \epsilon^{pem}_{iso} \cdot \epsilon^{pem}_{(Had/EM)} \cdot \epsilon^{pem}_{\chi^2_{3x3}} \cdot \epsilon^{pem}_{vtpc}. \quad \text{(B.5)}$$

$$\epsilon_{fwrd} = \epsilon^{fem}_{iso} \cdot \epsilon^{fem}_{(Had/EM)}. \quad \text{(B.6)}$$

again the individual common plug and forward electron selection efficiencies are as listed in section 4.2.4.

The factors f^{γ}_{Zcc}, f^{γ}_{Zcp} and f^{γ}_{Zcf} are defined as the fraction of all photons that are central ($|\eta_\gamma| < 1.1$), which have already satisfied the $E^{\gamma}_T > 5.0$ GeV and $\Delta R_{e\gamma} > 0.7$

requirements, and are produced by Z decay electrons which pass the selection requirements for each class of central-central, central-plug and central-forward fiducial-fiducial Z bosons, respectively. The factors A^{γ}_{Zcc}, A^{γ}_{Zcp} and A^{γ}_{Zcf} represent the individual overall acceptances associated with central photons passing all photon cuts for central-central, central-plug and central-forward fiducial-fiducial dielectrons, respectively, and are a product of individual central photon acceptances:

$$\begin{aligned} A^{\gamma}_{Zcx} &= A^{\gamma}_{Zcx\ E_T^{\gamma}} \cdot A^{\gamma}_{Zcx\ fid\ cem} \cdot A^{\gamma}_{Zcx\ \Delta R_{e\gamma}} = 1.0 \cdot A^{\gamma}_{Zcx\ fid\ cem} \cdot 1.0 \\ &= A^{\gamma}_{Zcx\ fid\ cem} \end{aligned} \tag{B.7}$$

The kinematic acceptance factor $A^{\gamma}_{Zcx\ E_T^{\gamma}} = 1.0$, since all central photons associated with cx Z bosons must intrinsically pass the $E_T^{\gamma} > 5.0$ GeV requirement. In addition, the lepton-photon angular separation acceptance factor, $A^{\gamma}_{Zcx\ \Delta R_{e\gamma}} = 1.0$, since all central photons associated with Z bosons must intrinsically pass the $\Delta R_{e\gamma} > 0.7$ angular separation requirement applied to both decay leptons.

The factor $A^{\gamma}_{Zcx\ fid\ cem}$ is the geometrical acceptance for photons, which are in the central ($|\eta_{\gamma}| < 1.1$) region associated with cx Z bosons with Z decay leptons passing the selection requirements and central photons already satisfying the $E_T^{\gamma} > 5.0$ GeV and $\Delta R_{e\gamma} > 0.7$ requirements, that pass the CEM fiducial requirements.

Therefore, $f^{\gamma}_{Zcx} \cdot A^{\gamma}_{Zcx}$ is the acceptance factor for central fiducial photons associated with cx $Z\gamma$ events that have already satisfied the Z selection and $E_T^{\gamma} > 5.0$ GeV and $\Delta R_{e\gamma} > 0.7$ requirements.

The central fiducial photon selection efficiency is given by

$$\begin{aligned} \epsilon^{\gamma}_{cem} &= \epsilon^{\gamma}_{ET4} \cdot \epsilon^{\gamma}_{\Sigma PT4} \cdot \epsilon^{\gamma}_{N3D} \cdot \\ &\quad \epsilon^{\gamma}_{Had/EM} \cdot \epsilon^{\gamma}_{Lshr} \cdot \epsilon^{\gamma}_{\chi^2_{strip}+\chi^2_{wire}} \cdot \epsilon^{\gamma}_{no\ 2^{nd}\ CES} \cdot \mathcal{P}^{\gamma}_{\overline{conv}} \cdot \mathcal{S}^{cem}_{e\to\gamma} \end{aligned} \tag{B.8}$$

where the individual terms are the central fiducial photon efficiencies as listed in section 4.2.5. The factor $\mathcal{P}^{\gamma}_{\overline{conv}}$ is the probability that a photon will traverse the material of the inner central detector without converting to an e^+e^- pair. This

factor is determined from CEM energy scale studies for CDF W/Z boson mass measurements[33, 60], by the amount of material on average that is considered in the inner central detector, $< \Delta T >= 4.6 \pm 0.3\%$ of a radiation length, χ_o^e. This corresponds to a conversion length, χ_o^γ, of $3.6 \pm 0.3\%$. The Baur/ISAJET/QFL $Z\gamma$ MC is used as a cross-check by obtaining the fraction of events where the photon would have passed all cuts if it had not converted to an e^+e^- pair. The calculation of $\mathcal{P}_{\overline{conv}}^\gamma$ and the MC result are in good agreement. The systematic uncertainty is defined by the difference between the two methods. Explicitly searching for isolated $\gamma \rightarrow e^+e^-$ conversion pairs, where $|\eta_{\gamma \rightarrow e^+e^-}| < 1.1$, provided another cross-check for $\mathcal{P}_{\overline{conv}}^\gamma$. No $Z + (\gamma \rightarrow e^+e^-)$ candidate events were found.

Since electron test beam data was used to determine some of the individual photon efficiencies, as discussed in section 5.2.2, differences in EM shower development for electrons and photons are corrected by the factor $\mathcal{S}_{e \rightarrow \gamma}^{cem}$. This factor was obtained using QFL γ vs. e MC simulations, and is described as the ratio of QFL γ vs. e efficiency products as listed in Table 5.5.

References

[1] J.D. Bjorken and S.D. Drell, *Relativistic Quantum Mechanics*, McGraw-Hill, New York, 1964.

[2] S.L Glashow, Nucl. Phys. **B22**, 579 (1961) S. Weinberg, Phys. Rev. Lett. **19**, 1264 (1967) A. Salam, in *Elementary Particle Theory*, edited by N. Svartholm (Almquist and Wiskell, Stockholm, 1968), p.367

[3] F.A. Berends, R. Kleiss, Z. Phys. **C27**, 155 (1985)

[4] F. Abe *et al.*, *A Measurement of* $\sigma \cdot \mathrm{B}(W \rightarrow e\nu)$ and $\sigma \cdot \mathrm{B}(Z \rightarrow e^+e^-)$ *in* $\bar{p}p$ *Collisions at* $\sqrt{s} = 1800$ GeV, submitted to Phys. Rev. D. (1990)

[5] H. Baer, V. Barger and K. Hagiwara, Phys. Rev. **D30**, 1513 (1984).

[6] Z. Ryzak, Nucl. Phys. **B289**, 301 (1987)

[7] U. Baur, E.L. Berger, Phys Rev **D41**, 1476 (1990).

[8] K. Hagiwara *et al*, Nucl. Phys. **B282**, 253 (1987)

[9] C.N. Yang, Phys. Rev. **77**, 242 (1950).

[10] J.M. Cornwall, D.N. Levin and G. Tiktopoulos, Phys. Rev. Lett. **30**, 1268 (1973); Phys. Rev. **D10**, 1145 (1974); C.H. Llewellyn Smith, Phys. Lett. **46B**, 233 (1973); S.D. Joglekar, Ann. of Phys. **83**, 427 (1974).

[11] A. Barroso *et al*, Z. Phys. **C28**, 149 (1985).

[12] S. Errede, private communication.

[13] F. Boudjema, private communication.

[14] F. M. Renard, Nucl. Phys. **B196**, 93 (1982).

[15] S. van de Meer, Proceedings of the SLAC and Fermilab Summer Schools on the Physics of Particle Accelerators, edited by M. Dienes and M. Month, AIP Conference Proceedings **153**, American Institute of Physics, New York, 1987; Design Report Tevatron I Project, Fermi National Accelerator Laboratory, Sept. 1984.

[16] F. Abe et al.,(CDF Collaboration). The CDF Detector: An Overview. *Nuclear Instruments and Methods in Physics Research*, **A271**, 387-403(1988).

[17] F. Snider et al., CDF Vertex Time Projection Chamber System. *Nuclear Instruments and Methods in Physics Research*, **A268**, 75-91(1988).

[18] F. Bedeschi et al.,*Nuclear Instruments and Methods in Physics Research*, **A268**, 50 (1988).

[19] L. Balka et al.,*Nuclear Instruments and Methods in Physics Research*, **A267**, 272 (1988).

[20] S. Bertolucci et al.,*Nuclear Instruments and Methods in Physics Research*, **A267**, 301 (1988).

[21] S.R. Hahn et al., Calibration Systems for the CDF Central Electromagnetic Calorimeter. *Nuclear Instruments and Methods in Physics Research*, **A267**, 351-366(1988).

[22] K. Yasuoka et al., Response Maps of the CDF Central Electromagnetic Calorimeter with Electrons. *Nuclear Instruments and Methods in Physics Research*, **A267**, 315-329(1988).

[23] Y. Fukui et al., CDF End Plug Electromagnetic Calorimeter Using Conductive Plastic Proportional Tubes. *Nuclear Instruments and Methods in Physics Research*, **A267**, 280-300(1988).

[24] M.E.B. Franklin et al.,in the proceedings of the 7^{th} *Topical Workshop on Proton-Antiproton Collider Physics*, p. 420, edited by R. Raja, A. Tollestrup and J. Yoh, World Scientific, Singapore (1988).

[25] G. Brandenberg, et al.,*Nuclear Instruments and Methods in Physics Research*, **A267**, 257 (1988).

[26] S. Cihangir et al.,*Nuclear Instruments and Methods in Physics Research*, **A267**, 249 (1988).

[27] D. Amidei et al., A Two Level FASTBUS Based Trigger System for CDF. *Nuclear Instruments and Methods in Physics Research*, **A269**, 51-62(1988).

[28] G.W. Foster et al., A Fast Hardware Track-Finder for the CDF Central Tracking Chamber. *Nuclear Instruments and Methods in Physics Research*, **A269**, 93-100(1988).

[29] T. Carroll et al.,*Nuclear Instruments and Methods in Physics Research*, **A263**, 199 (1988);T. Carroll et al., *Nuclear Instruments and Methods in Physics Research*, **A300**, 552 (1991).

[30] P. Hurst, Ph.D. thesis, Harvard University (1991).

[31] C. Newman-Holmes, E.E. Schmidt, R. Yamada, *Nuclear Instruments and Methods in Physics Research*, **A274**, 443 (1989).

[32] The Particle Data Group. Review of Particle Properties. Phys. Lett. **B204**, April 1988.

[33] F. Abe et al., Phys. Rev. **D43**, 2070 (1991); F. Abe et al., Phys. Rev. Lett. **65**, 2243 (1990); W. Trischuk, Ph.D. thesis, Harvard University (1990); P. Schlabach, Ph.D. thesis, University of Illinois at Urbana-Champaign (1990).

[34] M. Binkley, S. Errede and A.B. Wicklund, "A New Determination of the CEM Energy Scale", **CDF-1226** (1990).

[35] C. Campagnari et al., "A Standard Data Sample for $W \rightarrow e\nu$ and $Z \rightarrow ee$ Analysis", **CDF-1166** (1990).

[36] B. Winer, Ph.D. thesis, University of California at Berkeley (1991)

[37] F. Abe et al., Phys. Rev. Lett. **64**, 152 (1990); F. Abe et al., Phys. Rev. Lett. **68**, 3398 (1992); A. Roodman, Ph.D. thesis, University of Chicago (1991).

[38] F. Abe et al., Phys. Rev. Lett. **62**, 1005 (1989); F. Abe et al., Phys. Rev. **D44**, 29 (1991); F. Abe et al., Phys. Rev. Lett. **69**, 28 (1992); P. Derwent, Ph.D thesis, University of Chicago (1990); R.L. Swartz, Jr., Ph.D. thesis, University of Illinois at Urbana-Champaign (1993).

[39] D. Benjamin, private communication.

[40] C. Campagnari, "A Fast W and Z Monte Carlo", **CDF-1025** (1989).

[41] S. Errede, "Measurement of $\sigma * BR(W+\gamma)$ and $\sigma * BR(Z+\gamma)$ in the Electron and Muon Channels in $\sqrt{s} = 1.8$ TeV $p\bar{p}$ Collisions", **CDF-1941** (1993).

[42] VEGAS, G. Peter Lepage, J. Comp. Phys. **27**, 192-202, Academic Press (1978); G. Peter Lepage, CLNS-80/447 (1980).

[43] ISAJET Monte Carlo version 6.24, F.E. Paige and S.D. Protopopescu, BNL Technical Report No. 38034, 1986(unpublished).

[44] PAPAGENO Monte Carlo version 3.12, I. Hinchliffe, (to be published).

[45] PYTHIA version 5.4, T. Sjöstrand, Computer Phys. Commun. **39**, 347 (1986); T. Sjöstrand and M. Bengstson, Computer Phys. Commun. **43**, 367 (1987); Hans-Uno Bengtsson and T. Sjöstrandk, Computer Phys. Commun. **46**, 43 (1987).

[46] R.G. Wagner, Computer Phys. Commun. **70**, 15 (1992)

[47] PDFLIB version 3.11, H. Plothow-Besch, Computer Phys. Commun. **75**, 396 (1993); H. Plothow-Besch, CERN Report W5051, (1992).

[48] F. Abe et al., Phys. Rev. Lett. **66**, 2951 (1991); F. Abe et al., Phys. Rev. Lett. **67**, 2937 (1991); B. Winer, Ph.D. thesis, University of California at Berkeley (1991); J. Ng, Ph.D. thesis, Harvard University (1991); J. Ng, **CDF-1504**.

[49] M. Mangano, "The Unweighting of Matrix Element Monte Carlos", **CDF-1665** (1992).

[50] S. Errede, "Methodology for the Measurement of $W\gamma$ and $Z\gamma$ in the Muon Channel at CDF", **CDF-1732** (1992).

[51] L. Keeble, "New Jet Correction Function QDJSCO version 2.0", **CDF-1513** (1991).

[52] VECBOS Monte Carlo, F.A. Berends, W.T. Giele, H. Kuijf and B. Tausk, Nucl. Phys. **B357**, 32 (1991).

[53] HERWIG Monte Carlo version 5.6, G. Marchesini and B.R. Webber, Nucl. Phys. **B310**, 461 (1988).

[54] Barry Wicklund, private communication.

[55] Review of Particle Properties, Phys. Rev. **D45**, III.39, (1992).

[56] J.Ng **CDF-1504** (1991) and S. Eno et al., "Update on the Measurement of the W/Z Cross Sections in the Muon Channel" **CDF-1629** (1991).

[57] MINUIT, F. James and M. Roos, CERN Report D506, 1988.

[58] U. Baur, Phys. Rev. **D47**, 4889, (1993).

[59] O. Adriani, et al, Phys. Lett. **B 297**, 469 (1992); and J. Busenitz, private communication.

[60] F. Abe et al., Phys. Rev. Lett. **63**, 720 (1989); H. Keutelian, Ph.D. thesis, University of Illinois at Urbana-Champaign (1990).